# Study of the interaction of static converters on a shared DC bus

Zakaria Chmeit

Zakaria Chmeit. Study of the interaction of static converters on a shared DC bus. Electric power. Université de Technologie de Compiègne; Université Libanaise, 2021. English. NNT : 2021COMP2652 . tel-04005072

HAL Id: tel-04005072
https://theses.hal.science/tel-04005072

Submitted on 26 Feb 2023

Par **Zakaria CHMEIT**

# *Étude de l'interaction de convertisseurs statiques sur un bus DC mutualisé*

Thèse présentée en cotutelle
pour l'obtention du grade
de Docteur de l'UTC

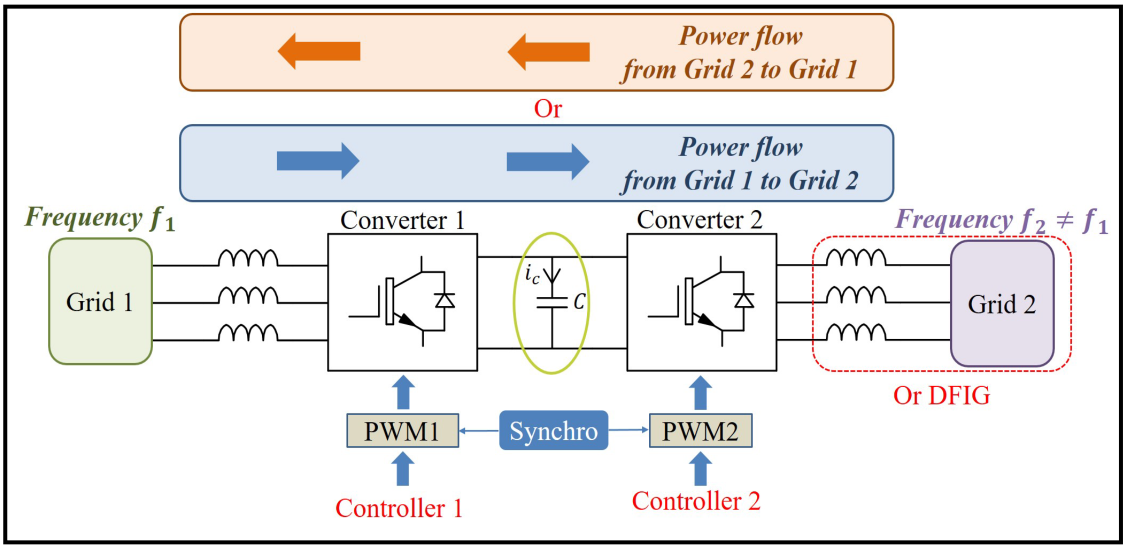

Soutenue le 14 décembre 2021
**Spécialité :** Génie Électrique : Unité de recherche en Mécanique - Laboratoire Roberval (FRE UTC - CNRS 2012)
D2652

Université Libanaise
Ecole Doctorale
Sciences et Technologie

## Thèse de doctorat en Cotutelle

Pour obtenir le grade de Docteur délivré par

# L'Université de Technologie de Compiègne
# et
# L'Université Libanaise

## Spécialité : Génie Électrique

Présentée et soutenue publiquement par

## CHMEIT Zakaria

# Étude de l'interaction de convertisseurs statiques sur un bus DC mutualisé

**14 Décembre 2021**

## Membres du Jury :

| | |
|---|---|
| **M. Farid MEIBODY-TABAR,** Prof. ENSEM - Université de Lorraine | Rapporteur |
| **M. Mohamed Wissem NAOUAR,** MCF, Ecole Nationale d'Ingénieurs de Tunis | Rapporteur |
| **M. Guy FRIEDRICH,** Prof. Roberval – Université de Technologie de Compiègne | Examinateur |
| **M. Lahoucine ID-KHAJINE,** MCF, Université de Cergy-Pontoise | Examinateur |
| **M. Jawad KHOURY,** MCF, Lebanese American University | Examinateur |
| **Mme. Rita MBAYED,** Prof. Université Libanaise | Examinatrice |
| **M. Nicolas PATIN,** HDR, Roberval – Université de Technologie de Compiègne | Directeur |
| **M. Georges SALLOUM,** Prof. Université Libanaise | Directeur |

# Acknowledgments

Firstly, I would like to take a moment to acknowledge, with my sincere gratitude, to my supervisors Mr. Nicolas PATIN (HDR at Université de Technologie de Compiègne) and Mr. Georges SALLOUM (Professor at Lebanese University) and my co-supervisor Mrs. Rita MBAYED (professor at Lebanese University) for their advices, motivations, and patience throughout the development of this thesis. Their guidance steered me toward completing my research and writing it.

I am grateful to all my friends and my colleagues in Roberval laboratory who have made my stay in Compiègne a pleasant one.

I would also like to thank everyone who has directly or indirectly helped me for the completion of my thesis.

At last, I would like to thank my parents, my brothers, my sisters and my friends who have always been great source of inspiration, for their constant support, and for providing me the continuous encouragement and persistent motivation throughout my years of study.

Thank you all.

# Table of contents

# List of figures

# List of tables

# List of abbreviations

| | |
|---|---|
| DFIM | Doubly Fed Induction Machine |
| IM | Induction Machines |
| WT | Wind Turbine |
| DFIG | Doubly Fed Induction Generator |
| SCIM | Squirrel Cage Induction Machine |
| MMF | Magneto-Motive Force |
| EMF | Electro-Motive Force |
| RSC | Rotor Side Control |
| SRF | Synchronous Reference Frame |
| PLL | Phase-locked loop |
| VOC | Voltage Controlled Oscillator |
| SFO | Stator-Flux Orientation |
| FOC | Field Oriented Control |
| PI | Proportional-Integral |
| DC | Direct Current |
| AC | Alternative Current |
| IGBT | Insulated Gate Bipolar Transistor |
| MOSFET | Metal-Oxide Semiconductor Field-Effect Transistor |
| TRIAC | Triode for Alternating Current |
| SCR | Silicon Controlled Rectifiers |
| VSC | Voltage Source Converters |
| ASD | Adjustable Speed Drives |
| UPS | Uninterruptible Power Supplies |
| PV | Photovoltaic |
| VSI | Voltage Source Inverter |
| CCM | Continuous Conduction Mode |
| JFET | Junction Field-Effect Transistor |

| | |
|---|---|
| PWM | Pulse Width Modulation |
| DFIM | Doubly Fed Induction Machine |
| THD | Total Harmonic Distortion |
| CPWM | Continuous PWM |
| SPWM | Sinusoidal PWM |
| SVPWM | Space Vector PWM |
| THIPWM | Third Harmonic Injection PWM |
| DCPWM | Double Carrier PWM |
| APWM | Adjacent PWM |
| DPWM | Discontinuous PWM |
| GDPWM | Generalized Discontinuous PWM |
| RPWM | Random PWM |
| RCD-PWM | Random Centered Distribution PWM |
| RZD-PWM | Random Zero-Vector Distribution PWM |
| Ext-DCPWM | Extended Double Carrier PWM |
| Uni-DCPWM | Unified Double Carrier PWM |
| WECS | Wind Energy Conversion Systems |

# List of symbols and notations

| | |
|---|---|
| $P_s, P_r$ | Stator and rotor real power respectively. |
| $Q_s, Q_r$ | Stator and rotor reactive power respectively. |
| $i_s = (i_{sa}, i_{sb}, i_{sc})$<br>$i_r = (i_{ra}, i_{rb}, i_{rc})$ | Three-phase instantaneous stator and rotor currents. |
| $F_s, F_r$ | Stator and rotor magneto-motive forces. |
| $f_s, f_r$ | Stator and rotor frequencies. |
| $\omega_s, \omega_r$ | Stator and rotor angular frequencies. |
| $p$ | Number of pair of poles. |
| $\Omega_s, \Omega_r$ | Rotating speeds for $F_s$ and $F_r$ forces respectively ($\Omega_s$ is called synchronous speed too). |
| $\Omega$ | Mechanical speed of the machine. |
| $N_s, N_r$ | Number of the wire turns in the stator and rotor coils per phase. |
| $T_{em}$ | Electromagnetic torque. |
| $s$ | Slip of the machine. |
| $P_m$ | Mechanical power. |
| $\theta$ | Mechanical position of the rotor with respect to the stator. |
| $\theta_e = p\theta$ | Electrical position of the rotor with respect to the stator. |
| $\omega$ | Electrical rotor speed regarding to the stator stationary frame. |
| $x_i^j$ | The superscript ($j = s, r$) denotes if the parameter $x$ is stator or rotor related variable. While the subscript ($i = s, r$) denotes the $\alpha\beta$-frame where the parameter $x$ is viewed. |
| $x_s = x_{sd} + jx_{sq}$ | Complex notation of the stator variable $x_s$. |
| $x_r = x_{rd} + jx_{rq}$ | Complex notation of the rotor variable $x_r$. |
| $v_s^s, v_r^r$ | Complex notation for stator (respectively rotor) voltage of the machine referred to the stator (respectively rotor) $\alpha\beta$-frame. |
| $i_s^s, i_r^r$ | Complex notation for stator (respectively rotor) current of the machine referred to the stator (respectively rotor) $\alpha\beta$-frame. |
| $\varphi_s^s, \varphi_r^r$ | Complex notation for stator (respectively rotor) flux of the machine referred to the stator (respectively rotor) $\alpha\beta$-frame. |

| | |
|---|---|
| $R_s, R_r$ | Stator and rotor windings resistance of the machine per phase. |
| $v_s, v_r$ | Stator and rotor voltage in $dq - frame$. |
| $i_s, i_r$ | Stator and rotor currents in $dq - frame$. |
| $\varphi_s, \varphi_r$ | Stator and rotor linkage flux in $dq - frame$. |
| $\varphi_{ls}, \varphi_{lr}$ | Stator and rotor leakage flux in $dq - frame$. |
| $\varphi_m$ | Mutual linkage flux in $dq - frame$. |
| $M$ | Cyclic mutual inductance in $dq - frame$. |
| $L_{ls}, L_{lr}$ | Stator and rotor leakage inductance per phase in $dq - frame$. |
| $L_{cs}, L_{cr}$ | Stator and rotor cyclic self-inductance per phase in $dq - frame$. |
| $L_s, L_r$ | Stator and rotor self-inductance per phase. |
| $m_s, m_r$ | Mutual inductance between two stator (rotor) phases. |
| $m_{sr}$ | Mutual inductance between stator and rotor phases. |
| $\sigma$ | Dispersion coefficient of the machine. |
| $J$ | Inertia moment. |
| $f$ | Viscous friction coefficient of the machine. |
| $T_L$ | Load torque applied on the machine. |
| $T_{max}$ | Maximal torque of the machine. |
| $s_{max}$ | Slip ratio corresponding to $T_{max}$. |
| $V_s$ | Peak value of the stator voltage. |
| $\Phi_s$ | Peak value of the stator flux. |
| $x^*$ | Desired value of variable $x$. |
| $K_p^i, K_i^i$ | Gain parameters for the current controller. |
| $K_p^\Omega, K_i^\Omega$ | Gain parameters for the speed controller. |
| $K_p^p, K_i^p$ | Gain parameters for the power controller. |
| $\tau_i$ | Constant time of the current controller. |
| $\tau_\Omega$ | Constant time of the speed controller. |
| $\tau_p$ | Constant time of the power controller. |
| $t_d$ | Dead Time |
| $v_a , v_b , v_c$ | Three-phase voltage |
| $i_a , i_b , i_c$ | Three-phase current |
| $L$ | Load Inductor |

| | |
|---|---|
| $R$ | Load Resistor |
| $v_{dc}$ | DC-link voltage |
| $C_3 = (c_a, c_b, c_c)$ | The switches state |
| $x^T$ | The transpose of matrix or vector $x$ |

# Abstract

The impact of Pulse Width Modulation (PWM) strategies on the stresse of the decoupling capacitors at the input of a three-phase converter is currently well known, as well as the behavior of the supplied load (power factor). A large panel of modulation techniques is currently available and can be applied according to the various environmental constraints (stress on the capacitors but also quality of the currents in the load or switching losses in the semiconductors). However, in many application contexts, the DC bus can be shared between several converters that will individually stress the decoupling capacitor(s).

The objective of this thesis is to study the implementation of PWM strategies between several converters sharing their DC bus. More precisely, a study of the case of back-to-back converters connected on Doubly Fed Induction Machine (DFIM) has been done.

The aim of this study is to evaluate the impact of interleaved PWM strategies on the RMS current flowing through the DC link capacitor associated to two back-to-back three-phase Full Bridges (FB). Indeed, this value is usually the key-parameter for the sizing of this (or these) component(s), far above the capacitance, especially for aluminum electrolytic capacitors. Interleaving technique is applied on two different strategies:

- Classical (single carrier) Space-Vector PWM strategy (SVPWM).
- Unified Double Carrier PWM (Uni-DCPWM) that is dedicated to the reduction of the RMS current for a single FB.

Our study also aims to reduce the RMS current in the capacitor and find the optimal value of the interleaving time dynamically for all operating points.

# Résumé

L’impact des stratégies Modulation de Largeur d'Impulsion MLI sur les sollicitations des condensateurs de découplage en entrée d’un onduleur triphasé est bien connu à l’heure actuelle au même titre que le comportement de la charge alimentée (facteur de puissance). On dispose à l’heure actuelle d’un large panel de techniques de modulation applicables en fonction des diverses contraintes d’environnement (stress des condensateurs mais aussi qualité des courants dans la charge ou pertes par commutation dans les semi-conducteurs). Toutefois, dans de nombreux contextes applicatifs, le bus continu peut être mutualisé entre plusieurs convertisseurs qui vont solliciter individuellement le ou les condensateurs de découplage.

L’objectif de cette thèse est d'étudier la mise en œuvre des stratégies MLI coordonnées entre plusieurs onduleurs mutualisant leur bus continu. Plus précisément, une étude du cas des convertisseurs back-to-back dans le cas de MADA a été faite.

De plus, cette étude vise à évaluer l'impact de stratégies MLI entrelacées sur le courant efficace traversant le condensateur de découplage associé à deux convertisseurs en parallèle. En effet, cette valeur est généralement le paramètre clé pour le dimensionnement de ce (ou ces) composant(s), bien au-delà de la capacité, notamment pour les condensateurs électrolytiques à l'aluminium. La technique d'entrelacement est appliquée selon deux stratégies différentes :

- La stratégie classique SVPWM.
- La stratégie MLI à double porteuse unifié (Uni-DCPWM) qui est dédié à la réduction du courant efficace pour un seul convertisseur.

Notre étude vise également à réduire le courant RMS dans le condensateur et à trouver la valeur optimale du temps d'entrelacement de manière dynamique pour tous les points de fonctionnement.

# Introduction

The wind turbines offered in the market can be divided into two main categories according to the electric generator: those equipped with an asynchronous generator (about 75% of the market), and those equipped with a synchronous generator (about 25% of the market) [1]. Referring to Figure 0.1, by 2050, solar power, with 8 500 GW installed capacity, and wind, with 6 000 GW, would account for three-fifths of global electricity generation [2]. Today, wind power generation systems that has a capacity of 1 MW and more almost exclusively use the Doubly Fed Induction Machine (DFIM) [3].

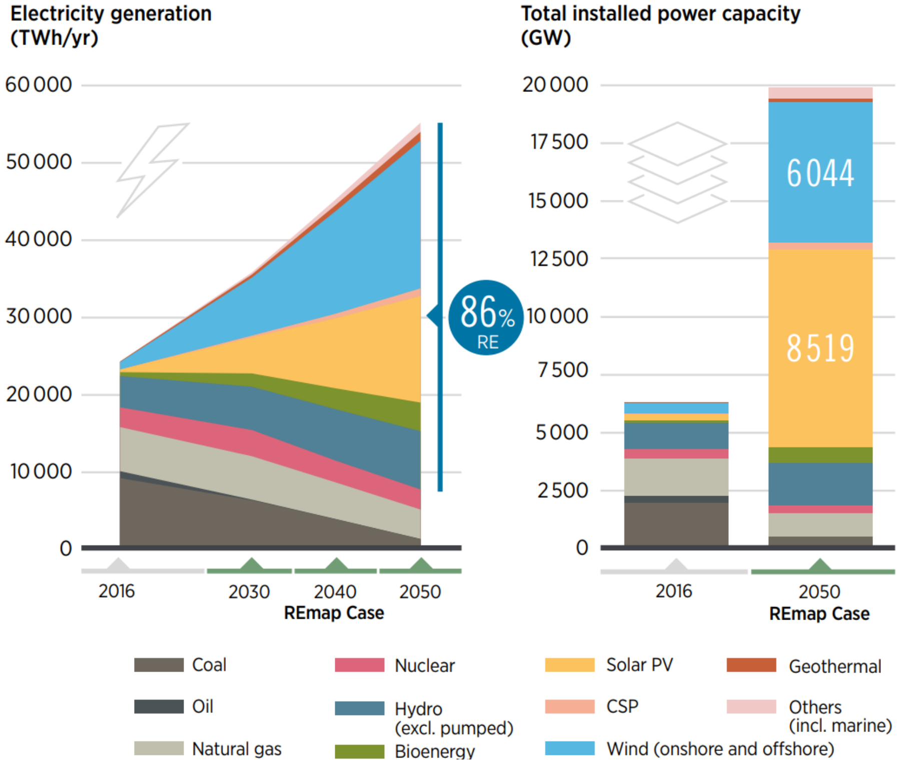

*Figure 0.1: Electricity generation and power installed capacity, REmap Case, 2016-2050 [2].*

This machine is very popular because it has some advantages over all other variable-speed machine types. Its use in the electro-mechanical conversion chain as generator or motor has grown in recent years [4]. Indeed, the static converter that used to rectify-wave the alternating currents of the rotor has a rated power which is fractional of that of the machine, which reduces its cost compared to competing topologies.

The doubly fed induction machine is a wound rotor induction machine. The stator windings are connected directly to the three-phase grid while the rotor windings are connected to power converters that are bi-directional in current. The power passing through these converters can be absorbed or produced by the machine, depending on the operating mode (sub/super-synchronous). The capacitor between two converters represents the shared DC bus. This electromechanical conversion system is depicted in Figure 0.2.

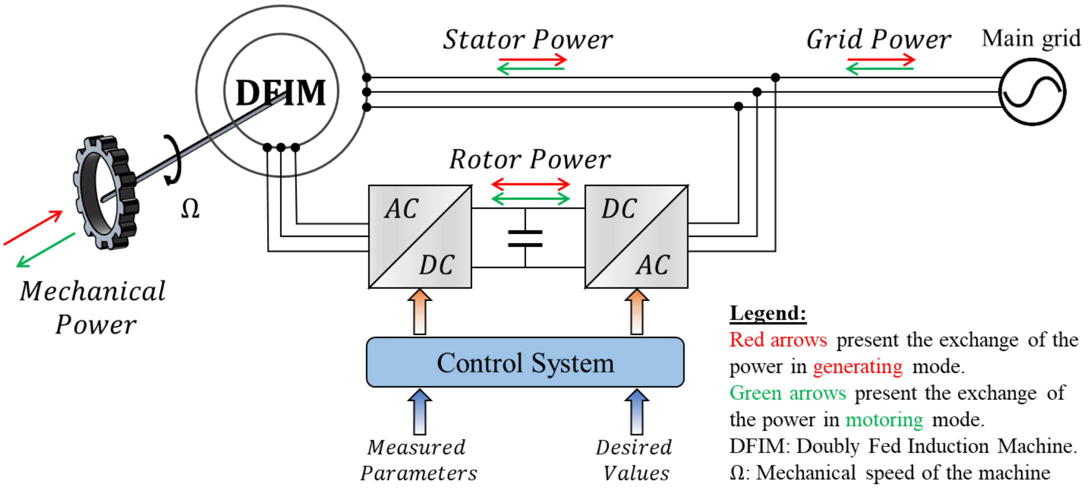

*Figure 0.2: Electro-mechanical conversion system based on a DFIM*

In the back-to-back converters structure driving the doubly fed induction machine rotor, the RMS value of the current passes through the decoupling capacitor of the DC-link is the key parameter for sizing this later [5]. In fact, this current is directly linked to the Pulse Width Modulation (PWM) strategy used to control both converters. In the literature, this problem has been very detailed for a single inverter [6]–[12], but it has been very little addressed in the case of several converters. For example, in [13], a quick study has been carried out on a dual converter architecture for vehicles but in this case, we are confronted with a major difficulty that is the operating points of these two converters are independent. In this context, the development of a joint pulse width modulation strategy for both bridges is very difficult. The problem is simpler to tackle here because in the structure of Figure 0.2, the operating points of the two converters are always related, because the instantaneous power flowing through the converter connected to the grid must be the same as the one injected into the rotor of the doubly fed induction machine in order to stabilize the DC bus voltage. Thus, only the fundamental frequencies of the controls of these two bridges, their amplitudes and the current/voltage phase shifts on each AC side differ.

The objective of this thesis work was to integrate this aspect of the close control of the switches within a global control of the system structure presented above and used in a context of fixed frequency and variable speed generation.

Besides the introduction and conclusion, this thesis report consists of four chapters as depicted in Figure 0.3. First chapter deals with the doubly fed induction machine, starting with its interest through its principle of operation that is detailed by talking about the electromagnetic torque production, sub/super synchronism mode and motor/generator operation. Then an analysis and modelling for the doubly fed induction machine is done. After that, second chapter is devoted to the control of this machine where the doubly fed induction machine model (obtained in chapter 1) is simplified under the Stator Flux Orientation (SFO) concept. And then a test is done in order to analyze the performance of this control.

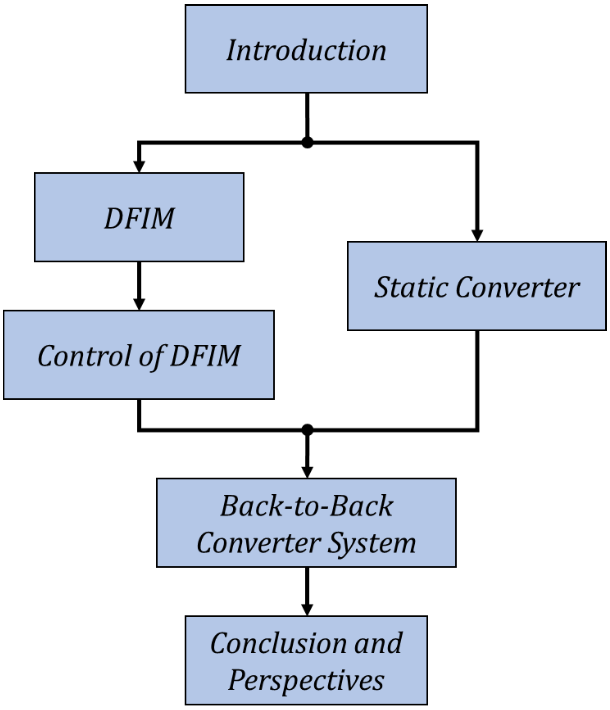

*Figure 0.3: Information flow for this book.*

In chapter 3, the static converter has been studied where the Voltage Source Converter (VSC) is detailed by talking about its structure. And an analysis for the system is done by modelling the load (output of the converter), the DC-bus (input of the converter) and the converter itself. Thereafter, the pulse width modulation strategies are addressed (Space Vector Pulse Width Modulation SVPWM, Double Carrier Pulse Width Modulation DCPWM, Generalized Discontinuous Pulse Width Modulation GDPWM and Unified

Double Carrier Pulse Width Modulation Uni-DCPWM) in order to command the converter. Finally, chapter 4 is dedicated to the back-to-back converter system (global system), where the static converter, DFIM and its control are assembled. In addition, in this chapter the interleaving time factor (between the PWM strategies of the converters) is introduced in order to study its impact on the shared DC-link current in both cases: SVPWM and Uni-DCPWM strategies. Therefore, simulation results are shown for different operation points. At the end of this chapter an algorithm is proposed for tracking the optimal value of the interleaving time for each operating point. Finally, this thesis will end with a general conclusion summarizing the main results obtained as well as some perspectives that is important to be done.

# Chapter 1: Doubly Fed Induction Machine

## 1.1 Interest of DFIM

The direct connection of Induction Machines (IM) to the network obligates the speed to remain almost constant so that the machine remains close to synchronism. This restriction leads to decrease the efficiency for Wind Turbine (WT) applications at high wind speeds. The addition of the power converter between the stator and the grid results in a decoupling between the frequency of the electricity main grid and the rotating speed of the machine that allows operating at variable speed. However, this converter must be sized to handle the entire power generated by the machine.

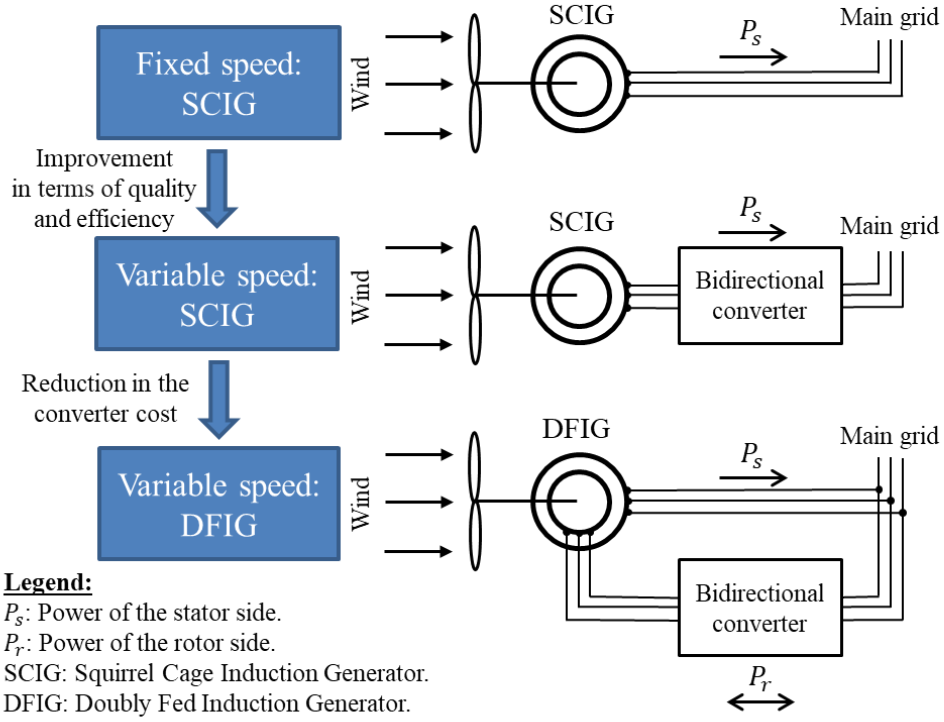

*Figure 1.1:Development of the electrical configuration of the induction machine.*

With the use of IM with double power supply driven by the rotor, most of the power is directly distributed to the grid by the stator and part of this power (generally less than 25%) goes through the converters of power through the rotor (see Figure 1.1). This gives the opportunity to use smaller and therefore less expensive converters [14]. The presence of this converter allows to control the power at the generator output and handle the speed fluctuation. The disadvantage of this system is the presence of brushes at the rotor, which requires more important maintenance work.

For WT application where the Doubly Fed Induction Generator (DFIG) is widely used, the rotor speed is adjusted according to the wind speed. Indeed, the DFIG allows an operation in sub-synchronous and super-synchronous modes. The advantage of variable speed for a WT is that it can operate over a wide range of wind speeds, which allows to extract the maximum possible power for each wind speed [15].

With these configurations, the WT that uses induction machine has undergone a big evolution, that has led today to intensive use of DFIG in 80% of installed WT [14].

This chapter is going to deal with the operation principle of the DFIM by presenting its case of running in sub/super synchronism condition for both operation: modes motor and generator. Then a mathematical model for the machine is done in stationary and rotating frames which allow finding its powers and torque expressions, and also, finding a simplified block diagram for the machine. Finally, a free acceleration test is performed for the obtained mathematical model.

## 1.2 Operation principle of DFIM

### 1.2.1 Production of the electromagnetic torque

When the stator is supplied by a balanced three-phase source, the instantaneous currents $i_s = (i_{sa}, i_{sb}, i_{sc})$ passing in the three-phase winding create a Magneto-Motive Force (MMF) $F_s$ which rotates at a speed $\Omega_s = \frac{\omega_s}{p} = \frac{2\pi f_s}{p}$ ($f_s$ and $p$ are stator frequency and the number of pair of poles in the machine respectively). At the rotor side, there is a three-phase winding cores connected to an alternative source having a frequency $f_r$ and it produces a MMF $F_r$ rotating at speed $\Omega_r = \frac{\omega_r}{p} = \frac{2\pi f_r}{p}$ with respect to the rotor. In order to maintain the average torque constant when the rotor rotates with regard to the stator, it is obligated that both MMF $F_s$ and $F_r$ remain synchronous. This would imply that the rotor itself must rotate at a speed of $\Omega = \Omega_s - \Omega_r$. Any other speed produces a continuous sliding of the rotor poles in relation to the stator poles. The average torque would then be zero and the machine would stop [16].

The resulting MMF $F$ is the sum of $F_r$ and $F_s$ as described in (1.1) in phasor notation. This MMF $F$ creates a magnetizing flux in the air gap $\varphi_m$.

$$\overline{F} = \overline{F_s} + \overline{F_r} \tag{1.1}$$

Equation (1.1) can be reformulated as function of the currents as mentioned in (1.2) thanks to $\overline{F_r} = -N_r.\overline{i_r}$, $\overline{F_s} = N_s.\overline{i_s}$ and $\overline{F} = N_s.\overline{i_m}$ [4] (note that $N_r$ and $N_s$ are the numbers of the wire turns in the rotor and stator coils per phase respectively, while $\overline{i_r}$, $\overline{i_s}$ and $\overline{i_m}$ are rotor, stator and magnetizing currents respectively).

$$N_s.\overline{i_m} = N_s.\overline{i_s} - N_r\overline{i_r} \implies \overline{i_s} = \overline{i_m} + \frac{N_r}{N_s}\overline{i_r} \tag{1.2}$$

The electromagnetic torque between both MMFs, represented by $\overline{F}$ and $\overline{F_r}$, is their cross product as expressed in (1.3) [4].

$$T_{em} = \left\|\overline{F} \times \overline{F_r}\right\| \tag{1.3}$$

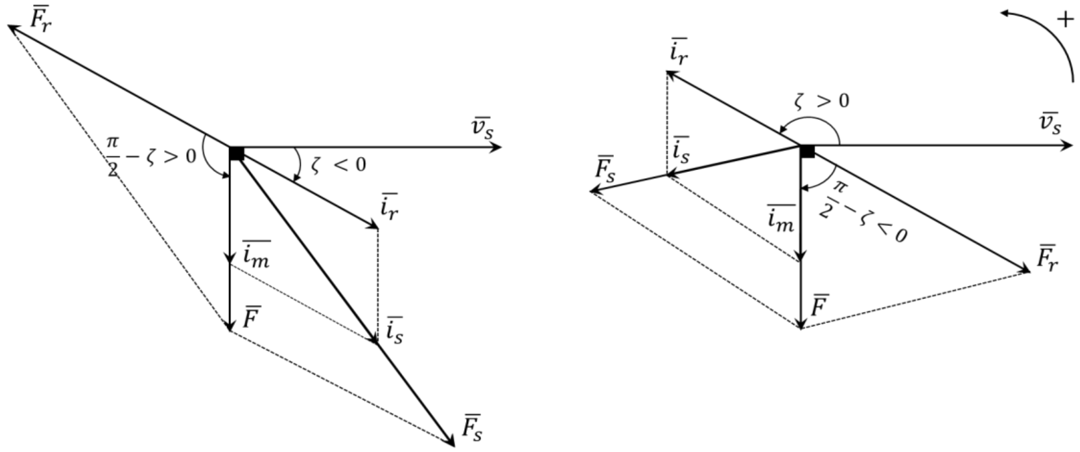

(a) Motor mode (b) Generator mode

*Figure 1.2: Phasor diagram of magneto-motive forces.*

Supposing $\zeta$ is the phase shift of the current $\overline{i_r}$, then the torque can be obtained by (1.4) due to $\overline{F_r} = -N_r.\overline{i_r}$ .

$$T_{em} = F.F_r.\sin(\frac{\pi}{2} - \zeta) \tag{1.4}$$

Figure 1.2 shows the phasor diagram of the MMFs with the phase angle between $\overline{F_r}$ and $\overline{F}$ in motor and generator modes.

### 1.2.2 Operation in sub and super synchronism modes

The slip is defined by the following equations:

$$s = \frac{\Omega_s - \Omega}{\Omega_s} \tag{1.5}$$

$$s = \frac{\omega_s - \omega}{\omega_s} = \frac{\omega_r}{\omega_s} \tag{1.6}$$

$$s = \frac{f_r}{f_s} \tag{1.7}$$

The equation (1.5) yields to:

$$\Omega = (1 - s).\Omega_s \tag{1.8}$$

If the source connected to the rotor creates $F_r$ that rotates in the opposite direction of $F_s$, the slip becomes negative and the rotor will turn faster than the rotating field created by the stator because $\Omega > \Omega_s$. In this case the machine runs in super-synchronous mode.

If the source connected to the rotor creates $F_r$ which rotates in the same direction of $F_s$, the slip is positive and the rotor will rotate slower than the rotating field created by the stator because $\Omega < \Omega_s$. Therefore the machine runs in sub-synchronous mode [16].

In the conventional IM which is Squirrel Cage Induction Machine (SCIM), the machine operates in generator (motor) mode when the slip factor is negative (positive). This is not the case with DFIM where the slip sign indicates if the machine operates in sub or super synchronous modes and it does not mean if the machine runs as motor or generator. Moreover, with DFIM, it is even possible to operate at synchronous speed ($\Omega = \Omega_s$).

### 1.2.3 Generator and motor operations

For generator operation, the DFIM requires a torque on the shaft of the machine in the same direction of the rotating field $F_s$. The effect of this torque causes a forward shift of the rotor poles with respect to the stator poles and therefore the MMF of the rotor $F_r$ is leading both MMFs $F_s$ and $F$ (Figure 1.3). The electromagnetic torque of the machine that is applied to the rotor becomes a resistant torque in the opposite direction of the machine rotation [17].

For motor operation, the resulting MMF $F$ is leading the MMF $F_r$. The torque on the machine shaft is a resistant torque in the opposite direction of the rotational speed of the rotating field $F_s$ and the electromagnetic torque of the machine is a motor torque in the same direction as the rotation.

Each operating mode requires an appropriate control for the rotor voltages, which allows to manage the magnetic field inside the machine and offers the possibility to work in super or sub synchronism speed as well as in motor or generator modes. Noting that, it is no longer the speed of rotation that imposes the motoring and generating operations.

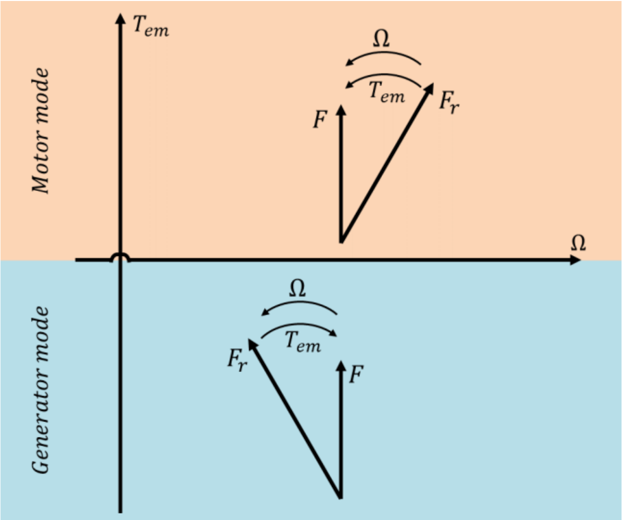

*Figure 1.3: Vector diagram of magneto-motive forces in motoring and generating modes.*

## 1.3 Power transfer in DFIM

The presence of the converter between the rotor and the main grid (like third configuration in Figure 1.1) allows the power to be controlled between the stator and the grid. Figure 1.4 shows the different configurations of the DFIM operation where the stator is connected directly to the grid and the rotor is connected to the grid via the converter. $P_s$ is the real power passing through the stator, $P_r$ is the real power passing through the rotor, and $P_m$, the mechanical power. For power transfer, we distinguish four possible cases [4], [18]:

A. When the machine is running as a motor, the power is supplied by the grid to the stator. If the rotational speed is lower than the synchronism speed, the rotor power $P_r$ (or slip power) is recovered to the network ($P_r = s.P_s$). In this case the machine operates in sub-synchronous as motor. The classical IM can have this operation; however, the slip power is then dissipated as copper losses (heating) in the rotor. The mathematical conditions that reflect this operation while neglecting all losses are:

$$s > 0, \qquad P_s > 0, \qquad P_m > 0, \qquad P_r > 0$$

B. In super-synchronous motor mode, part of the power absorbed by the network goes to the rotor and is converted into mechanical power. The power is therefore supplied to the machine by the stator and the rotor too. The conventional induction machine cannot have this operation. The mathematical conditions are as follows:

$$s < 0, \qquad P_s > 0, \qquad P_m > 0, \qquad P_r < 0$$

C. In sub-synchronous generator mode, the power supplied to the machine by the device that drives it (like WT), it is called a mechanical power. The latter is transferred to the grid by the stator. The slip power is also supplied by the rotor. We therefore have a generator operation below the synchronization speed (sub-synchronous). The conventional induction machine cannot have this mode of operation. The mathematical conditions are as follows:

$$s > 0, \qquad P_s < 0, \qquad P_m < 0, \qquad P_r < 0$$

D. Last case is when the mechanical power delivered to the machine is transferred to the grid via the stator and the slip power is recovered via the rotor to be fed back into the grid. We therefore have a generator operates above the synchronization speed (super-synchronous). Also this mode is available and possible in the conventional SCIM but in this case the slip power is dissipated as Joule’s losses in the rotor. The mathematical conditions are as follows:

$$s < 0\,, \qquad P_s < 0, \qquad P_m < 0\,, \qquad P_r > 0$$

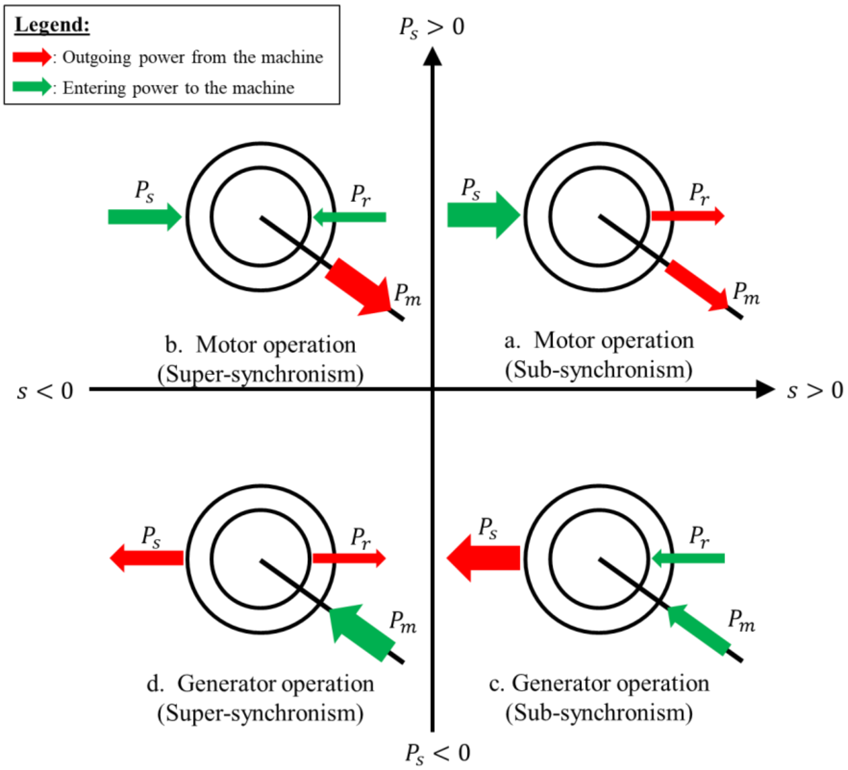

*Figure 1.4: Characteristics of various operation modes of the DFIM.*

We can therefore deduce that the DFIM has two main advantages over the conventional induction machine. The first is the production of electrical power regardless of the rotational speed (sub or super synchronism), while the second is the recovery of slip power.

## 1.4 Modelling of the DFIM

In order to establish the modelling of the DFIM, we will determine the model of an IM with wound rotor. This model will be established in the same way as the SCIM model with the difference of the existence of non-zero rotor voltages $v_{ri} \neq 0$ ($i = a, b, c$) [19]–[29].

### 1.4.1 Assumptions and conventions

In order to analyse and model the DFIM, we have taken into account the following simplifying assumptions and conventions [30], [31]:

- The machine is composed of a cylindrical stator and coaxial rotor. Both carry three-phase and symmetrical windings.
- The air-gap thickness is uniform giving a constant air-gap field at steady state.
- Unsaturated magnetic circuit with constant permeability.
- A sinusoidal spatial distribution of the air-gap field.

These hypotheses allow us the following assumptions [30]:

- Magnetic fluxes are additive.
- The selves inductances are constant.
- The variation of the mutual inductances between the stator and rotor windings is a sinusoidal function of the electrical angle $\theta_e = p.\theta$ along the considered axes ($\theta$ is the mechanical position of the rotor with respect to the stator).

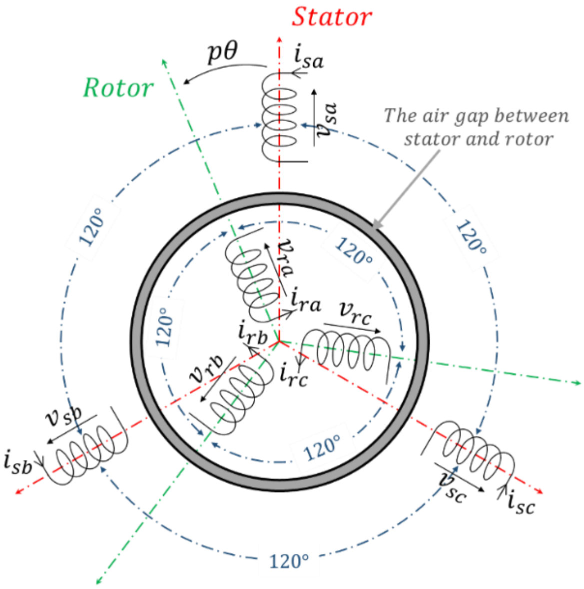

*Figure 1.5: Symbolic representation of the DFIM.*

Figure 1.5 illustrates the symbolic representation of the DFIM, it presents the uniform air gap between the stator and the rotor, stator and rotor three-phase balanced and windings and their voltages, also the the electrical position $p.\theta$ between them.

### 1.4.2 Angular velocities

Prior the modelling, the angular velocities are to be defined:

$$\omega_s = \frac{d\theta_s}{dt} \tag{1.9}$$

$$\omega_r = \frac{d\theta_r}{dt} \tag{1.10}$$

$\omega_s$: The angular speed of the rotating stator flux density regarding the stator stationary frame, it is imposed by the frequency of the grid $f_s$ ( $\omega_s = 2\pi f_s$ ) which is equal to 50Hz in studied case.

$\omega_r$: The angular speed of the rotating rotor flux density regarding the rotor reference frame, it depends on the machine speed and the stator angular frequency as mentioned in (1.13).

The angular electrical position of the rotor along with its electrical rotation speed are given by the following equations:

$$\theta_e = p.\theta \tag{1.11}$$

$$\omega = \frac{d\theta_e}{dt} = p.\frac{d\theta}{dt} = p.\Omega \tag{1.12}$$

$\theta_e$: the electrical position of the rotor.
$\theta$: the mechanical position of the rotor.
$\omega$: the electrical rotor speed regarding to the stator stationary frame.
$p$: Number of pair of pole in the IM.
$\Omega$: the mechanical rotor speed.

Based on Figure 1.6, we conclude the equation (1.13) that describes the frequencies' relation.

$$\omega_s = \omega_r + p.\Omega \tag{1.13}$$

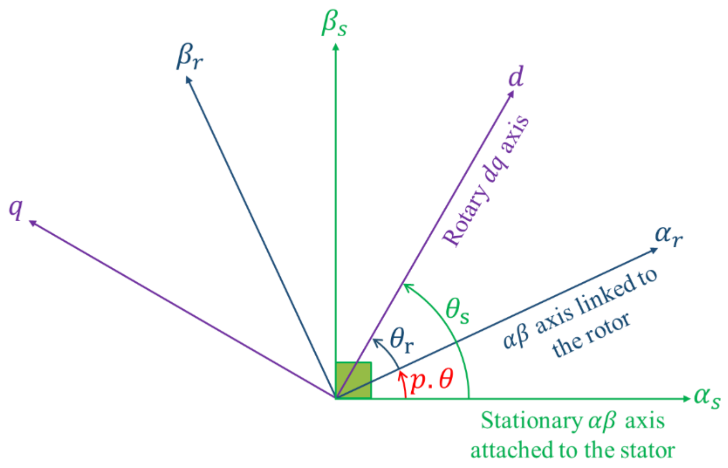

*Figure 1.6: Axes orientation of DFIM.*

### 1.4.3 Modelling of DFIM in stationary frame

At the beginning we introduce the following notation for a complex vector $x$:

$$x_s^s = x_{s\alpha} + jx_{s\beta}$$

$$x_r^r = x_{r\beta} + jx_{r\beta}$$

$$x_s = x_{sd} + jx_{sq}$$

$$x_r = x_{rd} + jx_{rq}$$

The subscript $s$ (respectively $r$) denotes stator-related variables (respectively rotor-related variables), while the superscript $s$ (respectively $r$) denotes that the parameter is observed in the stator (respectively rotor) reference frame. So $x_s^s$ (respectively $x_r^r$) represents the stator (respectively rotor) $x$-variable in stator (respectively rotor) coordinate i.e. each variable is linked to his stationary ($\alpha\beta - axis$) reference. While $x_s$ and $x_r$ represent the stator and rotor $x$-variable linked to the synchronous ($dq - axis$) reference frame.

We start from the general equations of the induction machine which are written, in space vector notation as follows:

$$v_s^s = R_s . i_s^s + \frac{d\varphi_s^s}{dt} \tag{1.14}$$

$$v_r^r = R_r . i_r^r + \frac{d\varphi_r^r}{dt} \tag{1.15}$$

(1.14) and (1.15) show the relation between the voltages, currents and fluxes for the stator and rotor windings referring to stator and rotor reference frame.

$v_s^s, v_r^r$: the complex notation for stator (respectively rotor) voltages of the machine referred to the stator (respectively rotor) frame.

$i_s^s, i_r^r$: the complex notation for stator (respectively rotor) currents of the machine observed in the stator (respectively rotor) frame.

$\varphi_s^s, \varphi_r^r$: the stator and rotor fluxes linkage of the machine linked to the stator and rotor frames respectively in complex notation.

$R_s$ and $R_r$ are the resistances of the stator and rotor windings of the machine per phase.

Equations (1.14) and (1.15) are in different reference frames. To facilitate the modelling, we ought to find all stator and rotor variables in same reference frame. Therefore, the stationary stator reference frame is chosen in this modelling. Hence the variables $v_r^s$, $i_r^s$ and $\varphi_r^s$ viewed from the stationary stator reference frame are described in (1.16), (1.17) and (1.18) respectively thanks to the rotating electrical speed $\omega$ of the rotor regarding to the stator.

$$v_r^s = v_r^r . e^{j\omega t} \tag{1.16}$$

$$i_r^s = i_r^r . e^{j\omega t} \tag{1.17}$$

$$\varphi_r^s = \varphi_r^r . e^{j\omega t} \tag{1.18}$$

By using the equations (1.16), (1.17) and (1.18) in (1.15) we can get the rotor voltage as seen in the stator frame in (1.19).

$$v_r^r = R_r . i_r^r + \frac{d\varphi_r^r}{dt}$$

$$v_r^s . e^{-j\omega t} = R_r . i_r^s . e^{-j\omega t} + \frac{d(\varphi_r^s . e^{-j\omega t})}{dt}$$

$$v_r^s . e^{-j\omega t} = R_r . i_r^s . e^{-j\omega t} + \frac{d\varphi_r^s}{dt} . e^{-j\omega t} - j\omega . \varphi_r^s . e^{-j\omega t}$$

$$v_r^s = R_r . i_r^s + \frac{d\varphi_r^s}{dt} - j\omega . \varphi_r^s \tag{1.19}$$

Suppose that the rotor current, the rotor flux linkage and the EMF in the rotor circuits are already referred to the stator side by scaling with the appropriate turns ratio between the stator and the rotor windings, we obtain the following equations in the stator referential [20]:

$$\varphi_s^s = \varphi_m^s + \varphi_{ls}^s \tag{1.20}$$

$$\varphi_r^s = \varphi_m^s + \varphi_{lr}^s \tag{1.21}$$

$$\varphi_m^s = M\ (\ i_s^s + i_r^s\ ) \tag{1.22}$$

$$\varphi_{ls}^s = L_{ls} i_s^s \tag{1.23}$$

$$\varphi_{lr}^s = L_{lr} i_r^s \tag{1.24}$$

$\varphi_s$and $\varphi_r$ are the stator and rotor flux linkage, while $\varphi_m$ is the mutual flux linkage. As for $\varphi_{ls}$ and $\varphi_{lr}$, they are representing the stator and rotor flux leakage respectively.

$M, L_{ls}, L_{lr}$ represent the cyclic mutual inductance, stator leakage inductance and rotor leakage inductance respectively.

By replacing $\varphi_m$, $\varphi_{ls}$ and $\varphi_{lr}$ by their expressions in (1.20) and (1.21), the stator and rotor linkage fluxes are expressed as function of the currents as mentioned in (1.25) and (1.26).

$$\varphi_s^s = M\ (i_s^s + i_r^s) + L_{ls} i_s^s\ = L_{cs} i_s^s + M i_r^s \tag{1.25}$$

$$\varphi_r^s = M\ (\ i_s^s + i_r^s\ ) + L_{lr} i_r^s = L_{cr} i_r^s + M i_s^s \tag{1.26}$$

Noting that $L_{cs} = L_{ls} + M$ and $L_{cr} = L_{lr} + M$ are the stator and rotor cyclic self-inductances respectively. In the other hand, the relations between the cyclic self-inductances (referred to $dq$ reference) and the real winding inductances are expressed as follows [21], [31]:

$$L_{cs} = L_s - m_s \tag{1.27}$$

$$L_{cr} = L_r - m_r \tag{1.28}$$

$$M = \frac{3}{2} m_{sr} \tag{1.29}$$

$L_s$: Stator self-inductance for each phase.

$L_r$: Rotor self-inductance for each phase.

$m_s$: Mutual inductance between two stator phases.

$m_r$: Mutual inductance between two rotor phases.

$m_{sr}$: Mutual inductance between stator and rotor.

Figure 1.7 illustrates the equivalent circuit of DFIM where all variables and parameters are transferred to the stator side.

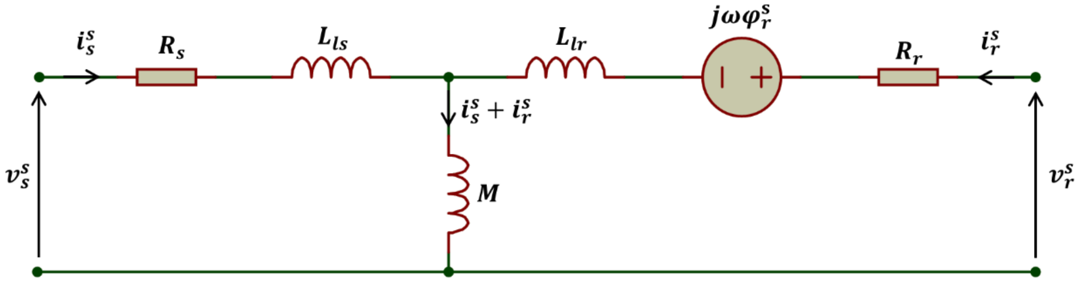

*Figure 1.7: Equivalent circuit of DFIM in stator coordinates.*

### 1.4.4 Modelling of DFIM in rotating frame

We are now going to implement the induction machine model in a rotating $dq$ reference frame. This reference is linked to the rotating flux which rotates at the angular speed of the stator currents $\omega_s$. Consequently, the obtained final model is that one corresponds to the result after Park's transformation Appendix A.

To perform a modelling for three-phase system, there is a direct approach which express the EMF in each phase. But this method requires the use of the phase-coupled and time-varied inductances. Fortunately, to avoid this problem and facilitate the analysis, we can use the Park's transformation. The advantage is that this approach yields to an analytical models based on $dq$ reference frame. This frame turns at the same speed of the rotating flux. Therefore the model will have a much simpler form and the inductances of the $dq$-axes are decoupled and constant.

We note that if we have a complex vector $x_{\alpha\beta} = x_\alpha + jx_\beta$ located in the stationary complex frame with an instantaneous angle noted $\zeta(t)$, then its complex vector $x = x_d + jx_q$ referred to synchroneous frame can be writen as mentioned in (1.30).

$$x = x_{\alpha\beta}.e^{-j\zeta(t)} \tag{1.30}$$

By applying (1.30) in (1.14) and taking into account the angular frequency of the stator flux density $\omega_s$, the relation of the complex vectors of the stator voltage, current and flux is done as mentioned in (1.31).

$$v_s e^{j\omega_s t} = R_s i_s e^{j\omega_s t} + \frac{d(\varphi_s e^{j\omega_s t})}{dt}$$

$$v_s e^{j\omega_s t} = R_s i_s e^{j\omega_s t} + \frac{d\varphi_s}{dt} e^{j\omega_s t} + j\omega_s \varphi_s e^{j\omega_s t}$$

$$v_s = R_s i_s + \frac{d\varphi_s}{dt} + j\omega_s \varphi_s \tag{1.31}$$

Similarly, we repeat the same steps, on the equation (1.15), for the rotor windings which have $\omega_r$ as an angular frequency.

$$v_r e^{j\omega_r t} = R_r i_r e^{j\omega_r t} + \frac{d(\varphi_r e^{j\omega_r t})}{dt}$$

$$v_r e^{j\omega_r t} = R_r i_r e^{j\omega_r t} + \frac{d\varphi_r}{dt} e^{j\omega_r t} + j\omega_r \varphi_r e^{j\omega_r t}$$

$$v = R_r i_r + \frac{d\varphi_r}{dt} + j\omega_r \varphi_r$$

$$v_r = R_r i_r + \frac{d\varphi_r}{dt} + j(\, \omega_s - \omega \,)\varphi_r \tag{1.32}$$

The relationship of the fluxes linkage and the currents are listed as follows:

$$\varphi_s = \varphi_m + \varphi_{ls} = M(i_s + i_r) + L_{ls} i_s = L_{cs} i_s + M i_r \tag{1.33}$$

$$\varphi_r = \varphi_m + \varphi_{lr} = M(i_s + i_r) + L_{lr} i_r = M i_s + L_{cr} i_r \tag{1.34}$$

Hence the last two equations (1.33) and (1.34), which describe the stator and rotor fluxes, can be written in $dq$ reference as the following:

$$\begin{cases} \varphi_{sd} = M(i_{sd} + i_{rd}) + L_{ls} i_{sd} = L_{cs} i_{sd} + M i_{rd} \\ \varphi_{sq} = M\left(i_{sq} + i_{rq}\right) + L_{ls} i_{sq} = L_{cs} i_{sq} + M i_{rq} \\ \varphi_{rd} = M(i_{sd} + i_{rd}) + L_{lr} i_{rd} = M i_{sd} + L_{cr} i_{rd} \\ \varphi_{rq} = M\left(i_{sq} + i_{rq}\right) + L_{lr} i_{rq} = M i_{sq} + L_{cr} i_{rq} \end{cases} \tag{1.35}$$

Concerning the stator and rotor voltages equations which are mentioned in (1.31) and (1.32) respectively, can be listed regarding to $dq$ reference in (1.36).

On the basis of (1.35) and (1.36), the equivalent circuit model in $dq$ reference frame is shown in Figure 1.8 regarding to $d - axis$ (also we have similar circuit for the $q - axis$).

$$\begin{cases} v_{sd} = R_s i_{sd} + \frac{d\varphi_{sd}}{dt} - \omega_s \varphi_{sq} \\ v_{sq} = R_s i_{sq} + \frac{d\varphi_{sq}}{dt} + \omega_s \varphi_{sd} \\ v_{rd} = R_r i_{rd} + \frac{d\varphi_{rd}}{dt} - (\omega_s - \omega)\varphi_{rq} \\ v_{rq} = R_r i_{rq} + \frac{d\varphi_{rq}}{dt} + (\omega_s - \omega)\varphi_{rd} \end{cases} \tag{1.36}$$

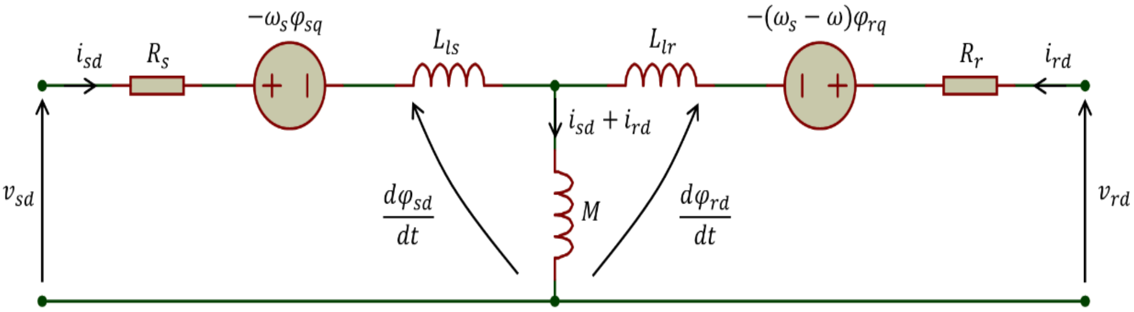

*Figure 1.8: Equivalent circuit of DFIM in the dq reference regarding to d-axis.*

The model in steady state can be easily obtained neglecting the derivatives of fluxes' linkage:

$$\begin{cases} \frac{d\varphi_s}{dt} = 0 \\ \frac{d\varphi_r}{dt} = 0 \end{cases} \tag{1.37}$$

So, by using (1.37) into (1.31) and (1.32), then rearranging them with the help of (1.33) and (1.34), we get as a result the equations (1.38) and (1.39) of the stator and rotor voltages which are more simplified. We remind that $s = \frac{\omega_s - \omega}{\omega_s}$ is the slip ratio of the machine.

$$v_s = (R_s + j\omega_s L_{ls})i_s + j\omega_s M(i_s + i_r) \tag{1.38}$$

$$v_r = (R_r + js\omega_s L_{lr})i_r + js\omega_s M(i_s + i_r) \tag{1.39}$$

Thus the circuit model of the DFIM in steady state is depicted in Figure 1.9.

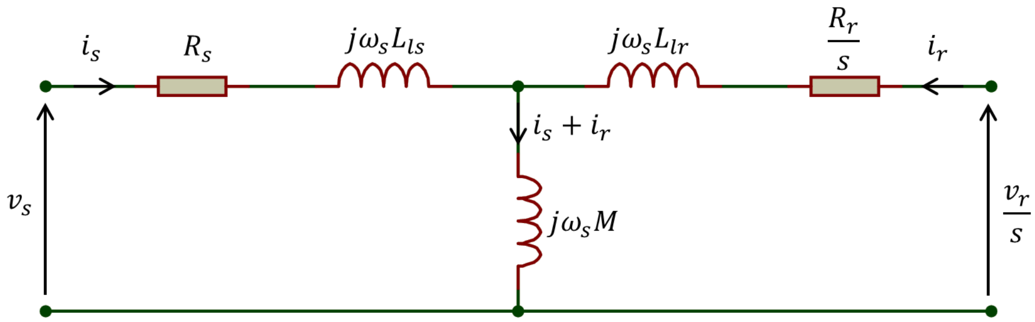

*Figure 1.9: DFIM circuit model in steady state.*

(1.35) and (1.36) can be reformulated in matrix form like listed in (1.40) and (1.41).

$$\begin{bmatrix} \varphi_{sd} \\ \varphi_{sq} \\ \varphi_{rd} \\ \varphi_{rq} \end{bmatrix} = \begin{bmatrix} L_{cs} & 0 & M & 0 \\ 0 & L_{cs} & 0 & M \\ M & 0 & L_{cr} & 0 \\ 0 & M & 0 & L_{cr} \end{bmatrix} \begin{bmatrix} i_{sd} \\ i_{sq} \\ i_{rd} \\ i_{rq} \end{bmatrix} \tag{1.40}$$

$$\begin{bmatrix} v_{sd} \\ v_{sq} \\ v_{rd} \\ v_{rq} \end{bmatrix} = \begin{bmatrix} R_s & 0 & 0 & 0 \\ 0 & R_s & 0 & 0 \\ 0 & 0 & R_r & 0 \\ 0 & 0 & 0 & R_r \end{bmatrix} \begin{bmatrix} i_{sd} \\ i_{sq} \\ i_{rd} \\ i_{rq} \end{bmatrix} + \begin{bmatrix} \frac{d}{dt} & -\omega_s & 0 & 0 \\ \omega_s & \frac{d}{dt} & 0 & 0 \\ 0 & 0 & \frac{d}{dt} & -\omega_r \\ 0 & 0 & \omega_r & \frac{d}{dt} \end{bmatrix} \begin{bmatrix} \varphi_{sd} \\ \varphi_{sq} \\ \varphi_{rd} \\ \varphi_{rq} \end{bmatrix} \tag{1.41}$$

By remanipulating equations (1.40) and (1.41), we can find the state-space representation as mentioned in (1.42) for this model. Noting that the stator and rotor currents represent the state variables and the output signals together as we have here:

$$\dot{x} = [A]x + [B]u \tag{1.42}$$

$x = [i_{sd} \quad i_{sq} \quad i_{rd} \quad i_{rq}]^T$ is the state vector and at the same time it contains the output signals (currents) for the model while $\dot{x} = \left[\frac{di_{sd}}{dt} \quad \frac{di_{sq}}{dt} \quad \frac{di_{rd}}{dt} \quad \frac{di_{rq}}{dt}\right]^T$ is its derivative, and $u = [v_{sd} \quad v_{sq} \quad v_{rd} \quad v_{rq}]^T$ represent the input (or control) vector of the DFIM. With regard to $[A]$ and $[B]$ matrices, they are the state (or system) and the input matrixes respectively. Both matrices are function of the stator and rotor parameters. In addition to that, $[A]$ is also depend on stator and rotor pulsation ($\omega_s$ and $\omega_r$) as following:

$$[A] = \begin{bmatrix} -\frac{R_s}{\sigma L_{cs}} & \frac{\omega_s+(\sigma-1)\omega_r}{\sigma} & \frac{(1-\sigma)R_r}{\sigma M} & \frac{M(\omega_s-\omega_r)}{\sigma L_{cs}} \\ \frac{-\omega_s-(\sigma-1)\omega_r}{\sigma} & -\frac{R_s}{\sigma L_{cs}} & \frac{-M(\omega_s-\omega_r)}{\sigma L_{cs}} & \frac{(1-\sigma)R_r}{\sigma M} \\ \frac{(1-\sigma)R_s}{\sigma M} & \frac{-M(\omega_s-\omega_r)}{\sigma L_{cr}} & -\frac{R_r}{\sigma L_{cr}} & \frac{-(\sigma-1)\omega_s-\omega_r}{\sigma} \\ \frac{M(\omega_s-\omega_r)}{\sigma L_{cr}} & \frac{(1-\sigma)R_s}{\sigma M} & \frac{(\sigma-1)\omega_s+\omega_r}{\sigma} & -\frac{R_r}{\sigma L_{cr}} \end{bmatrix}.$$

$$[B] = \begin{bmatrix} \frac{1}{\sigma L_{cs}} & 0 & \frac{\sigma-1}{\sigma M} & 0 \\ 0 & \frac{1}{\sigma L_{cs}} & 0 & \frac{\sigma-1}{\sigma M} \\ \frac{\sigma-1}{\sigma M} & 0 & \frac{1}{\sigma L_{cr}} & 0 \\ 0 & \frac{\sigma-1}{\sigma M} & 0 & \frac{1}{\sigma L_{cr}} \end{bmatrix}.$$

Noting that $\sigma = 1 - \frac{M^2}{L_{cs}L_{cr}}$ is the leakage or dispersion coefficient of the machine [32].

### 1.4.5 Mechanical equation

The fluxes generated by the stator interact with the rotor fluxes to produce an electromagnetic torque in the air gap. If the torque produced is large enough, the rotor starts to rotate; this phenomenon is described by Newton's Second Law for rotating bodies.

The fundamental principle of dynamics, described by Newton's second law, assumes that a body with a constant moment of inertia $J$ with respect to an axis of rotation has an angular acceleration. The latter is proportional to the sum of the applied torques on this body, and inversely proportional to its moment of inertia [33]. In the case of a rotating electrical machine, this principle is presented by this equation:

$$J\frac{d\Omega}{dt} = \frac{J}{p}\frac{d\omega}{dt} = T_{em} - T_L - f.\Omega \tag{1.43}$$

where $J$ is the moment of inertia of the rotor with the associated load, $\Omega$ is the mechanical angular velocity of the rotor, $T_{em}$ is the electromagnetic torque provided by the stator on the machine shaft, which is generated from the electromagnetic field. $T_L$ represents the torque exerted by the load while $f.\Omega$ is the friction torque ($f$ is the viscous friction coefficient of the DFIM).

### 1.4.6 Electromagnetic torque

The electromagnetic torque can be computed in several forms either according to stator and rotor currents by (1.44) or as a function of stator fluxes and currents by (1.45) or as a function of the rotor fluxes and currents by (1.46). Also it can be determined as function of the stator real power $P_s$ and the mechanical speed of the machine $\Omega$ by equation (1.47).

$$T_{em} = \frac{3}{2}pM\left(i_{sq}i_{rd} - i_{sd}i_{rq}\right) \tag{1.44}$$

$$T_{em} = \frac{3}{2}p\left(\varphi_{sd}i_{sq} - \varphi_{sq}i_{sd}\right) \tag{1.45}$$

$$T_{em} = \frac{3}{2}p\left(\varphi_{rq}i_{rd} - \varphi_{rd}i_{rq}\right) \tag{1.46}$$

$$T_{em} = \frac{P_s}{\Omega} \tag{1.47}$$

### 1.4.7 Powers of the machine

In addition to the stator real power $P_s$, rotor real power $P_r$ and the mechanical $P_m$ power that are illustrated in Figure 1.4, the machine has also two reactive powers $Q_s$, $Q_r$ at the stator and rotor sides. These powers are expressed in terms of the stator and rotor voltages and currents as follows:

$$P_s = \frac{3}{2}\left(v_{sd}i_{sd} + v_{sq}i_{sq}\right) \tag{1.48}$$

$$Q_s = \frac{3}{2}\left(v_{sq}i_{sd} - v_{sd}i_{sq}\right) \tag{1.49}$$

$$P_r = \frac{3}{2}\left(v_{rd}i_{rd} + v_{rq}i_{rq}\right) \tag{1.50}$$

$$Q_r = \frac{3}{2}\left(v_{rq}i_{rd} - v_{rd}i_{rq}\right) \tag{1.51}$$

Based on a simplified model of the machine, where copper and iron losses and magnetic leakages are neglected, the DFIM is characterized by the following:

$$P_r = s.P_s \tag{1.52}$$

$$P_m = P_s - P_r = P_s - s.P_s = (1-s)P_s \tag{1.53}$$

Figure 1.10 presents the real power transfer between stator, rotor and shaft of the ideal model of the DFIM in generating mode for (a) super-synchronism and (b) sub-synchronism cases.

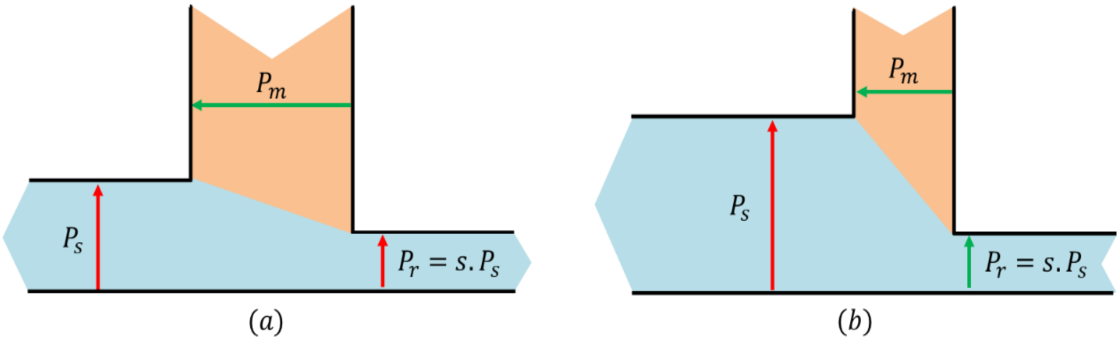

*Figure 1.10: Real power balance for ideal model of DFIM in generating mode.*

### 1.4.8 Block diagram of DFIM

The block diagram of the DFIM displayed in Figure 1.11 is obtained based on the voltages, fluxes and electromagnetic torque equations depicted in (1.31), (1.32), (1.33), (1.34) and (1.44). Note that $v_s = (v_{sd}, v_{sq})$, $v_r = (v_{rd}, v_{rq})$, $i_s = (i_{sd}, i_{sq})$, $i_r = (i_{rd}, i_{rq})$, $\varphi_s = (\varphi_{sd}, \varphi_{sq})$, and $\varphi_r = (\varphi_{rd}, \varphi_{rq})$.

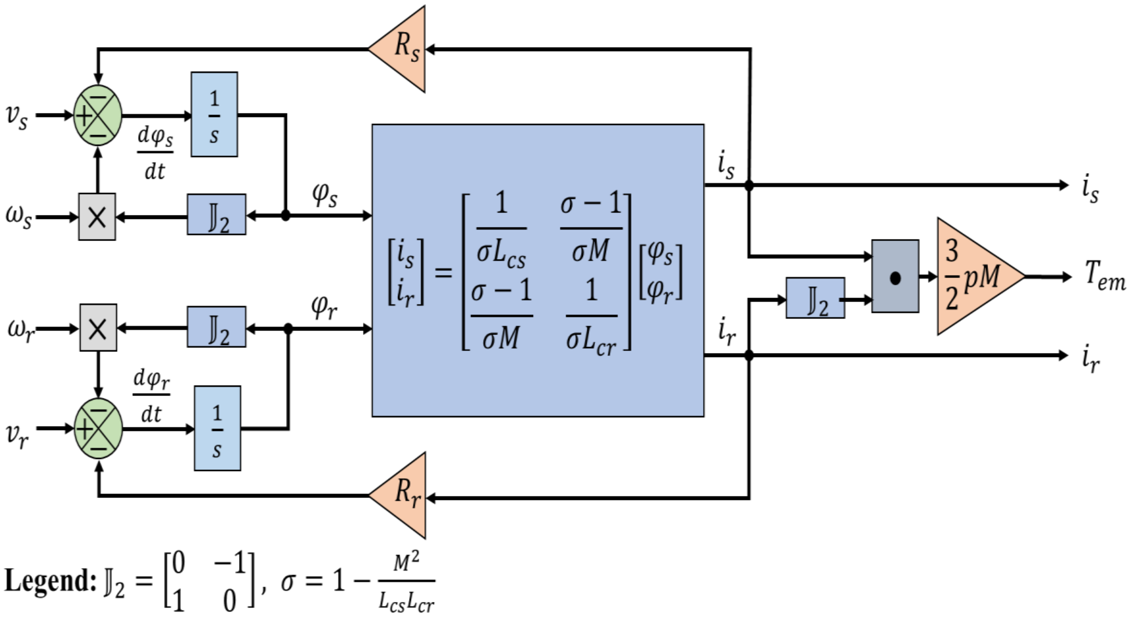

*Figure 1.11: Block diagram of the DFIM.*

## 1.5 Free acceleration test as SCIM

In order to validate the implementation under Matlab/Simulink of the mathematical model for the DFIM, we have simulated its behavior in open loop operation mode where the stator windings are supplied with sinusoidal voltages (at a constant frequency) and with shorted rotor windings. This test is performed at no load and as a consequence, it is called *free acceleration case*. Then to analyze the results of this test, it can be compared to the Torque-Speed characteristic of the classical (squirrel-cage) induction machine. The machine parameters are shown in Appendix B.

Figure 1.12 illustrates the torque-speed or torque-slip curves ($s = 1 - \frac{\Omega}{\Omega_s}$) for the induction machine in three modes of operation. Generating mode when $s < 0$ (or $\Omega_s < \Omega$), motoring mode when $0 < s < 1$ (or $0 < \Omega < \Omega_s$) and braking mode in the case of $1 < s$ (or the machine doesn't turn). This characteristic of the machine is described by the equation (1.54).

$$T_{em} = \frac{2T_{max}}{\frac{s}{s_{max}} + \frac{s_{max}}{s}} \qquad (1.54)$$

Where $T_{max}$ is the maximal torque of the machine and $s_{max}$ is slip ratio corresponding to $T_{max}$. They are function of the machine parameters.

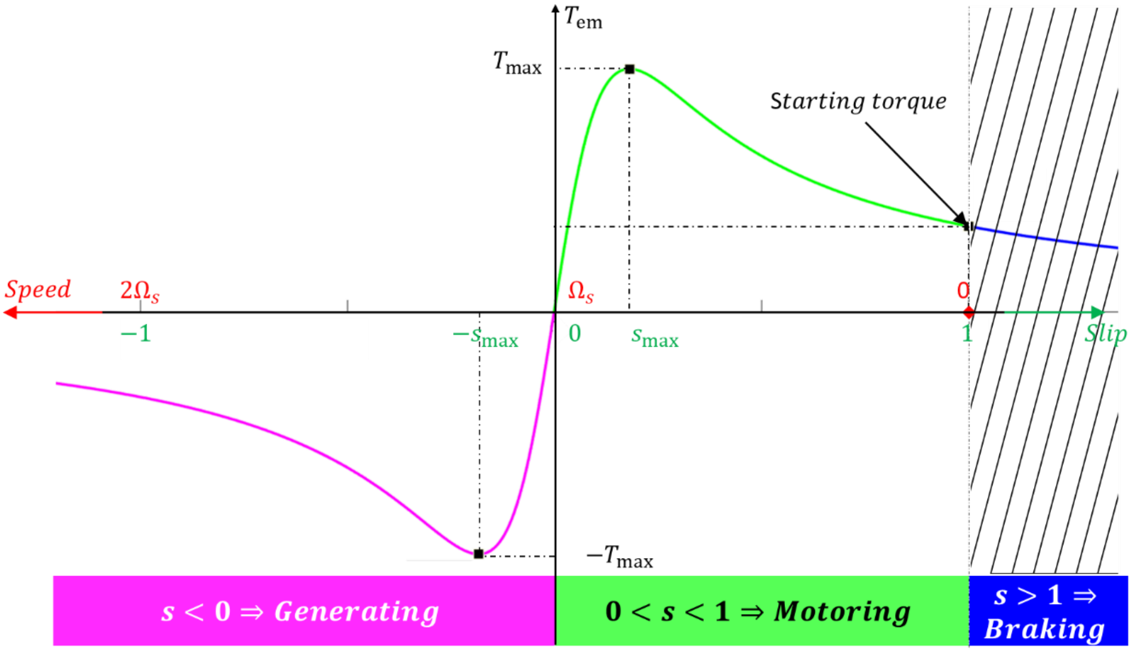

*Figure 1.12:Induction machine Torque-Speed/Slip curve.*

The result for this test is illustrated in Figure 1.13 and Figure 1.14. First figure presents the variation of the torque and the speed while the second figure illustrates the stator and rotor currents.

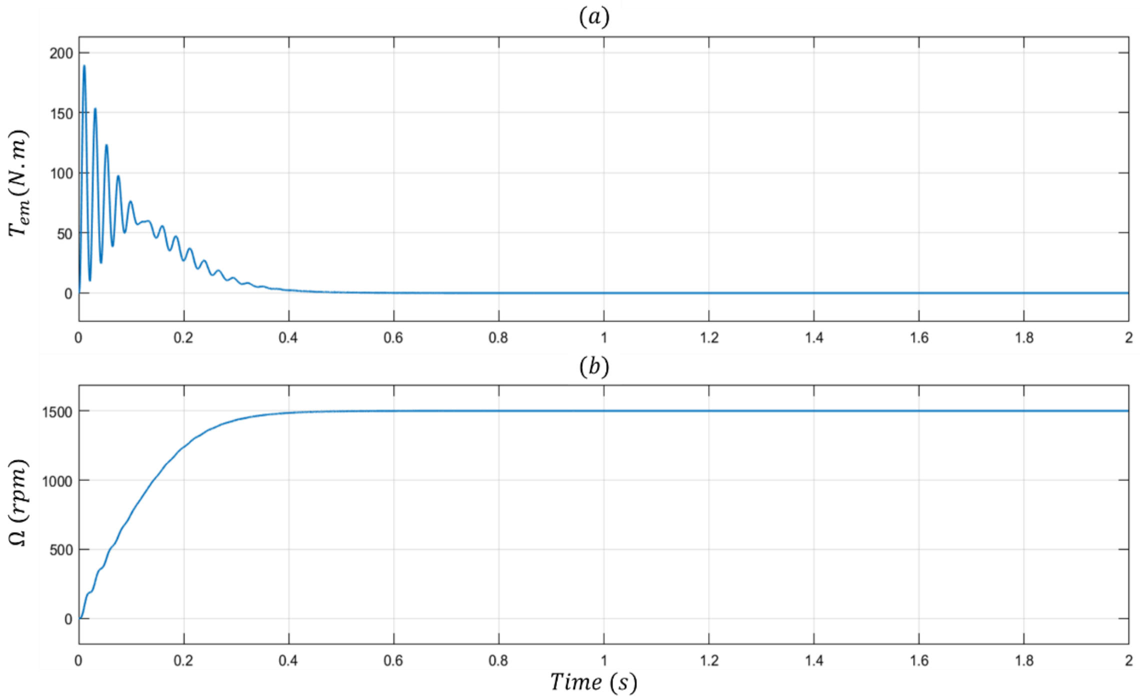

*Figure 1.13: (a) Electromganetic torque and (b) speed of DFIM in free acceleration case.*

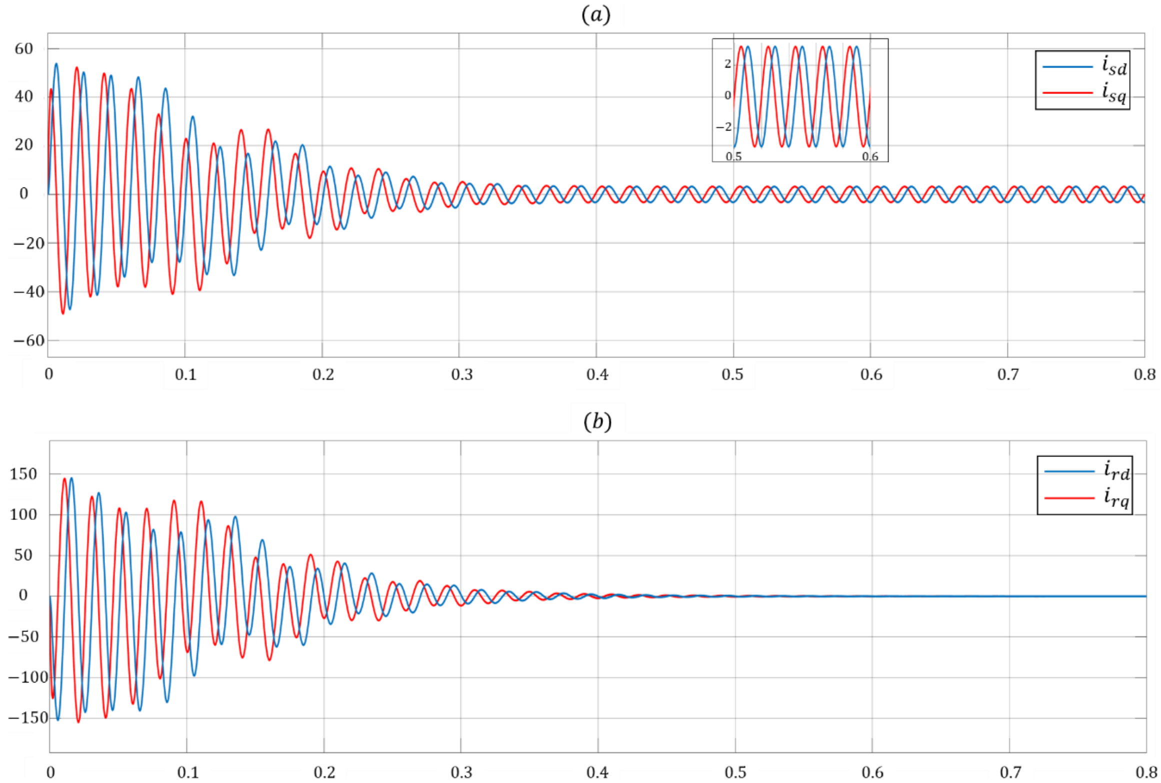

*Figure 1.14: (a) Stator and (b) rotor currents of the machine in free acceleration case.*

When comparing the results of Figure 1.13 with the torque-speed characteristic shown in Figure 1.12, we can notice that at steady state the torque converges to zero when the speed reaches its synchronism value $\Omega_s = 1500\, rmp$. Also, there is a starting torque when the machine starts turning. So it can be deduced that the results of speed and torque in Figure 1.13 comply with the torque-speed curve characteristic in Figure 1.12.

By reference to equation (1.44), the torque can't be zero, unless the stator and/or the rotor currents are zeros. However, the stator currents cannot be null because of the voltage supply at the stator side. Therefore, at the steady state, when the torque becomes null, the rotor currents should be null too. And this is what we can see clearly at steady-state in Figure 1.14 where the stator currents stay different from zero while the rotor currents become zero.

## 1.6 Conclusion

In this chapter, the DFIM principle is presented, its mathematical model is performed and proved in the case of free acceleration while there is no mechanical torque applied on the machine shaft and the rotor windings are short-circuited. Also, it has been seen that the DFIM has two main advantages over the conventional induction machine. The first is the production of electrical power regardless of the rotational speed (sub or super synchronism), while the second is the recovery of slip power.

In the next chapter, the control of the machine will be treated in order to be able to insert the machine in the back-to-back converter system as a load.

# Chapter 2: Control of DFIM

## 2.1 Introduction

The previous chapter highlighted the importance of using DFIM in wind turbine application since the DFIM is able to operate at variable speed following the optimal power characteristic of the wind turbine. This characteristic indicates that for each wind speed, there is an optimal rotation speed allowing the wind turbine getting the best possible efficiency. To be able to run at this optimal angular velocity, at a given wind speed, the turbine must have a given mechanical resistant torque, i.e. a real power output by the DFIM. It is by using this power reference that the machine can then be controlled.

In the following paragraph, we will therefore recalculate the equations that describe the relationship between the real and reactive stator powers and the rotor variables that can be controlled. This is known as rotor side control.

## 2.2 Rotor Side Control

### 2.2.1 State of art

In the literature, the control methods of variable frequency drives can be classified into two categories, vector control and scalar control (Figure 2.1). Among all methods developed for the IM, the most commonly used techniques are the Field-Oriented Control (FOC) techniques and Direct Torque Control (DTC) techniques. In many IM applications, vector control is the most widely used technique because of its high performance [34].

The vector control theory is based on the acquisition of the magnitude and phase of voltages or currents for the control of IMs. The vector control is thus based on regulating the direction of the IM's flux, voltage, and current vectors. This control has been achieved for DFIM in many ways [27]. Controlling the rotor currents by Stator-Flux Orientation (SFO) [35], [36] or air-gap-flux orientation [37], [38] is a common way. SFO gives orientation also with the stator voltage as we will see in section 2.2.4, if the resistance of stator windings is small enough [39], [40].

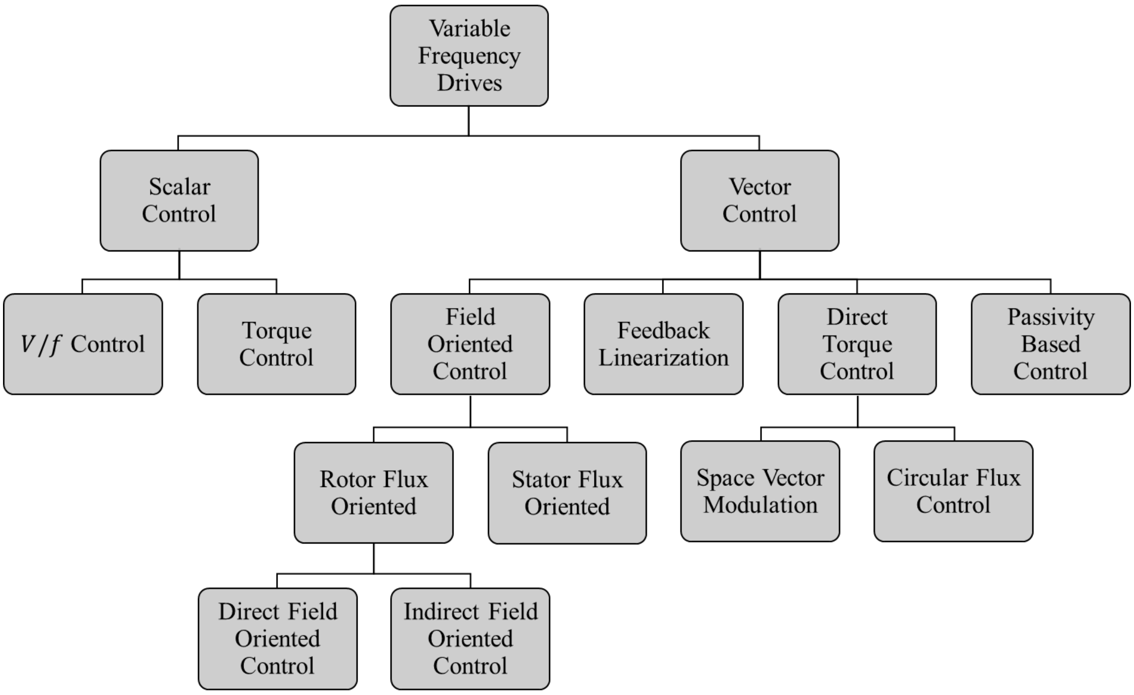

*Figure 2.1:Categorization of variable frequency drive methods [34].*

In this thesis, SFO concept is adopted to control the rotor current. In this case, the torque is only dependent on the quadrature rotor current component in steady state as it will be proved next in (2.28) and (2.29).

### 2.2.2 Synchronous reference frame

For the purpose of controlling the rotor side variables of the machine, the relationships between the rotor currents and the stator powers will be determined. Then, the closed control loops for the currents will be performed.

The real and reactive stator powers can be controlled independently by varying quadrature current $i_{rq}$ and direct current $i_{rd}$ respectively. This can be achieved thanks to the linking between stator flux with $d-axis$ of the $dq$ reference frame as illustrated in Figure 2.2.

$\theta_s$ and $\theta_r$ are the electrical angles of the stator rotating field with regard to the stator and to the rotor reference frame respectively. While $p.\theta$ is the electrical angle between the stator and the rotor. These angles are linked according to (2.1).

$$\theta_s = \theta_r + p.\theta \tag{2.1}$$

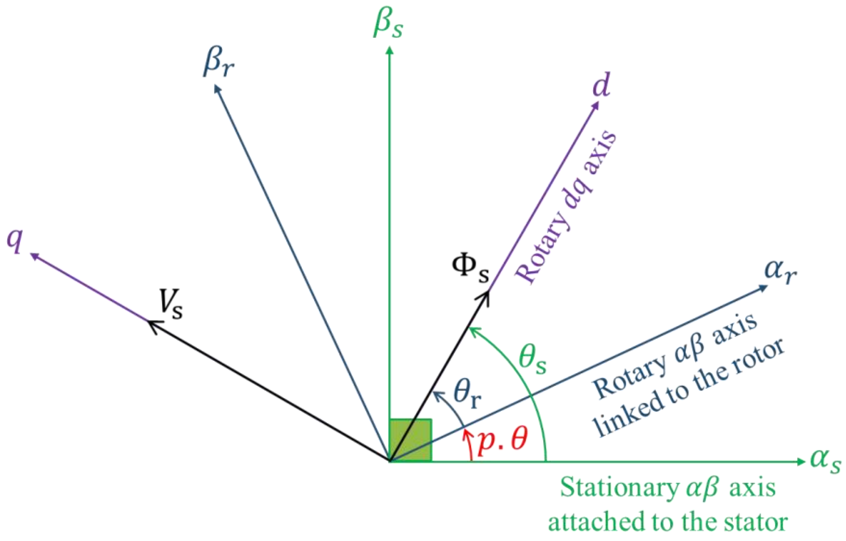

*Figure 2.2: Reference frame linked to the stator rotating flux.*

### 2.2.3 Phase-locked loop

In order to find the required angle $\theta_s$ for Park transformations, we opted for a Synchronous Reference Frame Phase Locked Loop (SRF-PLL), which is the most popular and widely used technique for extraction of grid voltage phase, frequency, and amplitude in three-phase systems [41].

The basic idea of the PLL system is a non-linear feedback control system that synchronizes its output frequency as well as its phase with its input. The input are the three-phase grid voltages and the output from the PLL is the phase angle of one of the three phases [42]. PLLs are now widely used for the synchronization of power electronic converters as well as for monitoring and control purposes in various technical fields [41].

For the three-phase system, the PLL principle is presented in [27]–[33]. Advanced PLL techniques seek robust methods that allow finding the frequency and the angle of the network despite the existence of disturbances. The main disturbances are: phase shift, troughs and bumps in voltage, harmonics, frequency shift [50].

The structure of the PLL is very diversified, but always includes three blocks: phase detector, loop filter or corrector and Voltage Controlled Oscillator (VCO). Figure 2.3 shows the schematic diagram of the conventional SRF-PLL, the input signal is denoted by $(v_a, v_b, v_c)$ while the output phase is denoted by $\theta_s$.

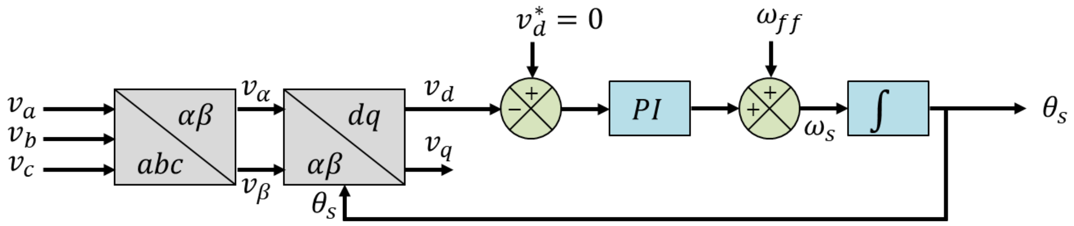

*Figure 2.3: Block diagram structure of a three phase SRF-PLL.*

### 2.2.4 DFIG modelling under SFO concept

With the aim of obtaining a decoupled control of real and reactive stator powers, the DFIG model requires all values to be computed under the Stator-Flux Orientation (SFO) or Field Oriented Control (FOC) concept. The stator flux equations can be then simplified to equations (2.2) thanks to the linking between stator flux with $d-axis$ of the $dq$ reference frame as illustrated in Figure 2.2.

$$\begin{cases} \varphi_{sd} = \Phi_s = constant \\ \varphi_{sq} = 0 \end{cases} \tag{2.2}$$

$\Phi_s$: is the peak value of the stator flux.

If the stator resistance $R_s$ is neglected, which is a fairly realistic assumption for medium and high power machines used in wind energy [51], in addition to the simplified stator flux described in (2.2), the stator voltage expressions, already computed in (1.36) become simpler as indicated in (2.3).

$$\begin{cases} v_{sd} = 0 \\ v_{sq} = \omega_s \Phi_s = V_s \end{cases} \tag{2.3}$$

Where $V_s$ represents the peak value of the stator voltage.

We can notice from equation (2.3) that the stator voltage is linked to $q-axis$ ($v_{sd} = 0$). Hence, the stator voltage and the stator flux rotate at the same angular velocity in the $dq$ frame with a phase-shift angle of $\pi/2$ , because they are attached to $q-axis$ and $d-axis$ respectively as illustrated in Figure 2.2.

Based on (2.3) the stator flux can be expressed by:

$$\Phi_s = \frac{V_s}{\omega_s} \tag{2.4}$$

After some rearrangements of the obtained stator flux equations in (1.35) as illustrated in (2.5) and (2.6), the stator current components can be written as function of the rotor current components as shown in (2.7).

$$\begin{cases}\varphi_{sd} = L_{cs} i_{sd} + M i_{rd} = \Phi_s \\ \varphi_{sq} = L_{cs} i_{sq} + M i_{rq} = 0\end{cases} \tag{2.5}$$

$$\begin{cases} i_{sd} = -\dfrac{M}{L_{cs}} i_{rd} + \dfrac{1}{L_{cs}} \Phi_s \\ i_{sq} = -\dfrac{M}{L_{cs}} i_{rq}\end{cases} \tag{2.6}$$

$$\begin{cases} i_{sd} = -\dfrac{M}{L_{cs}} i_{rd} + \dfrac{1}{L_{cs}} \dfrac{V_s}{\omega_s} \\ i_{sq} = -\dfrac{M}{L_{cs}} i_{rq}\end{cases} \tag{2.7}$$

Then the electromagnetic torque as computed in (1.44) and (1.45) is simplified into (2.8). This equation demonstrates that the control of the electromagnetic torque is possible by controlling the quadrature rotor current $i_{rq}$.

$$T_{em} = -\frac{3.p.V_s.M}{2.\omega_s.L_{cs}}.i_{rq} \tag{2.8}$$

By rearranging the rotor flux components cited in (1.35) using the stator current components in (2.7), the rotor flux components are expressed as in (2.9).

$$\begin{cases} \varphi_{rd} = \sigma L_{cr} i_{rd} + \dfrac{M}{L_{cs}} \dfrac{V_s}{\omega_s} \\ \varphi_{rq} = \sigma L_{cr} i_{rq}\end{cases} \tag{2.9}$$

Recalling that $\sigma = 1 - \frac{M^2}{L_{cs}.L_{cr}}$ is dispersion coefficient.

By substituting (2.9) into (1.36), the rotor voltage equations become:

$$\begin{cases} v_{rd} = R_r i_{rd} + \sigma L_{cr} \dfrac{di_{rd}}{dt} + e_{rd} \\ v_{rq} = R_r i_{rq} + \sigma L_{cr} \dfrac{di_{rq}}{dt} + e_{rq} + e_{\varphi}\end{cases} \tag{2.10}$$

With the following Electro-Motive Force (EMF):

$$e_{rd} = -\sigma\, L_{cr}\, \omega_r\, i_{rq} \tag{2.11}$$

$$e_{rq} = \sigma\, L_{cr}\, \omega_r\, i_{rd} \tag{2.12}$$

$$e_{\varphi} = \frac{M}{L_{cs}} \frac{\omega_r}{\omega_s} V_s \tag{2.13}$$

The rotor current components can be expressed then by (2.14).

$$\begin{cases} \sigma L_{cr} \dfrac{di_{rd}}{dt} + R_r i_{rd} = v_{rd} - e_{rd} \\ \sigma L_{cr} \dfrac{di_{rq}}{dt} + R_r i_{rq} = v_{rq} - e_{rq} - e_{\varphi} \end{cases} \tag{2.14}$$

Transforming equation (2.14) from time domain into frequency domain yields to (2.15).

$$\begin{cases} i_{rd} = \dfrac{1}{R_r + \sigma L_{cr} s} (v_{rd} - e_{rd}) \\ i_{rq} = \dfrac{1}{R_r + \sigma L_{cr} s} (v_{rq} - e_{rq} - e_{\varphi}) \end{cases} \tag{2.15}$$

Where $s$ is a complex number frequency parameter in Laplace domain.

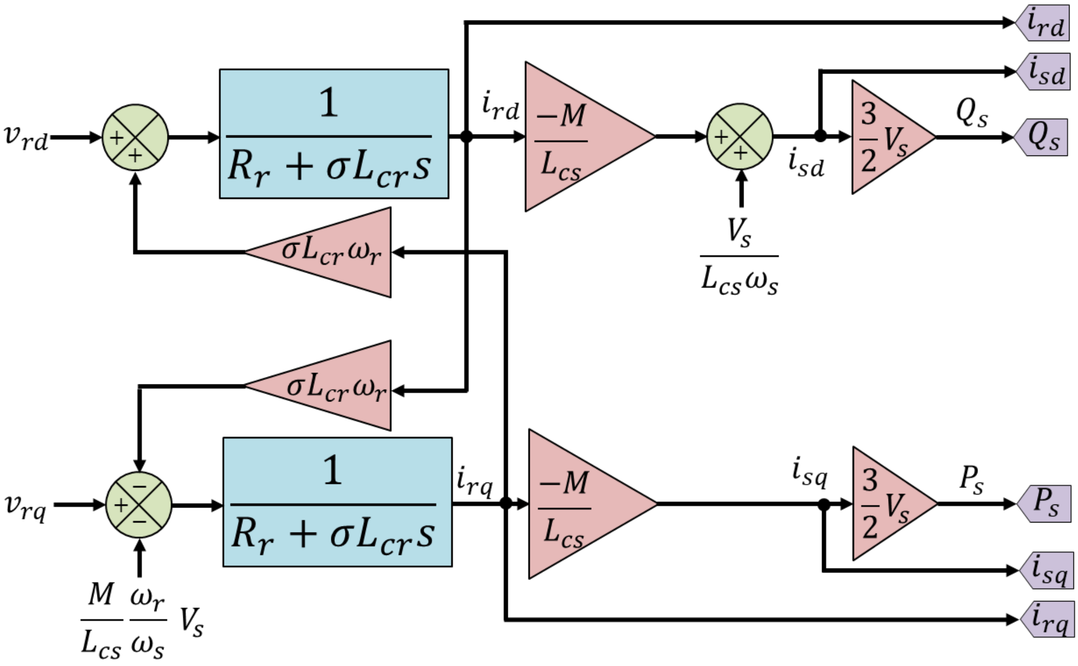

*Figure 2.4: Simplified block diagram of the DFIM in SRF.*

From (2.15), it is observed that the desired rotor current components $i_{rd}$ and $i_{rq}$ can be regulated by the rotor voltages $v_{rd}$ and $v_{rq}$ respectively. The terms $e_{rd} = -\sigma\, L_{cr}\, \omega_r\, i_{rq}$ and $e_{rq} = \sigma\, L_{cr}\, \omega_r\, i_{rd}$ represent the coupling terms, while $e_{\varphi} = \frac{M}{L_{cs}} \frac{\omega_r}{\omega_s} V_s$ represents the EMF [32]. These terms can be compensated in the control strategy [20]. Figure 2.4

illustrates the simplified block diagram of DFIM in SRF.

### 2.2.5 Control structure of the system

Proportional-Integral (PI) controllers are widely used in industry due to their performance and calculation speed. Their operating principle is to compare the actual measured values with the reference or desired values and to stabilize the system to be regulated. PI control combines the advantages of integral control (zero steady-state error) with those of proportional control (increasing the speed of the transient response) [52]–[55].

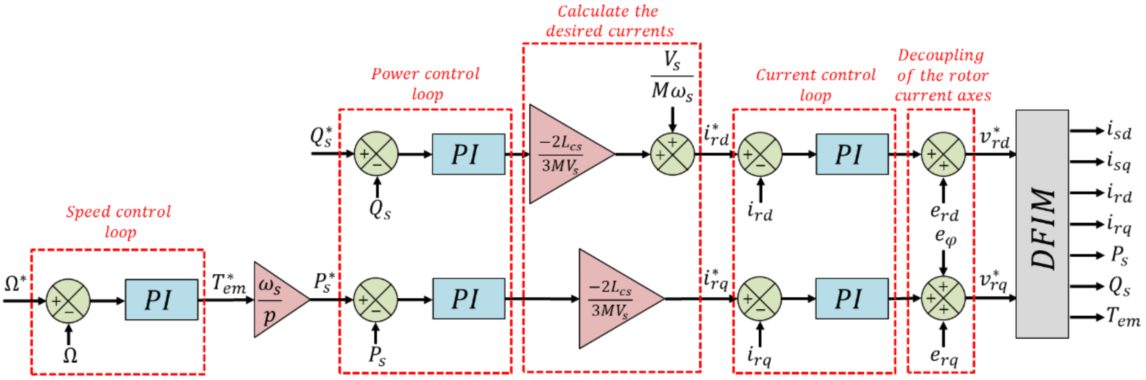

*Figure 2.5: Rotor side  control of the DFIM.*

Figure 2.5 illustrates the rotor side control structure of the DFIM. It consists of three imbricated control loop: $i_{rd}$ and $i_{rq}$ current regulation, real and reactive power regulation and speed regulation. When tuning the PI controllers, the disturbances variables ($e_{rd}, e_{rq}, e_\varphi$ and $T_L$) are assumed to be well compensated in the global structure of the system. Therefore, they are not considered while calculating the controller parameters. This assumption allows to simplify the loops as depicted in Figure 2.6, Figure 2.8 and Figure 2.7.

#### 2.2.5.1 Current controllers

According to the DFIM model equations (2.15); the simplified bloc diagram of current control loop can be drawn as shown in Figure 2.6.

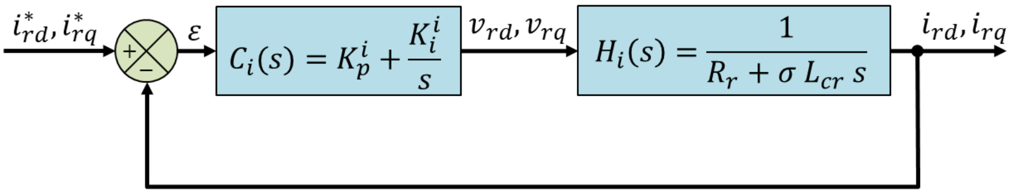

*Figure 2.6: Current regulation using PI controller.*

$\varepsilon$*: is* the error between the measured output signal and its desired value.

$C_i(s)$ and $H_i(s)$ are respectively the controller and the process transfer functions.

Let $G_i(s)$ is the open-loop transfer function and $F_i(s)$ is the closed-loop transfer function, therefore the expression of $G_i(s)$ is:

$$G_i(s) = C_i(s).H_i(s) \tag{2.16}$$

$$G_i(s) = \left(K_p^i + \frac{K_i^i}{s}\right)\left(\frac{1}{R_r + \sigma L_{cr} s}\right)$$

$$G_i(s) = \left(\frac{K_i^i\left(1 + \frac{K_p^i}{K_i^i} s\right)}{s}\right)\left(\frac{\frac{1}{R_r}}{1 + \frac{\sigma L_{cr}}{R_r} s}\right)$$

$$G_i(s) = \frac{K_i^i}{R_r s}\left(1 + \frac{K_p^i}{K_i^i} s\right)\left(\frac{1}{1 + \frac{\sigma L_{cr}}{R_r} s}\right) \tag{2.17}$$

When finding the controller parameters $K_p^i$ and $K_i^i$, the dominant-pole compensation method is used. It yields to:

$$\frac{K_p^i}{K_i^i} = \frac{\sigma L_{cr}}{R_r} \tag{2.18}$$

Therefore:

$$G_i(s) = \frac{K_i^i}{R_r s}\cancel{\left(1 + \frac{\sigma L_{cr}}{R_r} s\right)}\left(\frac{1}{\cancel{1 + \frac{\sigma L_{cr}}{R_r} s}}\right)$$

$$G_i(s) = \frac{K_i^i}{R_r\, s} \tag{2.19}$$

Concerning $F_i(s)$, it can be computed by using $G_i(s)$ as mentioned in (2.20).

$$F_i(s) = \frac{G_i(s)}{1 + G_i(s)} \tag{2.20}$$

$$F_i(s) = \frac{\frac{K_i^i}{R_r s}}{1 + \frac{K_i^i}{R_r s}}$$

$$F_i(s) = \frac{1}{1 + \frac{R_r}{K_i^i}.s} \tag{2.21}$$

$F_i(s)$ represents the first order transfer function of type $\frac{1}{1+\tau_i.s}$; $\tau_i$ is the desired current time constant. By identification, we obtain:

$$K_i^i = \frac{R_r}{\tau_i} \tag{2.22}$$

By replacing $K_i^i$ value computed by (2.22) in equation (2.18), $K_p^i$ is written as a function of $\sigma$, $L_{cr}$ and $\tau_i$:

$$K_p^i = \frac{\sigma L_{cr}}{\tau_i} \tag{2.23}$$

**Desired rotor current values:**

With the aim of controlling the system, there is still a need to find the reference rotor currents which will be the input of the controllers. By rearranging (1.48) and (1.49) using equations (2.3) and (2.7), the stator real and reactive powers are written as function of the direct and quadrature rotor currents as following:

$$\begin{cases} P_s = \frac{3}{2}(\cancel{v_{sd} i_{sd}} + \overbrace{v_{sq}}^{V_s}\, i_{sq}) \\ Q_s = \frac{3}{2}(\overbrace{v_{sq}}^{V_s}\, i_{sd} - \cancel{v_{sd} i_{sq}}) \end{cases} \tag{2.24}$$

$$\begin{cases} P_s = \frac{3}{2} V_s i_{sq} \\ Q_s = \frac{3}{2} V_s i_{sd} \end{cases} \tag{2.25}$$

$$\begin{cases} P_s = \frac{3}{2} V_s \left(-\frac{M}{L_{cs}} i_{rq}\right) \\ Q_s = \frac{3}{2} V_s \left(-\frac{M}{L_{cs}} i_{rd} + \frac{1}{L_{cs}} \frac{V_s}{\omega_s}\right) \end{cases} \tag{2.26}$$

$$\begin{cases} P_s = -\dfrac{3\,M\,V_s}{2\,L_{cs}} i_{rq} \\ Q_s = -\dfrac{3\,M\,V_s}{2\,L_{cs}} i_{rd} + \dfrac{3\,V_s^2}{2\,L_{cs}\,\omega_s} \end{cases} \tag{2.27}$$

We deduce from equations (2.27) that:

- ✓ The control of the stator reactive power is possible by controlling the $i_{rd}$ current.
- ✓ The control of the stator real power is possible by controlling the $i_{rq}$ current.

Hence, the rotor desired currents can be expressed as function of the desired stator powers by (2.28):

$$\begin{cases} i_{rd}^* = -\dfrac{2\,L_{cs}}{3\,M\,V_s}\, Q_s^* + \dfrac{V_s}{M\,\omega_s} \\ i_{rq}^* = -\dfrac{2\,L_{cs}}{3\,M\,V_s}\, P_s^* \end{cases} \tag{2.28}$$

Also the reference value for the stator real power $P_s^*$ is given by:

$$P_s^* = \Omega.T_{em}^* = \frac{\omega_s}{p}.T_{em}^* \tag{2.29}$$

### 2.2.5.2 Power controller

Figure 2.7 illustrates the power control loop. For this loop, the power controller parameters $K_p^P$ and $K_i^P$ are mentioned in (2.30) and (2.31). They are obtained by following the same steps taken for current controller.

$$K_p^P = \frac{2.\sigma.L_{cr}.L_{cs}}{3.V_s.M.\tau_P} \tag{2.30}$$

$$K_i^P = \frac{2.R_r.L_{cs}}{3.V_s.M.\tau_P} \tag{2.31}$$

Where $\tau_p$ represents the constant time for the power loops.

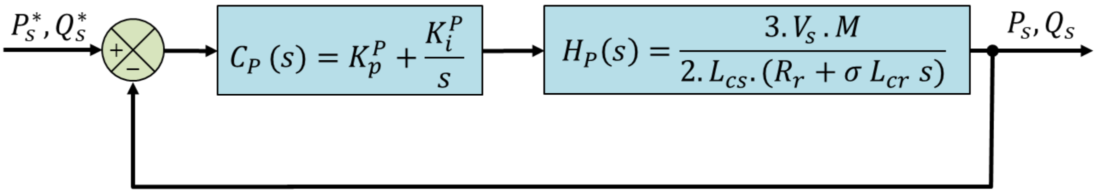

*Figure 2.7: Power control loop.*

#### 2.2.5.3 Speed regulation

The speed control loop is given by Figure 2.8.

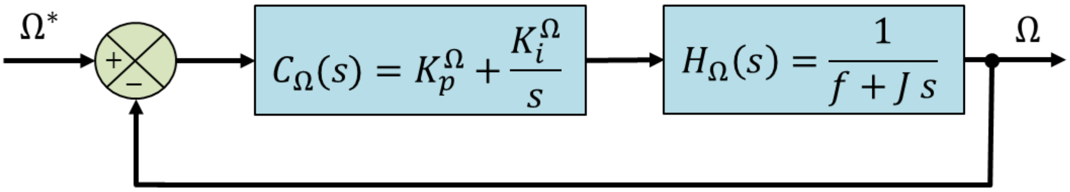

*Figure 2.8: Speed control loop.*

The transfer function of the PI speed controller $C_\Omega(s)$ and the system transfer function $H_\Omega(s)$ are:

$$C_\Omega(s) = K_p^\Omega + \frac{K_i^\Omega}{s} \tag{2.32}$$

$$H_\Omega(s) = \frac{1}{f + Js} \tag{2.33}$$

Then the open-loop transfer function $G_\Omega(s)$ is computed by:

$$G_\Omega(s) = C_\Omega(s).H_\Omega(s) \tag{2.34}$$

$$G_\Omega(s) = \left(K_p^\Omega + \frac{K_i^\Omega}{s}\right)\left(\frac{1}{f + Js}\right)$$

$$G_\Omega(s) = \left(\frac{K_i^\Omega\left(1 + \frac{K_p^\Omega}{K_i^\Omega}s\right)}{s}\right)\left(\frac{\frac{1}{f}}{1 + \frac{J}{f}s}\right)$$

$$G_\Omega(s) = \frac{K_i^\Omega}{fs}\left(1 + \frac{K_p^\Omega}{K_i^\Omega}s\right)\left(\frac{1}{1 + \frac{J}{f}s}\right) \tag{2.35}$$

In this case too, the dominant-pole compensation method yields to:

$$\frac{K_p^\Omega}{K_i^\Omega} = \frac{J}{f} \tag{2.36}$$

$$G_\Omega(s) = \frac{K_i^\Omega}{fs} \tag{2.37}$$

As the current controller, here also $F_{\Omega}(s)$ related to $G_{\Omega}(s)$ by (2.38) which helps finding its expression in (2.39).

$$F_{\Omega}(s) = \frac{G_{\Omega}(s)}{1 + G_{\Omega}(s)} \tag{2.38}$$

$$F_{\Omega}(s) = \frac{1}{1 + \frac{f}{K_i^{\Omega}}.s} \tag{2.39}$$

Under the assumption of a first order speed dynamic, $F_{\Omega}(s) = \frac{1}{1 + \tau_{\Omega} s}$; where $\tau_{\Omega}$ is the desired speed time constant, the speed controller parameters are :

$$K_i^{\Omega} = \frac{f}{\tau_{\Omega}} \tag{2.40}$$

$$K_p^{\Omega} = \frac{J}{\tau_{\Omega}} \tag{2.41}$$

## 2.3 Grid side control

The Grid Side Converter (GSC) is often controlled to operate at unity power factor and to regulate the DC-bus voltage [56]. For GSC, the use of a control method with a reference frame aligned along the inverter ac voltage is adopted, so the real and reactive powers transferred from the machine to the grid can be independently controlled. As shown in Figure 2.9, the grid side control includes outer loop that aims to control the DC-bus voltage, while the inner loop regulates the $dq$-axis decoupling current components. The output of this block diagram defines the three-phase reference voltages that should be delivered to the PWM controller in order to command the converter connected to the grid.

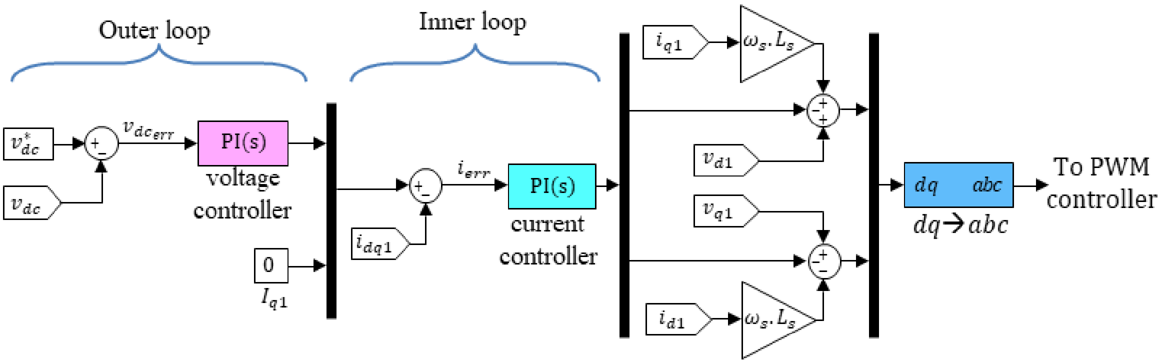

*Figure 2.9: Grid side control.*

## 2.4 Performance analysis of the control

This paragraph will allow to test the performance of the DFIG control and compare the obtained values with their references values for the different parameters. The simulation is performed when the machine is connected to an ideal source for the following scenario:

- Sub-synchronous mode $[0{,}1s]$.
- Super-synchronous mode $[1s, 2s]$.

Concerning the reference stator active power, its value was $P_s^* = -3500\ W$ at $t = 0s$. After $t = 1s$, it has decreased from $P_s^* = -3500\ W$ until it has arrived $P_s^* = -5500\ W$ ($P_s^*$ is negative during the operation of the machine, hence the DFIM operates in generator mode). Regarding the reference value of the reactive power, there was no demand for reactive power at the stator at the beginning. Between $t = 0.2s$ and $t = 0.6s$, $Q_s^* = 1000VAR$ is injected into the stator; then the reactive power was generated out of the stator from $t = 0.6s$ up to $t = 1s$. The evolution for the stator reactive power in the interval $[1s; 2s]$ is identical to the evolution between $t = 0s$ and $t = 1s$.

Figure 2.10 illustrates the variation of the stator active and reactive powers, also the electromechanical torque. The result demonstrates that the effective values converge towards the desired values.

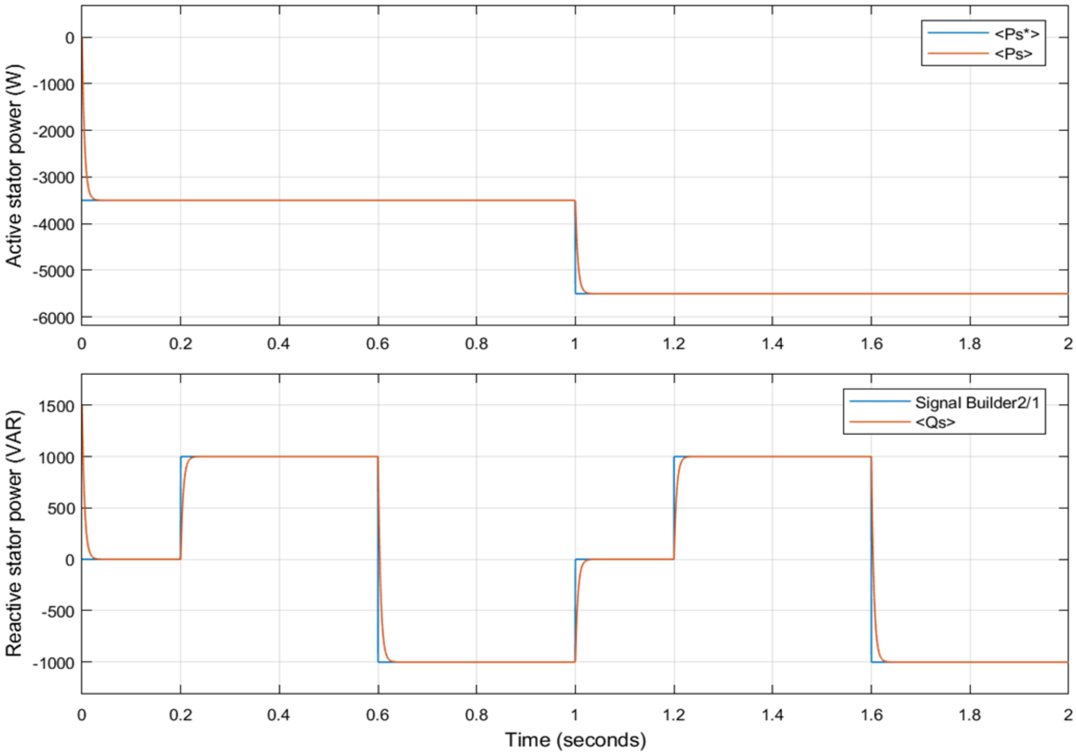

*Figure 2.10: Results of the stator powers.*

Figure 2.11 depicts the plot of active and reactive powers on both sides: rotor and stator. Remembering that active power at stator $P_s$ is negative all the time because the DFIM is running as generator. This power changes during the time at rotor side, but globally its value is positive ($P_r > 0$) when $0 < t < 1s$ and negative ($P_r < 0$) when $1s < t < 2s$. Hence the machine operates in sub-synchronous mode in the first sequence of the testing cycle, where there is a need to generate more power in order to rotate at synchronous speed. While in the second stage of time of running, the machine operates in super-synchronous mode, because part of the generated power from the machine is transferred to the main grid via rotor side with the aim of the machine turns at the synchronous frequency.

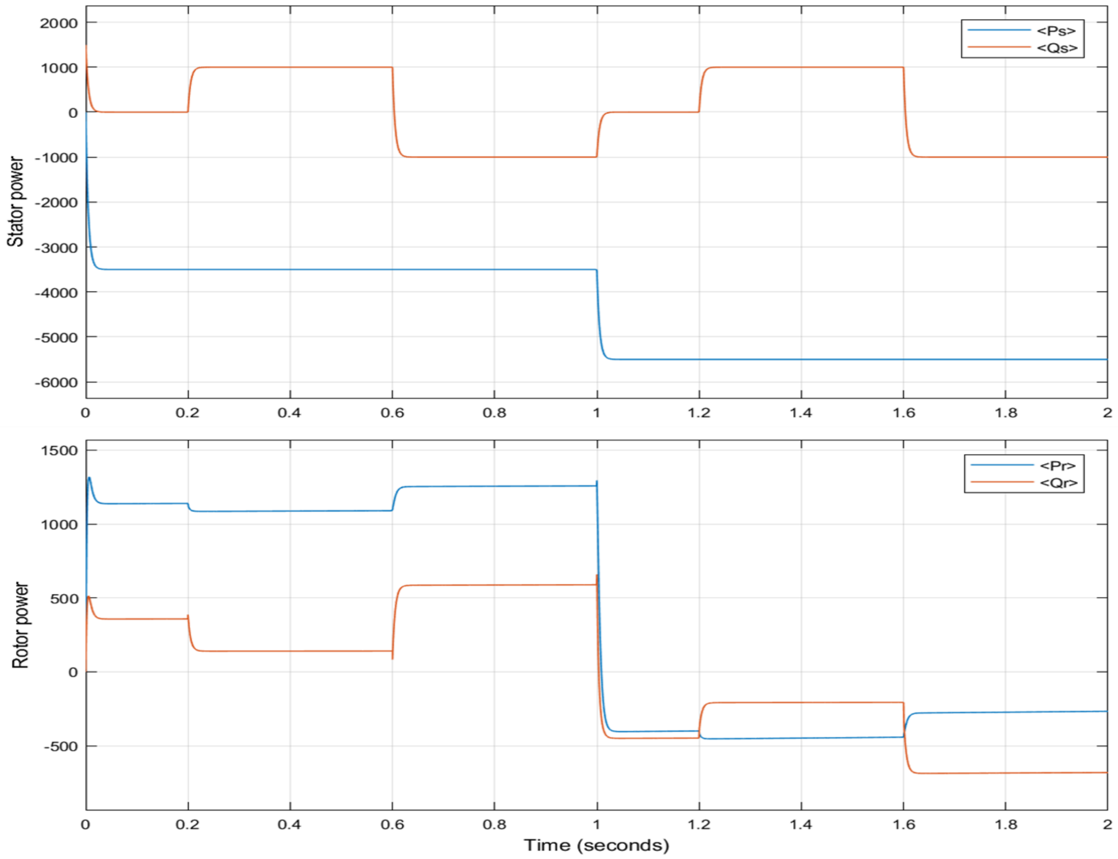

*Figure 2.11: Evolution of the stator and rotor powers.*

The variation of the stator and rotor frequencies ($f_s$ and $f_r$ respectively) are shown in first plot of Figure 2.12. While the angular frequencies ($\omega_s$ and $\omega_r$ respectively) and the mechanical speed $\omega_m$ , they have been displayed in second plot of Figure 2.12. We can notice that $f_s$ stayed constant and equal to $50Hz$ regardless of the mechanical speed value. Unlike the stator frequency $f_s$, the rotor frequency $f_r$ varies depending on the values of $\omega_m$ and $\omega_s$. If $\omega_m < \omega_s$ then $f_r$ is positive and so DFIG operates in sub-synchronous mode, otherwise, in the case of $\omega_m > \omega_s$, $f_r$ will be negative and the DFIG will run in super-synchronous mode (notice that change in sign of rotor frequency means the rotor phase order is changed too).

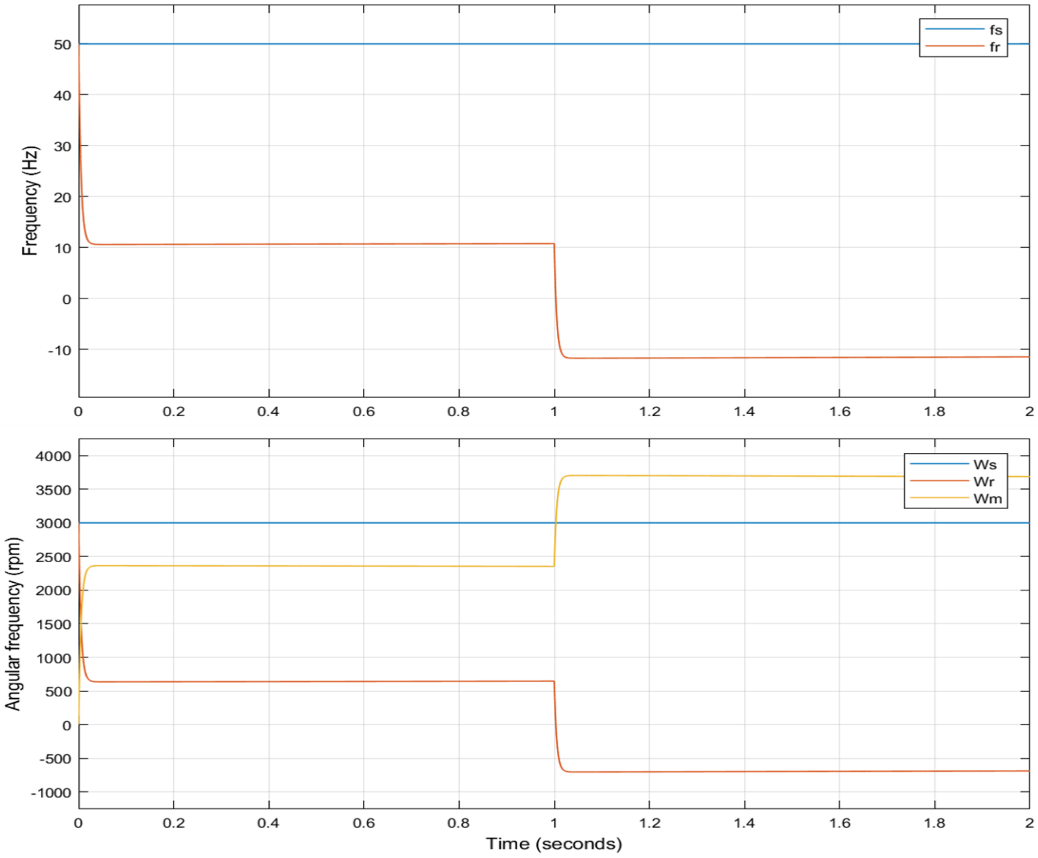

*Figure 2.12: Variation of stator frequency, rotor frequency and mechanical speed.*

Figure 2.13 displays the three-phase voltage and current signals for stator and rotor sides of the machine, while Figure 2.14 displays them in $dq$ frame.

The stator voltage is an alternating signal with constant peak value ($V_s = 311V$), while the stator current has two peaks values $I_{s\,max1} = 7.8A$ and $I_{s\,max2} = 11.9A$ (in sub-synchronous and super-synchronous modes respectively). Also it is clear that the stator frequency is constant $f_s = 50Hz$ (the period $T_s = 0.02s = 20ms$) at stator sides.

In the rotor side, there are variations in voltage and current simultaneous with the variation of the stator active and reactive power. Referring to $v_r$ and $i_r$ represented in Figure 2.13, the rotor frequency is constant $f_r = 10Hz$. But the sequence of the voltage and the current of phases is changing at $t = 1s$ (last two graphs in Figure 2.13) which is the consequence of changing rotor frequency sign from positive to negative ($10Hz$ to $-10Hz$).

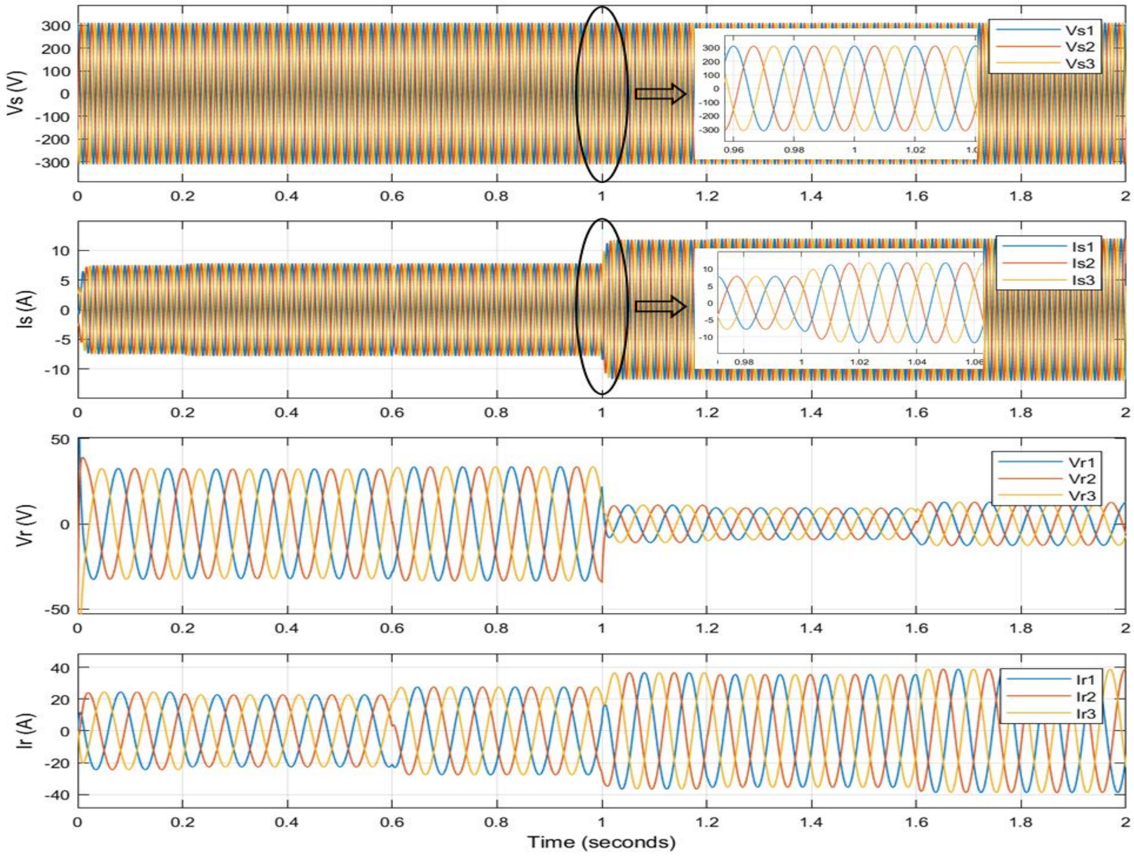

*Figure 2.13: Variation of the three-phase voltage and current on the stator and rotor sides.*

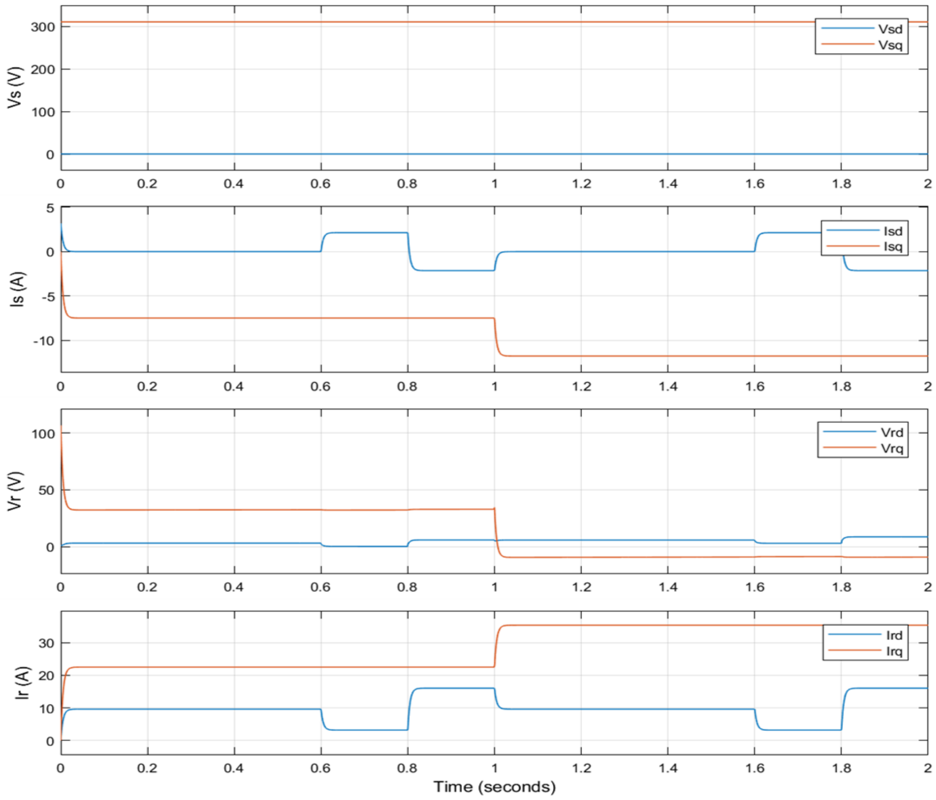

*Figure 2.14: Variation of the voltage and the current on the stator and rotor sides in dq-frame.*

First graph in Figure 2.14 proves that stator voltage is validated under SFO concept. Regarding to the rotor current, it can be noticed that the quadrature component $i_{rq}$ is inversely related to the stator active power, also the direct component $i_{rd}$ is inversely proportional to stator reactive power but with a particular offset.

## 2.5 Conclusion

This chapter has allowed us to establish the synthesis of a PI controllers for the control of the DFIM used as a generator. The first controller is for the rotor side converter, the purpose of this controller is to control the exchange of active and reactive power between the stator of the machine and the grid by modifying the amplitude and the frequency of the rotor voltages. While the second controller is for the grid side converter, it is used to stabilize the DC-bus voltage at desired value. Moreover, we have validated the controls by simulation for two operating points, one in sub-synchronous mode and the other in super-synchronous mode.

# Chapter 3: Static converter

## 3.1 Introduction

Within the context of doubly fed induction generators, the converters connected to utility grid and rotor windings are three-phase voltage source converters (VSC) which can operate as rectifier or inverter depending on the sub/super synchronous operation of the machine (since it is used as a variable speed constant frequency - VSCF - generator). In such an application, IGBTs are classically preferred due to the required voltage ratings (however, it must be noticed that SiC MOSFETs could also be good candidates with even higher performances). "Big" (and slow) components such as GTO and IGCT can be avoided in these small scale generators mainly because of the fractional rating of power converters connected to the rotor side of the DFIG since the sliding rate remains low (usually s<0.3).

The main aim of the static converter is to allow, through appropriate control method, such as Pulse Width Modulation (PWM), to transform electrical energy from one form to another while controlling its direction and characteristics with respect to desired application [13], [57]. Currently, these control algorithms of drive systems are widely required in the industrial applications [57], [58]. But, their choice must take into account the constraints generated by the operational and environmental conditions. Here, the challenge is to size the devices like capacitors at the best cost and smallest volume, while ensuring trouble-free operation under operational conditions for the desired lifetime.

As shown in the Figure 3.1, the principle of power conversion consist of an electrical energy source, power electronic circuit that transfers the energy from source to load, and a control bloc. The latter is responsible part to supervise and regulates the various parameters such as the real and reactive power, voltages and currents for each part.

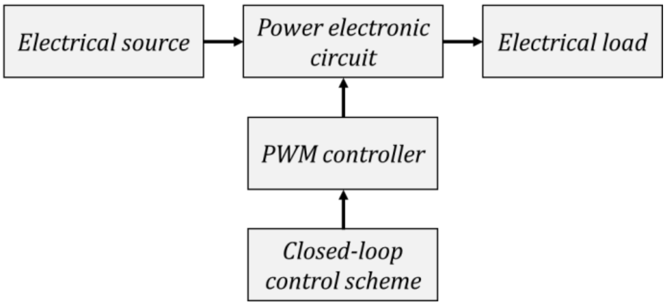

*Figure 3.1: Global diagram of a power conversion system.*

The purpose of this chapter is to focus on the static converter through displaying its structure, working principle and mathematical model. In addition, the PWM strategies will be addressed by presenting the evaluation criteria for these strategies. Also the algorithm and concept for many strategies will be evoked such as SVPWM, GDPWM and DCPWM.

## 3.2 The voltage source converter

The purpose of this section is to present the preliminary concepts on the structure and modelling of two level three-phase inverter. The various quantities will be introduced in order to have a clear vision on the parameters those will be used later.

### 3.2.1 Structure of the VSC

The two level three-phase VSC shown in Figure 3.2 takes an important class of power electronics. It is present in a wide range of applications for the speed variation of AC electrical machines (industrial drives but also for traction machines for electric vehicles [59]. Despite its apparent simplicity, this converter is highly nonlinear and difficult to accurately identify. However, a simplified model of IGBT bridge can be elaborated under the assumption of Continuous Conduction Mode (CCM), ideal switches and no losses.

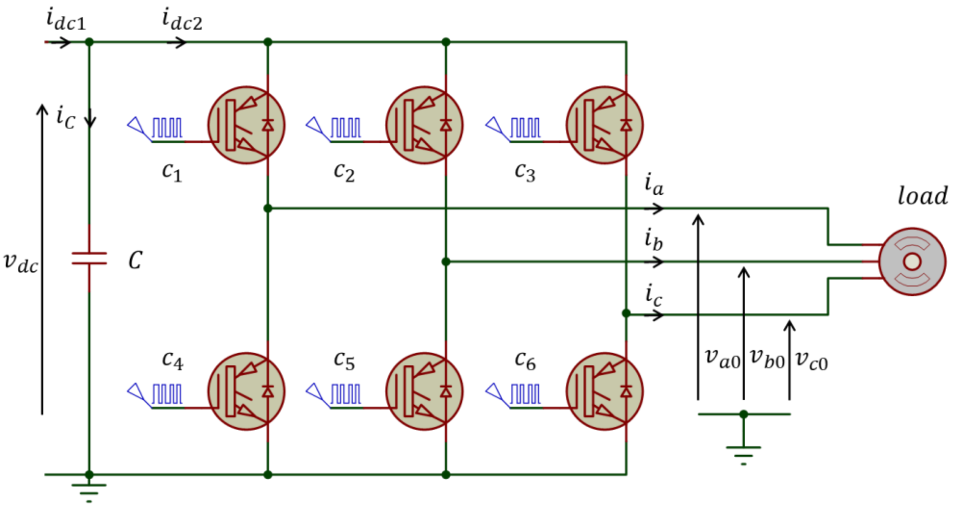

*Figure 3.2: Three-phase two level VSC circuit.*

It is composed of three bridge legs. Each leg has two switching components. According to the application requirements, those componnets might be MOSFET, JFET, IGBT or others. The switches can be turned on or off by controlling the gate of the components. The diode connected in parallel provides the current throughways in the reverse direction because the semiconductor switches conduct only in one direction. The capacitor or the DC-link is used for the decouling between the energy source and the inverter.

In the same bridge leg of the VSC, the commands for the bottom and the top switches are opposite, i.e. when the switch at the top is turned on then the bottom switch is turned off and vice versa. While the ideal signal can't be obtained in the real case because of transition time present when changing the state, therefore a dead time $t_d$ must be inserted to gate signals of switching devices before turning on the state of the switch. This time protects the circuit against short-circuit in the same leg of the VSC. Both switching devices $c_i$ and $c_{i+3}$ in the same leg are turned off during the dead time period $t_d$. This latter causes a miss control of the switches and the current can flows only through anti-parallel diode $D_i$ and $D_{i+3}$ [57]. That dead time lead to a distortion produced at the output signals. For this reason, $t_d$ should be as small as possible to reduce the distortion. Figure 3.3-a represents the switching patterns of ($c_i$, $c_{i+3}$) that compares the real and the ideal cases, while Figure 3.3-b shows the four possible status of an inverter phase leg, noting that the third status appears because of the insertion of dead time, and in this case the current goes through the diodes. The last case is critical and it mustn't be happened, otherwise, it will produce a short circuit on the source.

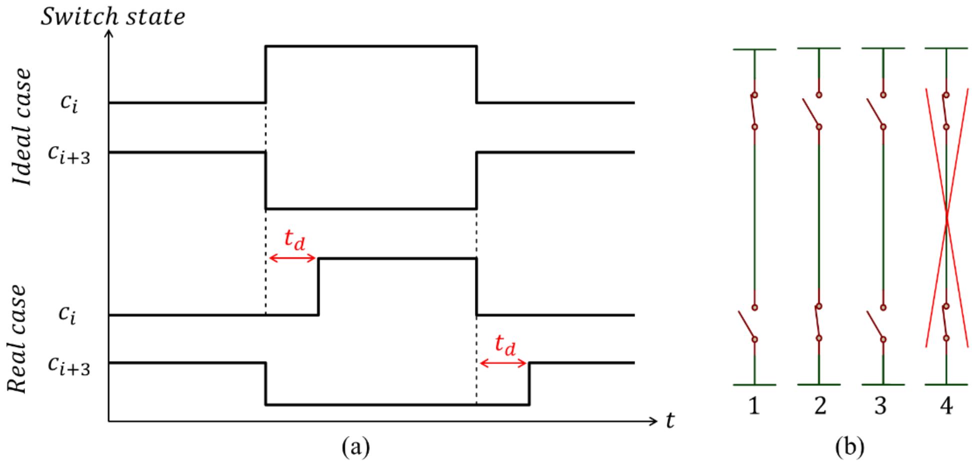

*Figure 3.3: (a)  High and low switches' patterns for the real and ideal cases. (b) The possible status of each leg.*

The used decoupling frequency $f_{PWM}$ is in range of $10\ kHz$ so the decoupling time is varying within a range of few fraction of milliseconds. Consequently, the dead time can be assumed to be zero with comparing to the decoupling time because of its value in range of a few microseconds.

In the next, a generic model of the three-phase VSC that has three bridge legs is presented in Figure 3.4. Each bridge leg (noted $i$ with $i = 1\ldots3$) has two switches, which are bidirectional in current and unidirectional in voltage: upper switch $c_i$, and lower switch $c_{i+3}$. The switches of the inverter are transistors of type IGBT (because we are going to work on high voltage application) associated with anti-parallel diodes. It's important to mention that a simplified model of VSC is elaborated under the following assumptions:

- The switching of the transistors is instantaneous.
- The voltage drop across the switches is insignificant.
- The three-phase load is balanced, star-connected with an isolated neutral.

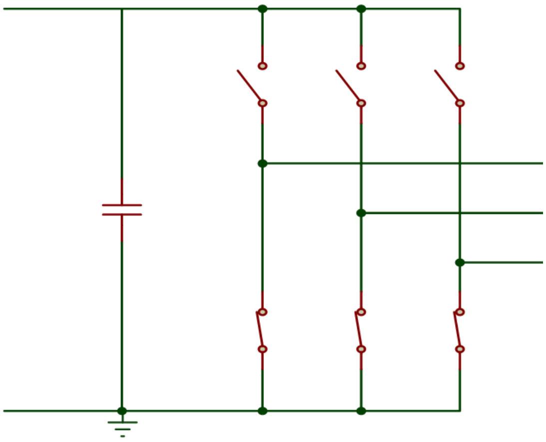

*Figure 3.4: A generic model for the three-phase VSI.*

In order to avoid the short circuit happening on the voltage source, the two transistors of same leg never to be controlled at the same time. So, the authorized configurations are the following:

- $c_i$ is turned on and $c_{i+3}$ is turned off.
- $c_i$ is turned off and $c_{i+3}$ is turned on.

So we can deduce that $c_i = \overline{c_{i+3}}$ and then only one binary variable is required to describe the state of a bridge arm (neglecting the inter-channel delay 2). In an arbitrary way, this one is defined as follows:

$$c_i = \begin{cases} 1 & if\ c_i\ is\ closed\ and\ c_{i+3}\ is\ opended \\ 0 & if\ c_i\ is\ opended\ and\ c_{i+3}\ is\ closed \end{cases} \tag{3.1}$$

## 3.2.2 Analysis and modelling of the system

### 3.2.2.1 Inverter

With the two possible states of each bridge arm, the voltages $v_{a0}$, $v_{b0}$ and $v_{c0}$ take two values $v_{dc}$ or 0 (see 3.2.1), the simple voltages with respect to ground at the output of the inverter ($v_{a0}$, $v_{b0}$ and $v_{c0}$) have the expression:

$$\begin{pmatrix} v_{a0} \\ v_{b0} \\ v_{c0} \end{pmatrix} = v_{dc} \times \begin{pmatrix} c_a \\ c_b \\ c_c \end{pmatrix} \tag{3.2}$$

With $C_3 = (c_a, c_b, c_c)^T = (c_1, c_2, c_3)^T$ is the switches state or the command vector coming from Pulse Width Modulation (PWM) strategy block which will be treated later. Noting that vector or matrix followed by a superscript of the letter " $T$ ", it means the transpose operation is applied to this vector or matrix.

With referring to Figure 3.5, the single-phase voltage $v_{xN}$ of phase $x$ can be done by (3.3).

$$v_{xN} = v_{x0} - v_{N0} \tag{3.3}$$

$v_{N0}$ is the neutral voltage, by applying Millman’s theorem to the point $N$ for the circuit in Figure 3.5 [60], with the assumption that the three-phase machine is balanced, we have :

$$v_{N0} = \frac{v_{a0} + v_{b0} + v_{c0}}{3} \tag{3.4}$$

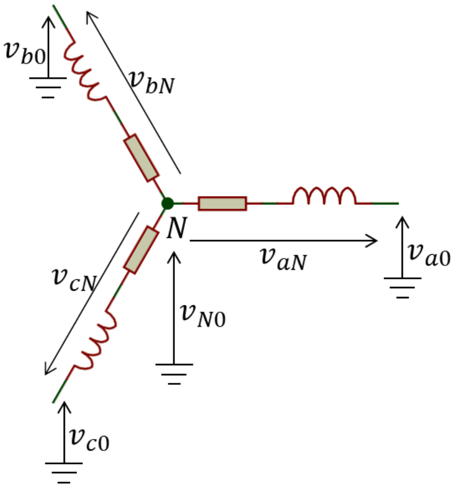

*Figure 3.5:phase voltage with respect to the ground and to the neutral point.*

Substituting Equations (3.2) and (3.4) into equation (3.3) for phase $a$, we have:

$$v_{aN} = v_{a0} - v_{N0} = v_{dc}c_a - \frac{v_{a0} + v_{b0} + v_{c0}}{3}$$

$$v_{aN} = v_{dc}c_a - v_{dc}\frac{c_a + c_b + c_c}{3}$$

$$v_{aN} = \frac{v_{dc}}{3} \times (2 \times c_a - c_b - c_c) \tag{3.5}$$

By applying the same calculations for the other two phases $b$ and $c$, the simple voltages at the terminals of the machine have the expression :

$$\begin{pmatrix} v_a \\ v_b \\ v_c \end{pmatrix} = \begin{pmatrix} v_{aN} \\ v_{bN} \\ v_{cN} \end{pmatrix} = \frac{v_{dc}}{3}\begin{pmatrix} 2 & -1 & -1 \\ -1 & 2 & -1 \\ -1 & -1 & 2 \end{pmatrix}\begin{pmatrix} c_a \\ c_b \\ c_c \end{pmatrix} \tag{3.6}$$

So the function of the three-phase load voltage $V_3 = (v_{aN}, v_{bN}, v_{cN})^T$ depends on the DC-link voltage value $v_{dc}$ and the switches state $C_3$ multiplied by a coefficient matrix $G$ as mentioned in (3.7).

$$V_3 = v_{dc}.G.C_3 \tag{3.7}$$

Where $G = \frac{1}{3}\begin{bmatrix} 2 & -1 & -1 \\ -1 & 2 & -1 \\ -1 & -1 & 2 \end{bmatrix}$.

The value for three phase load current $I_3 = (i_a, i_b, i_c)^T$ in relation with $V_3$ can be obtained as expressed in (3.8).

$$I_3 = \begin{bmatrix} i_a \\ i_b \\ i_c \end{bmatrix} = \frac{1}{R + L.s}\begin{bmatrix} v_a \\ v_b \\ v_c \end{bmatrix} = \frac{1}{R + L.s} V_3 \tag{3.8}$$

Basing on Figure 3.4, the DC-link current $i_{dc2}$ is divided into three current $i_a, i_b$ and $i_c$ depending on the state of switches $c_a, c_b$ and $c_c$ as mentioned in (3.9).

$$i_{dc2} = C_3.I_3 = c_a i_a + c_b i_b + c_c i_c \tag{3.9}$$

#### 3.2.2.2 DC bus

Modelling of DC bus requires study of the circuit shown in Figure 3.6. This circuit consists of decoupling capacitor $C$ which having $v_{dc}$ as voltage on its terminals. The current coming from the first side is represented by $i_{dc1}$, it is divided into capacitor current $i_{cap}$ and the current $i_{dc2}$ that comes out of the DC bus. Finally, the voltage $v_{dc}$ on the capacitor is applied on the inverter input.

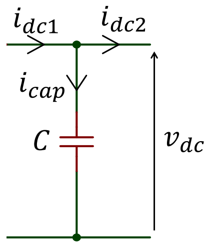

*Figure 3.6: DC bus circuit.*

Based on Figure 3.6, the equations (3.10) and (3.11) have been obtained.

$$i_{cap} = i_{dc1} - i_{dc2} \tag{3.10}$$

$$v_{dc} = \frac{1}{C.s} i_{cap} \qquad (3.11)$$

It is relevant to point out that the input current $i_{dc1}$can be either constant or variable depending on the application. For instance in [13], [59], it has been constant because the current ($i_{dc1}$) comes out of the battery bank. While in  [61], [62], $i_{dc1}$ represents the output current of the controlled converter (and more precisely a rectifier). Consequently, in such case, $i_{dc1}$ is controlled and can be variable depending on the application requirements.

## 3.3 PWM strategies

This section is dedicated to present the popular PWM strategies those are used to generate injected signals on the switches gates. Actually there are many strategies which can be classified into two groups. The first group are continuous PWM (CPWM) while the second are discontinuous PWM (DPWM).

Under these groups' umbrella, many strategies can be found such as Sinusoidal PWM (SPWM), Space Vector PWM (SVPWM), Third Harmonic Injection PWM (THIPWM), double Carrier PWM (DCPWM), Unified Double Career PWM (Uni-DCPWM), DPWM3, DPWMMAX, DPWMMIN and generalized discontinuous PWM (GDPWM) [59], [63]–[65]. Also [66]–[69] dealt Active Zero State PWM (AZSPWM), Near State PWM (NSPWM) and Remote State PWM (RSPWM).

Some of PWM strategies are shown in Table 3.1 and they are classified according to whether they are continuous or discontinuous.

| **Continuous (CPWM)** | **Discontinuous PWM (DPWM)** |
|---|---|
| Sinusoidal Pulse Width Modulation (SPWM) | DPWM3, DPWMMAX, DPWMMIN |
| Space Vector Pulse Width Modulation (SVPWM) | Generalized Discontinuous PWM (GDPWM) |
| Third Harmonic Injection Pulse Width Modulation (THIPWM) | Double Carrier Pulse Width Modulation (x-DCPWM) |

*Table 3.1: Most common PWM strategies.*

### 3.3.1 Common parameters of PWM strategies

Before starting with the various types of PWM strategies, it's important to mention essential and common parameters for all types of control strategies.

- Modulation index is defined as the ratio of the fundamental component amplitude of the line-to-neutral inverter output voltage to one-half of the available DC bus voltage [70] as expressed in (3.12). $V_{max}$ is the maximum amplitude of the sinewave and $v_{dc}$ is the DC-bus voltage which is equal to the carrier peak value (here the carrier is not normalized yet).

$$m = \frac{V_{max}}{\frac{v_{dc}}{2}} \tag{3.12}$$

- Duty cycle $D = \frac{T_{on}}{T_{PWM}}$ of converter. $T_{on}$ is the total ON period of the switch and $T_{PWM}$ is the switching time (or the carrier period) [71]. Always $0 < D < 1$.
- Frequency ratio $N = \frac{f_{PWM}}{f_s} = \frac{T_s}{T_{PWM}} > 1$ or number of switching cycles per sinewave period. $f_{PWM} = \frac{1}{T_{PWM}}$ is carrier frequency while $f_s = \frac{1}{T_s}$ defines the sinewave frequency. This ratio should be high (i.e. $f_{PWM}$ should be high) in order to minimize the Total Harmonic Distortion (THD) [72].

Figure 3.7 illustrates various parameters for $N = 4$ and $m = 0.8$.

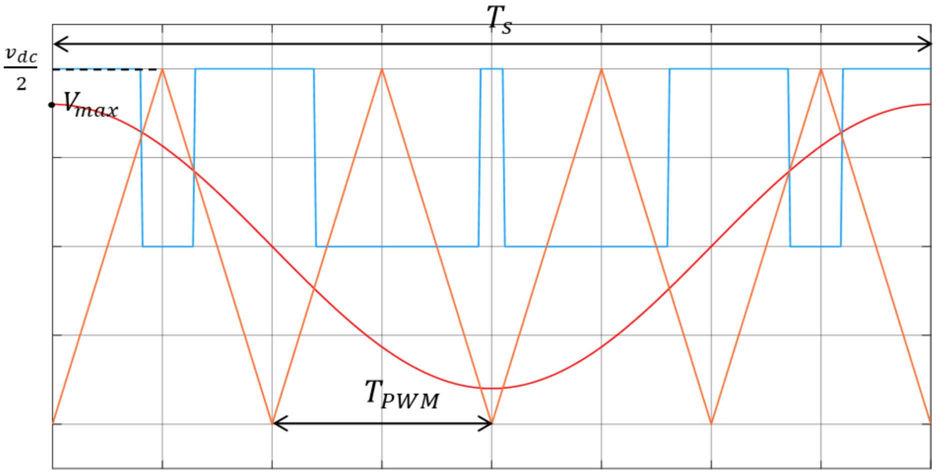

*Figure 3.7: PWM waveforms for N=4 and m =0.8.*

### 3.3.2 Evaluation criteria of the PWM strategies

PWM is the most commonly used strategy to control the output voltage of the inverter [73]. Because there are many types of PWM strategies, it should know the evaluation criteria which used to give the importance for one strategy over others. Furthermore, it will help us take a good decision to choose a specific strategy because of its advantages, or to avoid another strategy because of its disadvantages regarding to the application requirements. Regarding to [74]–[76], the selection of a strategy is often based on optimizing some criteria such as:

- Wide linear modulation zone: the extension of the linearity range of the inverter, to extend the optimal operating range of the electric machine.
- Reduction of switching losses: this mainly implies a reduction in the size of the radiator attached to the inverter, thus reducing the cost of the drive and increase the life time of the inverter.
- Acoustic noise reduction, which is very important for the expansion of the use of electric drives in noise sensitive environments.
- Less total harmonic distortion (THD) in the output spectrum.
- Easy implementation and less computation time.

Figure 3.8 categories some of PWM strategies under three optimisation umbrellas: extension of linearity, minimization of the losses and reduction of the noise [76]–[79].

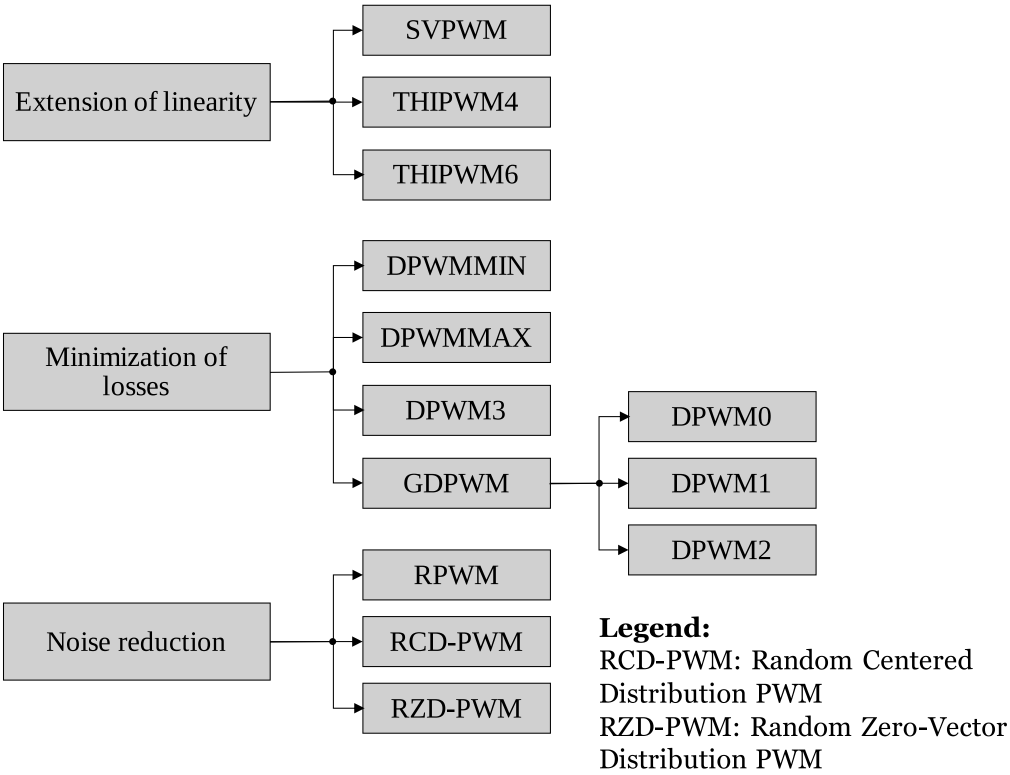

**Legend:**
RCD-PWM: Random Centered Distribution PWM
RZD-PWM: Random Zero-Vector Distribution PWM

*Figure 3.8: Classification of PWM methods.*

According to [13] and [59], these evaluation criteria are distributed on the output, input and inside of the inverter like the next:

#### 3.3.2.1 The output evaluation criteria

In order to compare and to evaluate the quality of the inverter output voltage (which one of the output criteria) for the different PWM strategies, the total harmonic distortion (THD) is used. If the THD is big, then the PWM strategy that used, it produced harmonics with high amplitude. In addition to the output voltage quality, the ripple current of the load and its harmonic content can be used as output criteria in order to compare the efficiency between the PWM strategies.

#### 3.3.2.2 The input evaluation criteria

The sizing of a capacitor is based on two important criteria: its lifetime and the ripple of the maximum voltage applied to its terminals. Regarding the lifetime of the decoupling capacitor, noted $l_c$, it is determined by the level of the voltage applied to the capacitor terminals and the internal temperature of the latter as shown in the (3.13) [80].

$$l_c = l_0 \left(\frac{V_0}{V}\right)^n .2^{\frac{T_0 - T}{10}} \tag{3.13}$$

$l_0$: The life time duration for $T_0$.
$T_0$: The ambient temperature.
$T$: The intern temperature of the capacitor.
$V$: The applied voltage on the capacitor.
$n = [7 \ldots 9.4]$ for film capacitors.

One can conclude by (3.13) that capacitor life time increase while the intern temperature decrease. This later, it happens when the RMS current value in the capacitor decrease. Like the output side, the harmonic content of the current in the decoupling capacitor and the ripple of the DC bus voltage, they are also used as evaluation criteria at the input side.

#### 3.3.2.3 The inside evaluation criteria

The losses in the inverter can be classified into two categories: conductive losses and switching losses. The conduction losses are due to the switch resistance in the conduction state. These losses are given by:

$$p_{cond} = \frac{3}{2} . R_S . I^2 \tag{3.14}$$

Where $p_{cond}$ $R_S$ and $I$ are respectively the power conduction losses, switch resistance and the peak value of the load current.

Concerning the switching losses, it influenced by the effective number of switches per second which can be reduced by using some strategies. The switching losses are caused by the coexistence of the voltage and the current at the moment of commutation. The switching losses inside a three-phase inverter can be evaluated with the following formula [63]:

$$P_{sw} = \frac{1}{2}.f_{PWM}.v_{dc}(t_{ON} + t_{OFF})(|i_a(t)| + |i_b(t)| + |i_c(t)|) \qquad (3.15)$$

With $P_{sw}$ being the power switching losses per fundamental cycle, $f_{PWM}$ is the frequency of the used PWM strategy, $v_{dc}$ is the DC link voltage, $t_{ON} + t_{OFF}$ being the sum of the turn-on time and turn-off time of the switching devices and $(|i_a(t)| + |i_b(t)| + |i_c(t)|)$ being the sum of the switched current inside each half-bridge.

### 3.3.3 Scalar-based approach for PWM

Generally, for PWM methods, there are two main implementation techniques, the scalar implementation and the space vector implementation. The scalar approach was one of the most used strategies before starting the development that has been seen in dedicated digital systems domain. The operating principle of the SPWM with triangular carrier is presented in Figure 3.9, for each inverter phase, a reference modulating sine wave is compared with a triangular carrier wave $c(t)$ and the intersections (red and green dashed lines) define the switching instants for the associated inverter leg switches [81], [82].

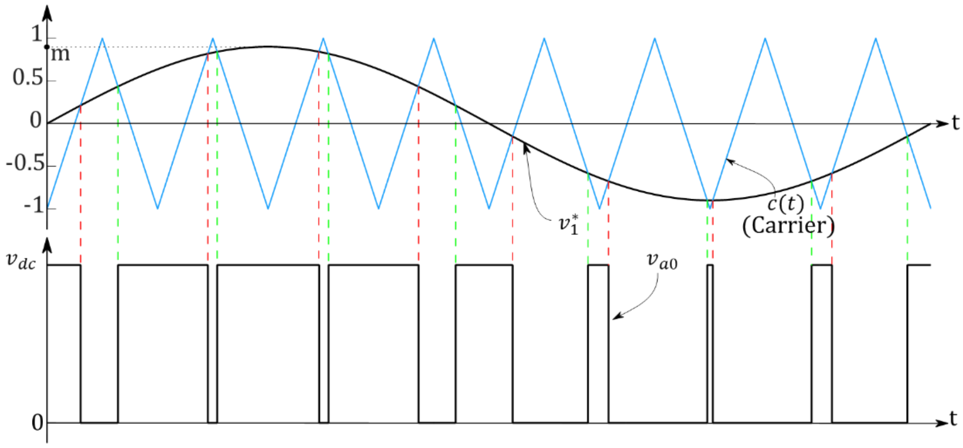

*Figure 3.9: SPWM or scalar approach for PWM.*

Figure 3.9 shows an example where the reference signal is a pure sinusoid of frequency $f_s$ and the carrier is a "symmetrical triangle" with high frequency $f_{PWM}$. In this case, we suppose that the average value of the control signal over one carrier period is constant and equal to the reference signal value thanks to the assumption $f_{PWM} \gg f_s$ (i.e. we have a very small variation of the reference signal during the decoupling period). Obviously, the switching causes voltage harmonics which appear at the inverter output around the carrier frequency and its multiples. Thankfully, with the filtering characteristic of electrical machines ($RL$ model), only the fundamental component of the load currents can develop (on the condition that the frequency ratio $N = \frac{f_{PWM}}{f_s} > 20 \gg 1$) [59].

If the modulating signal (also called reference signal) is a pure sinusoid, then this strategy is called SPWM. Consequently, the normalized reference signal (for phase "a") is defined as follows:

$$v_1^* = m \cdot \cos(\omega t) \tag{3.16}$$

Recalling that $m = \frac{V_{max}}{\frac{v_{dc}}{2}}$ is the modulation index (see 3.3.1) where $\omega$ is the angular frequency of the sinewave.

Figure 3.10 shows how PWM technique generates the signals $c_a$, $c_b$ and $c_c$. These are the signals that control the inverter' transistors. Their values are "1" (if the switch turned on) or "0" (if the switch turned off) depending by the comparing result between the amplitudes of the carrier $c(t)$ (saw-tooth signal $c(t) \in [-1,1]$) and the normalized reference sine waves voltages ($v_1^*$, $v_2^*$ and $v_3^*$).

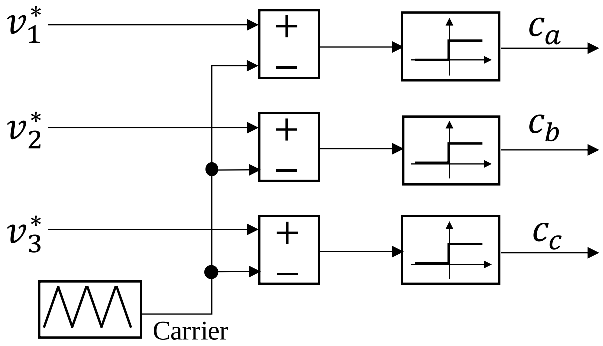

*Figure 3.10: Block diagram of the basic scalar SPWM method.*

So the PWM concept is based on the comparison of the normalized reference signals $v_1^*(t)$ with the carrier $c(t)$ aimed at determining the pulse instants of the transistor according to the following cases (for phase "a"):

- $v_1^*(t) \geq c(t)$ ➔ the switch or transistor is turned ON.
- $v_1^*(t) < c(t)$ ➔ the switch or transistor is turned OFF.

This comparison should be done also between $v_2^*(t)$ (respectively $v_3^*(t)$) and $c(t)$ for phase "b" (respectively for phase "c").

In a three-phase inverter, the scalar PWM technique with a single carrier is used to generate the driving signals of the three bridge arms. Defining $v_1^*$, $v_2^*$ and $v_3^*$ as the normalized reference sinusoid of the three bridge arms, then the normalized reference function can be written as:

$$\begin{cases} v_1^* = \frac{v_a^*}{\frac{v_{dc}}{2}} = m \cdot \cos(\theta) \\ v_2^* = \frac{v_b^*}{\frac{v_{dc}}{2}} = m \cdot \cos\left(\theta - \frac{2\pi}{3}\right) \\ v_3^* = \frac{v_c^*}{\frac{v_{dc}}{2}} = m \cdot \cos\left(\theta + \frac{2\pi}{3}\right) \end{cases} \tag{3.17}$$

Whereas the normalized modulating signal $mod_x$ are defined as the sum of the normalized reference sinusoids with the zero-sequence voltage $v_{n0}$, thus :

$$\begin{cases} mod_1 = m \cdot \cos(\theta) + v_{n0} \\ mod_2 = m \cdot \cos\left(\theta - \frac{2\pi}{3}\right) + v_{n0} \\ mod_3 = m \cdot \cos\left(\theta + \frac{2\pi}{3}\right) + v_{n0} \end{cases} \tag{3.18}$$

In the conventional scalar PWM method any zero-sequence signal can be injected to the reference modulation waves (see Figure 3.11). It can be freely varied, this degree of freedom can improve the waveform quality and reduce the switching losses significantly [64].

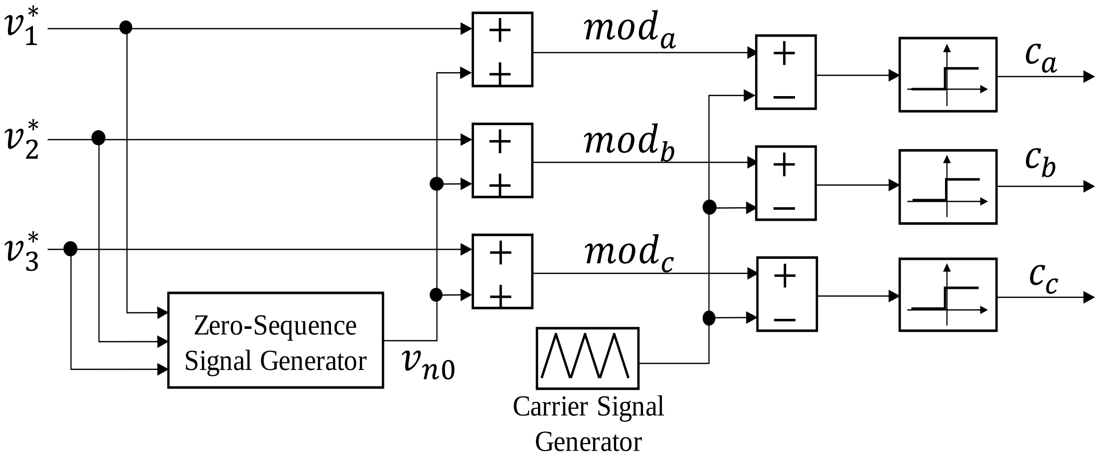

*Figure 3.11: Block diagram of the conventional scalar PWM method employing zero-sequence signal injection and a common triangular carrier wave.*

Adding of the same zero sequence component $v_{n0}$ to the three sinusoids leads to obtain the average voltages normalized with respect to $v_{dc}$ at the outputs of the inverter as shown in the following expression:

$$\begin{cases} v_{10} = m \cdot \cos(\theta) + v_{n0} \\ v_{20} = m \cdot \cos\left(\theta - \frac{2\pi}{3}\right) + v_{n0} \\ v_{30} = m \cdot \cos\left(\theta + \frac{2\pi}{3}\right) + v_{n0} \end{cases} \tag{3.19}$$

By using equation (3.4), the normalized voltage with respect to $v_{dc}$ of the neutral point (referred to the negative terminal of the battery) is:

$$v_{N0} = \frac{v_{10} + v_{20} + v_{30}}{3} = v_{n0} \tag{3.20}$$

The normalized phase's voltages (referred to the neutral point of the star load) of the load can be written as mentioned in (3.21):

$$\begin{cases} v_{1N} = v_{10} - v_{N0} = m \cdot \cos(\theta) \\ v_{2N} = v_{20} - v_{N0} = m \cdot \cos\left(\theta - \frac{2\pi}{3}\right) \\ v_{3N} = v_{30} - v_{N0} = m \cdot \cos\left(\theta + \frac{2\pi}{3}\right) \end{cases} \tag{3.21}$$

In other words, the addition of a zero-sequence component has no influence on the load voltage where it varies independently of $v_{n0}$.

Thanks to this property, several PWM strategies have been proposed in the literature in order to improve the inverter operation with respect to different criteria defined by the users.

It should be noted that the carrier can take several forms. Among them, the most common are: symmetrical carrier, saw tooth carrier or random slope carrier with fixed frequency or not (see Figure 3.12). Here, the symmetrical carrier is chosen to illustrate the generation of the bridge arm driving signals.

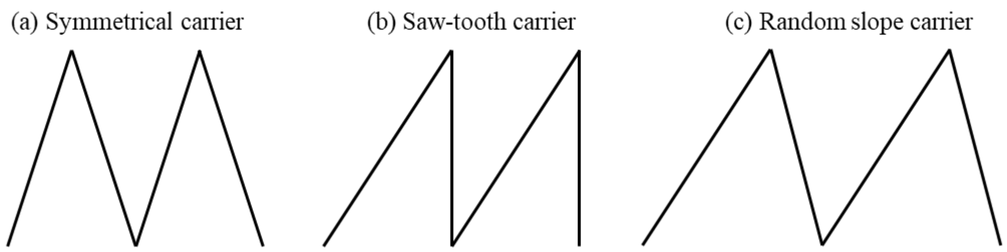

*Figure 3.12: Carrier types.*

Below we will discuss the vector-based approach for PWM or the SVPWM after the scalar-based method has been treated.

### 3.3.4 Vector-based approach for PWM

The SVPWM approach is a general method based on the direct use of a vector diagram. Contrary to the previous approach which generates the signals for each bridge arm independently, this approach considers the whole states of the output voltage of the three bridge arms as a single vector in the plane thanks to the three-phase to two-phase transformation based on the Clarke (or Concordia) matrix (see Appendix A). Consequently, it positions the reference voltages obtained after regulation directly on the $\alpha\beta$ reference frame by using Clarke (or Concordia) transformation, then the control signals are developed by taking into account the OFF/ON state of the three inverter arms $(a, b, c)$ at the same time (inverter state vector control). The appropriate control commands are applied to the switches. Indeed, these calculations must be repeated for each switching period so higher switching frequencies require faster calculations. The objective of this approach is to generate voltages $v_a, v_b$ and $v_c$ (measured value) as close as possible to a fixed references $v_a^*, v_b^*$ and $v_c^*$ [75], [83].

Since the three-phase system is balanced, therefore, $v_a + v_b + v_c = 0$ and the arm voltages are shifted by $\frac{2\pi}{3}$ with each other. The expression for the $\alpha$ and $\beta$ components of the arm voltages is written [75] ($\overrightarrow{v_{\alpha\beta}^*}$ is illustrated in Figure 3.13):

$$\begin{cases} v_\alpha = \frac{2}{3}\left(v_a - \frac{1}{2}v_b - \frac{1}{2}v_c\right) \\ v_\beta = \frac{2}{3}\left(\frac{\sqrt{3}}{2}v_b - \frac{\sqrt{3}}{2}v_c\right) \end{cases} \tag{3.22}$$

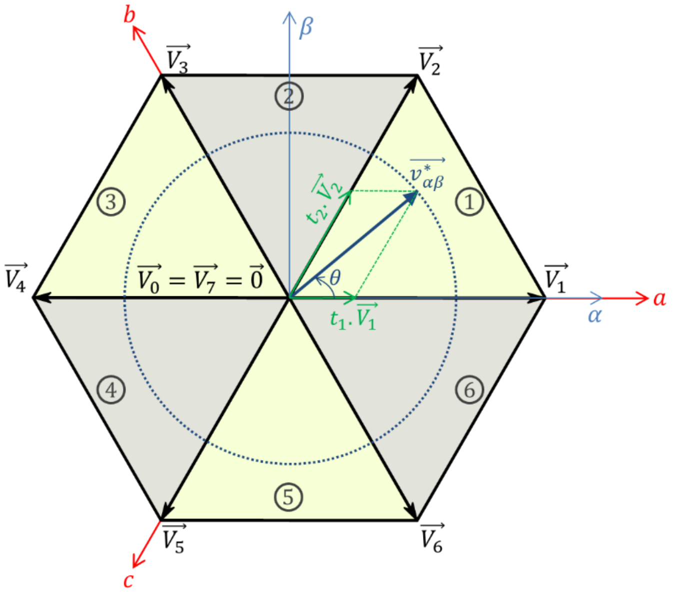

*Figure 3.13:Representation in the αβ coordinates of the inverter voltage vectors and the reference voltage in the first sector.*

This equation allows us to model a three-phase system by an equivalent two-phase model according to the formula:

$$\begin{pmatrix} v_\alpha \\ v_\beta \end{pmatrix} = C_{23} \times \begin{pmatrix} v_a \\ v_b \\ v_c \end{pmatrix} \tag{3.23}$$

Where $C_{23} = \frac{2}{3}\begin{bmatrix} 1 & -\frac{1}{2} & -\frac{1}{2} \\ 0 & \frac{\sqrt{3}}{2} & -\frac{\sqrt{3}}{2} \end{bmatrix}$.

If we have a balanced three-phase reference voltages shifted by $\frac{2\pi}{3}$ :

$$\begin{cases} v_a^* = V_{max} \cos\theta \\ v_b^* = V_{max} \cos\left(\theta - \frac{2\pi}{3}\right) \\ v_c^* = V_{max} \cos\left(\theta + \frac{2\pi}{3}\right) \end{cases} \tag{3.24}$$

The Clarke transformation of the vector $\begin{pmatrix} v_a^* \\ v_b^* \\ v_c^* \end{pmatrix}$ to the $\alpha\beta$ plane is :

$$\overrightarrow{v_{\alpha\beta}^*} = \begin{pmatrix} v_\alpha^* \\ v_\beta^* \end{pmatrix} = C_{23} \cdot \begin{pmatrix} v_a^* \\ v_b^* \\ v_c^* \end{pmatrix} = V_{max} \begin{pmatrix} \cos\theta \\ \sin\theta \end{pmatrix} \tag{3.25}$$

The equation (3.25) lead us to conclude that the trajectory of the Clarke transformation of the vector $(v_a^*, v_b^*, v_c^*)^T$ describes a circle in $\alpha\beta$ plane, with radius $V_{max}$ (see Figure 3.13). In sinusoidal steady state, we have $\theta = \omega t + \theta_0$ where $\omega$ is the pulsation of the three voltages $v_a^*, v_b^*$ and $v_c^*$ which corresponds in vector representation to the angular velocity of the equivalent rotating vector $\overrightarrow{v_{\alpha\beta}^*}$ in Clarke frame $(\alpha\beta)$. A complete rotation of $\overrightarrow{v_{\alpha\beta}^*}$ (from $0$ to $2\pi$) corresponds to a fundamental period of the voltages.

Applying the Clarke transformation to the simple voltages of the load at the output of the inverter, we obtain:

$$\overrightarrow{v_k} = C_{23} \cdot \begin{pmatrix} v_{aN} \\ v_{bN} \\ v_{cN} \end{pmatrix} \tag{3.26}$$

$$\overrightarrow{v_k} = C_{23} \cdot \begin{pmatrix} v_{a0} - v_{N0} \\ v_{b0} - v_{N0} \\ v_{c0} - v_{N0} \end{pmatrix}$$

$$\overrightarrow{v_k} = C_{23} \cdot \begin{pmatrix} v_{a0} \\ v_{b0} \\ v_{c0} \end{pmatrix} - v_{N0}\, \underbrace{C_{23} \cdot \begin{pmatrix} 1 \\ 1 \\ 1 \end{pmatrix}}_{\begin{pmatrix} 0 \\ 0 \end{pmatrix}}$$

$$\overrightarrow{v_k} = C_{23} \cdot \begin{pmatrix} v_{a0} \\ v_{b0} \\ v_{c0} \end{pmatrix} \tag{3.27}$$

$\overrightarrow{v_k}$ can be done as function of the DC-link voltage $v_{dc}$ and the switches state of the converter $C_3 = (c_a, c_b, c_c)^T$ by replacing $(v_{a0}, v_{b0}, v_{c0})^T$ in (3.27) by its function that obtained in (3.2).

$$\overrightarrow{v_k} = C_{23} \cdot v_{dc} \cdot \begin{pmatrix} c_a \\ c_b \\ c_c \end{pmatrix} \tag{3.28}$$

As previously mentioned, each control command $c_i$ can take 2 values 0 or 1 (turned OFF or turned ON), so the control vector $C_3 = (c_a, c_b, c_c)^T$ takes eight possible values (it has $2^3 = 8$ possible switching modes).

Let us suppose that $\overrightarrow{V_k}$ is the normalized vector of the vector $\overrightarrow{v_k}$ with respect to $\frac{v_{dc}}{2}$, so:

$$\overrightarrow{V_k} = \frac{\overrightarrow{v_k}}{\frac{v_{dc}}{2}} = 2 \cdot C_{23} \cdot \begin{pmatrix} c_a \\ c_b \\ c_c \end{pmatrix} \tag{3.29}$$

In the $\alpha\beta$ plane, Therefore, there are eight discrete vectors of output voltage of the inverter $\overrightarrow{V_k}$, two of them ($V_0$ and $V_7$) are zero and located at the origin of the axis, while the other vectors $\overrightarrow{V_k}$ ($k \in [1 \dots 6]$) are called active vectors. The active vectors divide the plane into six different sectors (denoted 1 to 6). The representation on the $\alpha\beta$ coordinates of these vectors is shown in Figure 3.13.

In general, we will associate any vector $\vec{X} = \left(x_\alpha, x_\beta\right)^T$ in the $\alpha\beta$ plane with a complex number $\bar{X} = x_\alpha + jx_\beta$ . Thus, in complex form, we have:

$$\overline{V_k} = \begin{cases} \frac{4}{3} \cdot e^{j\frac{(k-1)\pi}{3}} & if\ k \in \{1 \dots 6\} \\ 0 & if\ k \in \{0,7\} \end{cases} \tag{3.30}$$

The correspondence of the states of the 3 bridge arms with the vectors is reported in Table 3.2.

Based on (3.26) and (3.27), it is useful to note that if the Clarke transformation is applied to the load voltages referenced to the neutral $N$ ($V_{aN}, V_{bN}$ and $V_{cN}$), the vector obtained in the reference frame is the same as that obtained when the transformation is applied to the voltages referenced to ground ($V_{a0}, V_{b0}$ and $V_{c0}$). This finding in the vector approach is perfectly consistent with that established in the conventional scalar PWM approach. This, once again, confirms that the zero-sequence component $v_{N0}$ has no influence on the phase voltages seen by the load.

To illustrate the principle of PWM with the vector approach, we take the case where the reference vector $\overrightarrow{V_{\alpha\beta}^{*}}$ is located in the first sector as illustrated in Figure 3.14.

| $\overrightarrow{V_k}$ | $c_a$ | $c_b$ | $c_c$ |
|---|---|---|---|
| $\overrightarrow{V_0} = (0,0)$ | 0 | 0 | 0 |
| $\overrightarrow{V_1} = \left(\frac{2}{3}, 0\right)$ | 1 | 0 | 0 |
| $\overrightarrow{V_2} = \left(\frac{1}{3}, \frac{1}{\sqrt{3}}\right)$ | 1 | 1 | 0 |
| $\overrightarrow{V_3} = \left(-\frac{1}{3}, \frac{1}{\sqrt{3}}\right)$ | 0 | 1 | 0 |
| $\overrightarrow{V_4} = \left(-\frac{2}{3}, 0\right)$ | 0 | 1 | 1 |
| $\overrightarrow{V_5} = \left(-\frac{1}{3}, -\frac{1}{\sqrt{3}}\right)$ | 0 | 0 | 1 |
| $\overrightarrow{V_6} = \left(\frac{1}{3}, -\frac{1}{\sqrt{3}}\right)$ | 1 | 0 | 1 |
| $\overrightarrow{V_7} = (0,0)$ | 1 | 1 | 1 |

*Table 3.2: Switches states with regards to switching vectors.*

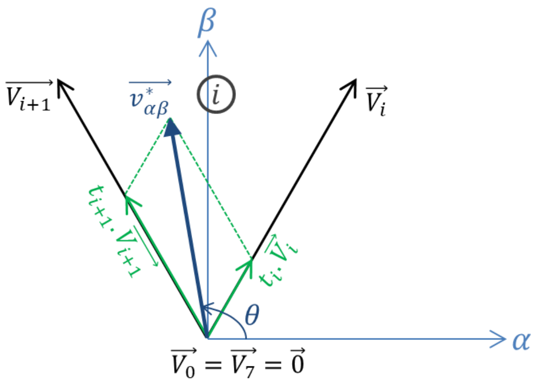

*Figure 3.14: principle for generating the reference vector in the sector $i$.*

**Computing the applying time of each vector for the combination $\overrightarrow{V_0}, \overrightarrow{V_7}, \overrightarrow{V_\iota}$ and $\overrightarrow{V_{\iota+1}}$**

Supposing $t_i$ and $t_{i+1}$ are the applying time of the active vectors $\overrightarrow{V_\iota}$ and $\overrightarrow{V_{\iota+1}}$ respectively, while $t_0$ and $t_7$ are the times when the null vectors $\overrightarrow{V_0}$ and $\overrightarrow{V_7}$ are applied, noting that the time of applying vector $\overrightarrow{V_0}$ is equal to that of vector $\overrightarrow{V_7}$ (i.e. $t_0 = t_7$) when SVPWM strategy is applied [84], [85].

$$t_0 = t_7 = \frac{T_0}{2} \tag{3.31}$$

$T_0$: The period when the null vectors $\overrightarrow{V_0}$ and $\overrightarrow{V_7}$ are applied.

The sum of applying times of active and null vectors is equal to the decoupling time $T_d = T_{PWM} = \frac{1}{f_{PWM}}$.

$$t_i + t_{i+1} + t_0 + t_7 = T_d \tag{3.32}$$

During a decoupling period $T_d$, the reference vector in the sector $i$ can be done as function of the vectors $\overrightarrow{V_0}, \overrightarrow{V_7}, \overrightarrow{V_\iota}$ and $\overrightarrow{V_{\iota+1}}$ as illustrated in Figure 3.14 and it can be generated on average by the relation:

$$T_d\overrightarrow{V_{\alpha\beta}^*} = t_0\overrightarrow{V_0} + t_i\overrightarrow{V_\iota} + t_{i+1}\overrightarrow{V_{\iota+1}} + t_7\overrightarrow{V_7}$$

$$T_d\overrightarrow{V_{\alpha\beta}^*} = t_i\overrightarrow{V_\iota} + t_{i+1}\overrightarrow{V_{\iota+1}} \tag{3.33}$$

And then in complex notation we have:

$$T_d\overline{V_{\alpha\beta}^*} = t_i\overline{V_\iota} + t_{i+1}\overline{V_{\iota+1}} \tag{3.34}$$

Assuming $\theta = \left(\vec{\alpha}, \overrightarrow{V_{\alpha\beta}^*}\right), \gamma_i = \left(\vec{\alpha}, \overrightarrow{V_\iota}\right),\ \gamma_{i+1} = \left(\vec{\alpha}, \overrightarrow{V_{\iota+1}}\right) = \gamma_i + \frac{\pi}{3}$ and $v_{\alpha\beta}^* = \left|\overrightarrow{V_{\alpha\beta}^*}\right| = m$, then the equation (3.34) can be rewritten as a system of two equations with two unknowns as shown in (3.37).

$$T_d V_{\alpha\beta}^* e^{j\theta} = t_i V_i e^{j\gamma_i} + t_{i+1} V_{i+1} e^{j\gamma_{i+1}} \tag{3.35}$$

$$T_d \cdot m \cdot e^{j\theta} = \frac{2}{3} \cdot t_i \cdot e^{j\gamma_i} + \frac{2}{3} \cdot t_{i+1} \cdot e^{j\gamma_{i+1}} \tag{3.36}$$

$$\begin{cases} T_d \cdot m \cdot \cos\theta = \frac{2}{3} \cdot t_i \cdot \cos\gamma_i + \frac{2}{3} \cdot t_{i+1} \cdot \cos\gamma_{i+1} \\ T_d \cdot m \cdot \sin\theta = \frac{2}{3} \cdot t_i \cdot \sin\gamma_i + \frac{2}{3} \cdot t_{i+1} \cdot \sin\gamma_{i+1} \end{cases} \tag{3.37}$$

By restating and manipulating the equation (3.37) as shown in Appendix C, we find the values of $t_i$ and $t_{i+1}$ as described in (3.38).

$$\begin{cases} t_i = \sqrt{3} \cdot T_d \cdot m \cdot \sin(\gamma_{i+1} - \theta) \\ t_{i+1} = \sqrt{3} \cdot T_d \cdot m \cdot \sin(\theta - \gamma_i) \end{cases} \tag{3.38}$$

Consequently, the applying time for the null vectors $\overrightarrow{V_0}$ and $\overrightarrow{V_7}$ in the case of SVPWM can be computed by (3.39).

$$t_0 = t_7 = \frac{1}{2} T_0 = \frac{1}{2}(T_d - t_i - t_{i+1}) \tag{3.39}$$

This method provides total control over the distribution of the used states, but it requires a processor with greater efficiency, and therefore more expensive to perform all the necessary calculations in a reasonable time comparing with the conventional scalar-based method.

### 3.3.5 Equivalence between scalar-based and vector-based methods

Each PWM strategy can be presented by both methods: scalar-based and vector-based approaches. Figure 3.15 shows the equivalence at the switching period scale, of these two approaches for the SPWM strategy and any other PWM strategy (such as SVPWM, THIPWM, GDPWM…) where a zero sequence component $v_{n0}$ is added to the three reference sinusoidal signals.

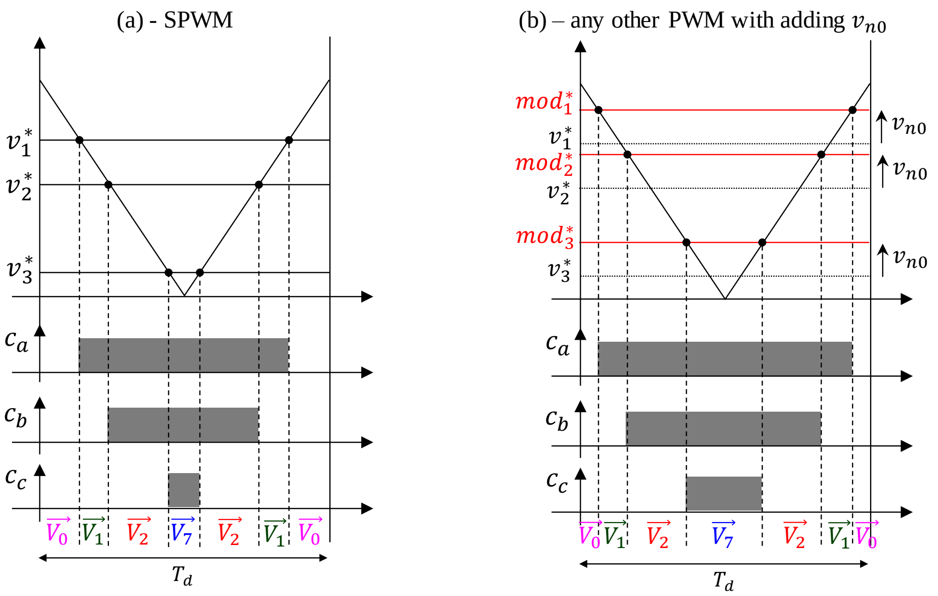
(a) - SPWM

(b) – any other PWM with adding $v_{n0}$

*Figure 3.15: Pulse patterns during a decoupling period for SPWM (a) and others PWM strategies (b).*

In the left sub-figure, the control signals of the three bridge arms are generated directly by comparing $v_1^*, v_2^*$ and $v_3^*$ with the triangular carrier (ascending-descending type). Whereas in the right sub-figure, these reference signals $v_1^*, v_2^*$ and $v_3^*$ are affected by the same zero-sequence component $v_{n0}$ to obtain new reference signals $mod_1^*, mod_2^*$ and $mod_3^*$ that will then be compared with the carrier.

As we can see clearly in Figure 3.15, both strategies generate the same sequence of vectors at the inverter output. In the first sector of the hexagon, this sequence is $\overrightarrow{V_0}, \overrightarrow{V_1}, \overrightarrow{V_2}, \overrightarrow{V_7}, \overrightarrow{V_2}, \overrightarrow{V_1}, \overrightarrow{V_0}$. Also we can notice that the duration of applying the active states (1,0,0) and (1,1,0) (which correspond to $\overrightarrow{V_1}$ and $\overrightarrow{V_2}$ respectively) still unaffected while it varies for the zero-states $(0,0,0)$ and $(1,1,1)$ (which are the correspondent states for $\overrightarrow{V_0}$ and $\overrightarrow{V_7}$ respectively).

Figure 3.16 illustrates the pulse patterns in the case of using SPWM strategy for both sectors 1 and 2 knowing that $v_1^* > v_2^* > v_3^*$ in the first sector while in the second sector $v_2^* > v_1^* > v_3^*$. Noting that $v_1^*, v_2^*$ and $v_3^*$ represent the reference voltages.

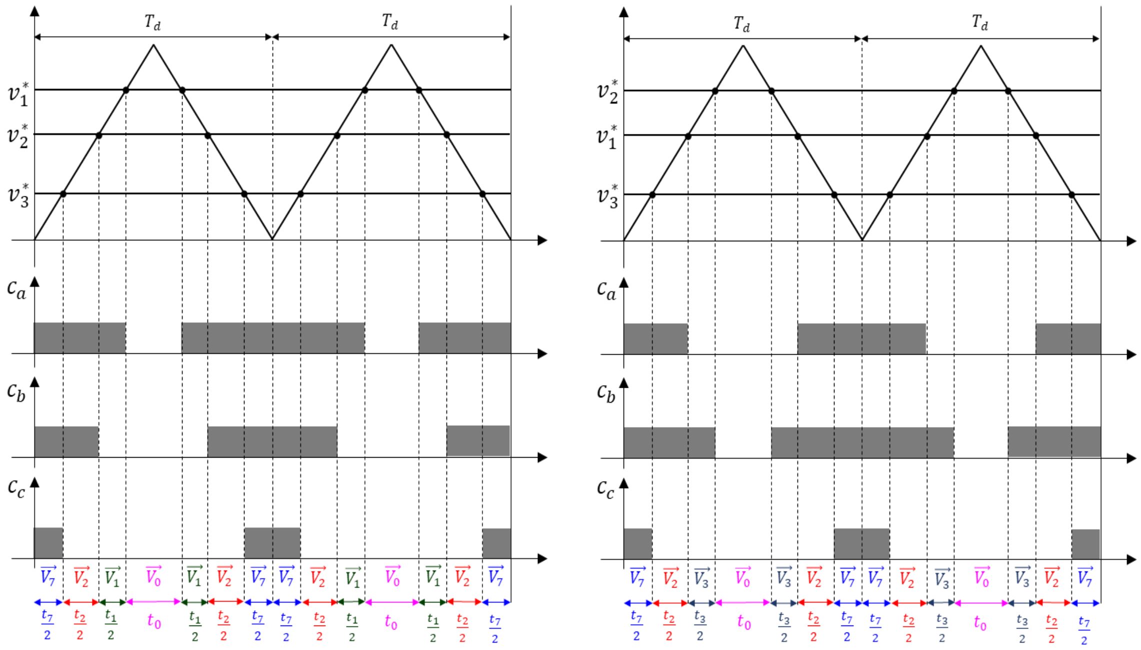
(a) - Sector 1

(b) - Sector 2

*Figure 3.16:Pulse patterns for SPWM strategy in first sector (a) and second sector (b).*

Also, Figure 3.16 allow us to compute the time of applying each vector during a switching period. For example, for the right sub-figure (sector 1) when the carrier varies between -1 and 1, the duty cycles of the three bridge arms are described in (3.40). Then the application times of each vector at the output of the inverter over each switching period $T_d$ are defined in (3.41).

$$\begin{cases} \alpha_1 = \frac{1}{2}(v_1^* + 1) \\ \alpha_2 = \frac{1}{2}(v_2^* + 1) \\ \alpha_3 = \frac{1}{2}(v_3^* + 1) \end{cases} \tag{3.40}$$

$$\begin{cases} t_0 = T_d \cdot (1 - \alpha_1) \\ t_1 = T_d \cdot (\alpha_1 - \alpha_2) \\ t_2 = T_d \cdot (\alpha_2 - \alpha_3) \\ t_7 = T_d \cdot \alpha_3 \end{cases} \tag{3.41}$$

In the case of SVPWM strategy is used, Table 3.3 shows the function of the required conduction time of each switch in the converter according to the sector number during decoupling cycle period. $T_a$ and $T_b$ represent the application time for the active vectors $\overrightarrow{V_\imath}$ and $\overrightarrow{V_{\imath+1}}$ respectively in the sector $i$, while $T_0$ is the time of applying zero-states $(0,0,0)$ and $(1,1,1)$, these times can be determined using (3.38) and (3.39).

| Sector | Upper switches | Lower switches |
|---|---|---|
| 1 | $\begin{cases} T_{S_1} = T_a + T_b + \frac{T_0}{2} \\ T_{S_2} = T_b + \frac{T_0}{2} \\ T_{S_3} = \frac{T_0}{2} \end{cases}$ | $\begin{cases} T_{S_4} = \frac{T_0}{2} \\ T_{S_5} = T_a + \frac{T_0}{2} \\ T_{S_6} = T_a + T_b + \frac{T_0}{2} \end{cases}$ |
| 2 | $\begin{cases} T_{S_1} = T_a + \frac{T_0}{2} \\ T_{S_2} = T_a + T_b + \frac{T_0}{2} \\ T_{S_3} = \frac{T_0}{2} \end{cases}$ | $\begin{cases} T_{S_4} = T_b + \frac{T_0}{2} \\ T_{S_5} = \frac{T_0}{2} \\ T_{S_6} = T_a + T_b + \frac{T_0}{2} \end{cases}$ |
| 3 | $\begin{cases} T_{S_1} = \frac{T_0}{2} \\ T_{S_2} = T_a + T_b + \frac{T_0}{2} \\ T_{S_3} = T_b + \frac{T_0}{2} \end{cases}$ | $\begin{cases} T_{S_4} = T_a + T_b + \frac{T_0}{2} \\ T_{S_5} = \frac{T_0}{2} \\ T_{S_6} = T_a + \frac{T_0}{2} \end{cases}$ |
| 4 | $\begin{cases} T_{S_1} = \frac{T_0}{2} \\ T_{S_2} = T_a + \frac{T_0}{2} \\ T_{S_3} = T_a + T_b + \frac{T_0}{2} \end{cases}$ | $\begin{cases} T_{S_4} = T_a + T_b + \frac{T_0}{2} \\ T_{S_5} = T_b + \frac{T_0}{2} \\ T_{S_6} = \frac{T_0}{2} \end{cases}$ |
| 5 | $\begin{cases} T_{S_1} = T_b + \frac{T_0}{2} \\ T_{S_2} = \frac{T_0}{2} \\ T_{S_3} = T_a + T_b + \frac{T_0}{2} \end{cases}$ | $\begin{cases} T_{S_4} = T_a + \frac{T_0}{2} \\ T_{S_5} = T_a + T_b + \frac{T_0}{2} \\ T_{S_6} = \frac{T_0}{2} \end{cases}$ |
| 6 | $\begin{cases} S_1 = T_a + T_b + \frac{T_0}{2} \\ S_2 = \frac{T_0}{2} \\ T_{S_3} = T_a + \frac{T_0}{2} \end{cases}$ | $\begin{cases} T_{S_4} = \frac{T_0}{2} \\ T_{S_5} = T_a + T_b + \frac{T_0}{2} \\ T_{S_6} = T_b + \frac{T_0}{2} \end{cases}$ |

*Table 3.3: Computing of the switching time in each sector.*

### 3.3.6 SVPWM

In the space vector approach that illustrated in Figure 3.17, the time lengths of the inverter states are pre-calculated for each carrier cycle by employing space vector theory then the voltage pulses are directly programmed. This strategy allows to have the maximum linearity area, a low voltage harmonic distortion rate and a simple implementation in real time on digital media (microcontroller, DSP, FPGA) [82], [84], [85].

By looking at Figure 3.17, we would like to recall once again that there are eight possible switching vectors for a three-leg inverter using space vector modulation from $V_0$ to $V_7$ (notice that $V_0$ and $V_7$ are zero-states while $V_1$ until $V_6$ are active states). Each vector of them represents the state of the inverter upper switches ($c_a$, $c_b$, $c_c$), it is ON-state when equal to "1" and OFF-state when equal to "0". For every PWM period, the reference vector $V_{ref}$ is averaged by using its two adjacent space vectors ($V_1$ and $V_2$ in Figure 3.17) for a certain duration from the decoupling period and null vectors ($V_0$ or $V_7$) for the rest of the period.

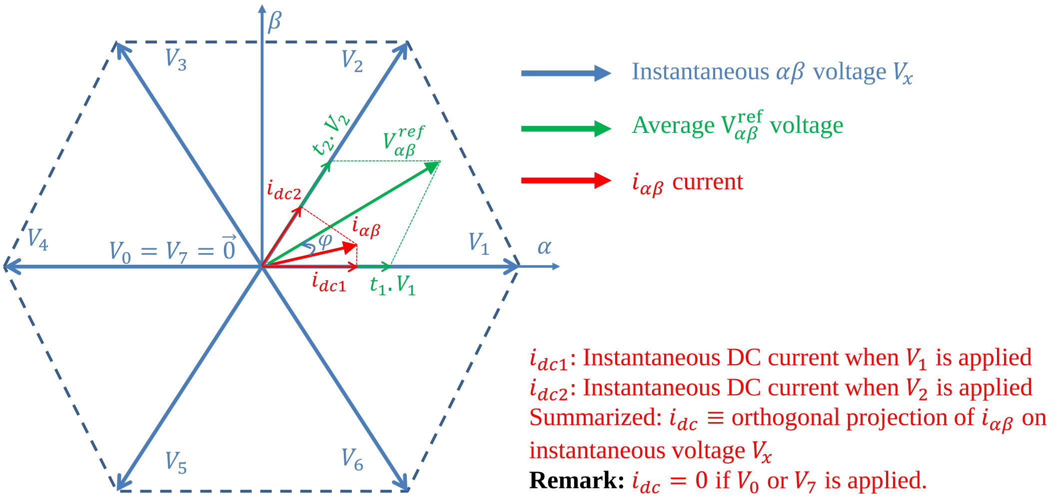

$i_{dc1}$: Instantaneous DC current when $V_1$ is applied
$i_{dc2}$: Instantaneous DC current when $V_2$ is applied
Summarized: $i_{dc} \equiv$ orthogonal projection of $i_{\alpha\beta}$ on instantaneous voltage $V_x$
**Remark:** $i_{dc} = 0$ if $V_0$ or $V_7$ is applied.

*Figure 3.17: SVPWM graphical approach.*

In regards to [86], [87], SVPWM is equivalent to sinusoidal modulation when a zero-sequence component is added to the reference signals. The freedom in selecting the partitioning of the two zero-states "$V_0$" (000) and "$V_7$" (111) in the space vector approach is equivalent to the freedom in selecting the zero-sequence signal in the scalar-based approach. Table 3.2 shows the state of each switch depending on the switching vectors.

Well, as mentioned above, and thanks to the equivalence between the vector-based and the scalar-based methods, SVPWM can be achieved using the conventional approach (Figure

3.11) after using equations (3.42), (3.43) and (3.44) [59], [64], [65], [88]. $v_a^*$, $v_b^*$ and $v_c^*$ are respectively the desired load voltage on the phase a, b and c. While $v_1^*$, $v_2^*$ and $v_3^*$ represent the normalized value with regard to $v_{dc}$. The flowchart that describes the steps of SVPWM algorithm is depicted in Figure 3.18.

$$\begin{cases} v_1^* = \frac{v_a^*}{v_{dc}} = m\cos(\theta) \\ v_2^* = \frac{v_b^*}{v_{dc}} = m\cos(\theta - \frac{2\pi}{3}) \\ v_3^* = \frac{v_c^*}{v_{dc}} = m\cos(\theta + \frac{2\pi}{3}) \end{cases} \tag{3.42}$$

$$\begin{cases} mod_1^* = v_1^* + v_{n0} \\ mod_2^* = v_2^* + v_{n0} \\ mod_3^* = v_3^* + v_{n0} \end{cases} \tag{3.43}$$

$$v_{n0} = \frac{1}{2} v_i \tag{3.44}$$

Where $i \in [1,2,3]$ is the index of $v_i$ such as $|v_i| = \min(|v_1^*|, |v_2^*|, |v_3^*|)$. Also $v_{n0}$ can be computed as expressed in (3.45).

$$v_{n0} = -\frac{1}{2}(\min(v_1^*, v_2^*, v_3^*) + \max(v_1^*, v_2^*, v_3^*)) \tag{3.45}$$

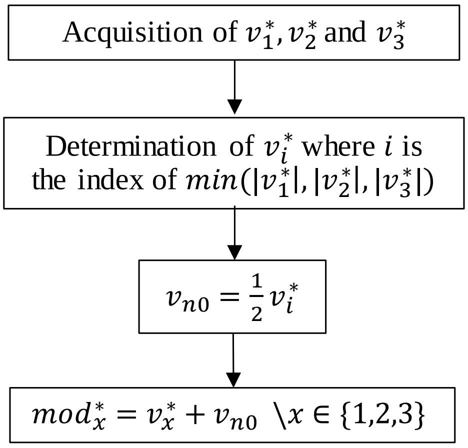

*Figure 3.18: SVPWM duty ratios calculation flowchart.*

Figure 3.19-(a) illustrates the modulating signal $mod_x^*$, reference signal $v_x^*$ and zero-voltage $v_{n0}$ in case of SVPWM strategy. While in Figure 3.19-(b), we have the carrier $c(t)$ and $mod_x^*$. As for $c_x$ that is depicted in Figure 3.19-(c), it represent the comparison result between them.

Regarding to the first plot in Figure 3.19, it is noted that the maximum of $mod_x^*$ is less than of that of $v_x^*$. Consequently, the linearity zone limit for SVPWM is larger than its of SPWM. This linearity zone has been treated in [59], [89]–[92] for various strategies, the limit of this zone is depicted in Figure 3.20 and Table 3.4 for SPWM, THIPWM4, THIPWM6 and SVPWM.

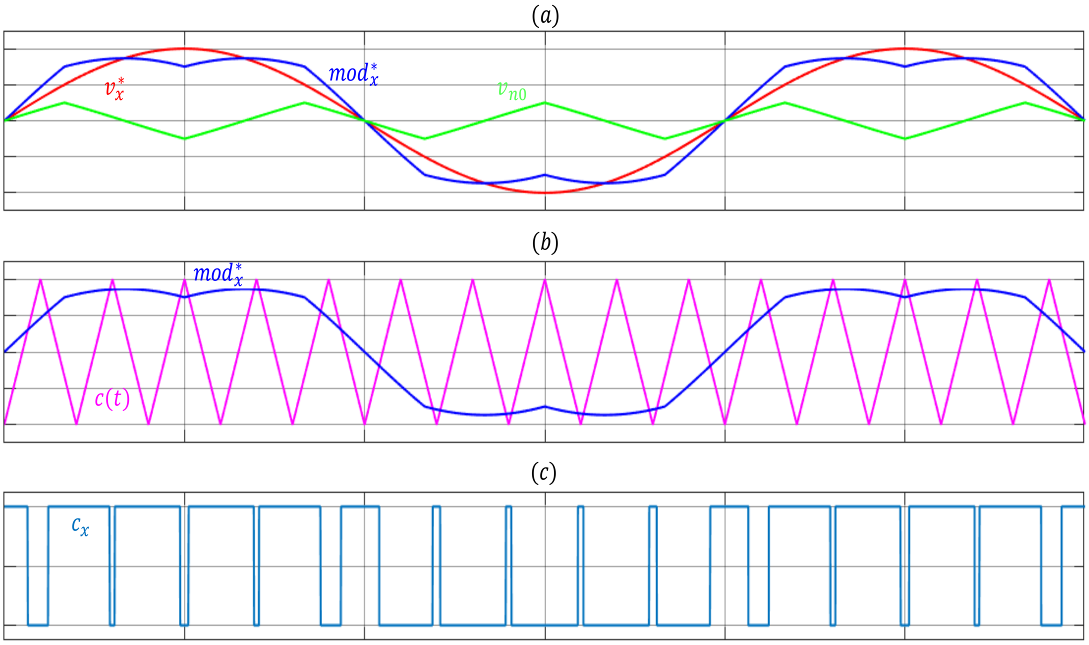

*Figure 3.19: Modulation waveform and zero-sequence signals of the SVPWM strategy.*

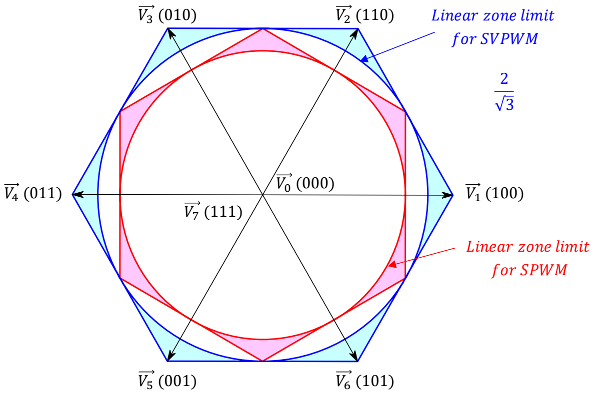

*Figure 3.20: Linear zone in the αβ plane.*

| Strategy | $m$ |
|---|---|
| $SPWM$ | 1 |
| $THIPWM4$ | $\frac{36}{7\sqrt{21}}$ |
| $THIPWM6$ | $\frac{2}{\sqrt{3}}$ |
| $SVPWM$ | $\frac{2}{\sqrt{3}}$ |

*Table 3.4: Linear zone limit for PWM strategies.*

### 3.3.7 DPWM

The injection of zero-voltage has been exploited for several purposes [93], [94]. Among them is the reduction of inverter losses [9], [10], [65], [94]–[96]. The simplest method for decreasing this loss is to decrease the number of switching. The concept may be realized by using the saturation sequences of the modulating signals during a portion of their period as illustrated in Figure 3.21-b. So, the main idea is to keep the state of a bridge arm unchanged during each decoupling period. This principle can be done by to saturating the reference during 120° of the 360° period, which prevent the switching-on the arm during this time and thus lead to gain in terms of switching losses. Because the duty ratios $a, b$ and $c$ are adjusted to zero or unity within a total of one third of the cycle, discontinuous modulating functions result in a decreased number of pulses of the switching signals , $b$ and $c$ controlling specific phases of the inverter. Hence, the switching frequency is reduced by one third in comparison with that when continuous modulating functions are used.

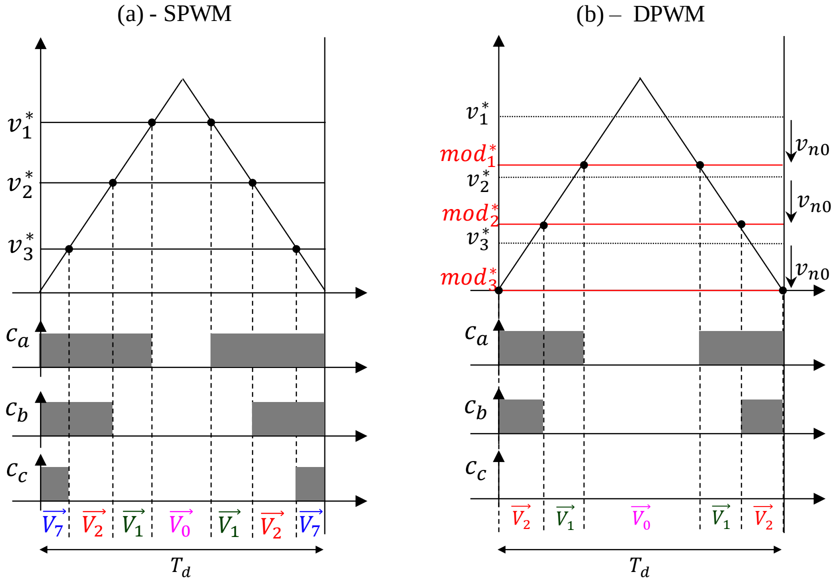
(a) - SPWM

(b) – DPWM

*Figure 3.21: PWM paterns, (a) for SPWM and (b) for DPWM .*

Based on this concept, any PWM strategies known as discontinuous PWM (DPWM), it is constituted of [8]–[10], [96]–[100]:

i. DPWM0, DPWM1, DPWM2, DPWM3: they are special cases of the GDPWM where each bridge arm is clamped to either up and down states; each for one sixth of the fundamental period. These strategies differ from each other in the clamp position with respect to the fundamental period. Consequently, each is optimal in terms of switching losses for a given power factor value of the load.

As shown in Figure 3.22, for these strategies, each modulating signal is saturated for $\alpha = 60°$ each half-period, but at different angles $\psi$ with respect to the sinusoidal reference (see Figure 3.22 and Appendix D):

- $\psi = 0°$ for DPWM0
- $\psi = 30°$ for DPWM1
- $\psi = 60°$ for DPWM2

ii. DPWMMAX, DPWMMIN: where each bridge arm is set to high (or low resp.) state for one third of a fundamental period. So these methods use only one saturation for 120°, which means adding a DC voltage to the three voltage references. This DC voltage unbalances the inverter bridge; therefore, they are rarely used because of the unbalanced switching loss distribution between the two switches on each bridge arm.

iii. GDPWM that allows minimizing switching losses in a wide range of power factor of the load, especially in the area where it is close to the unit.

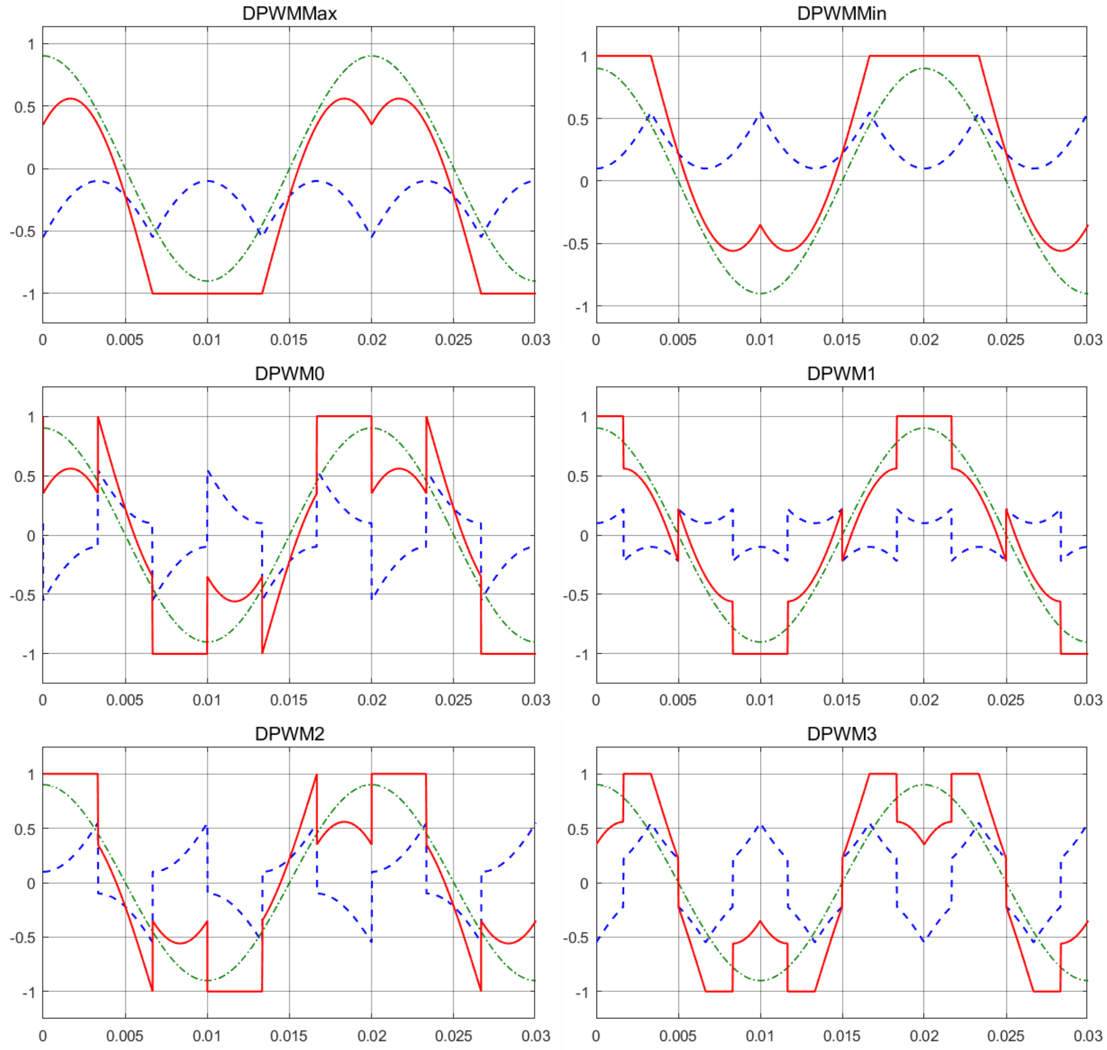

*Figure 3.22: The waveform of modulants (red), zero-sequence voltage components (blue) and reference signal (green) of different DPWM methods.*

All these strategies offer a maximum linearity extension, but the gain in losses is different each time. The comparison of the Joule losses over the whole load variation range shows that the GDPWM is the best method as illustrated in Figure 3.23.

The switching loss performance of the DPWM methods is compared to the SVPWM strategy in Figure 3.23. It can be seen that the GDPWM strategy reduces the switching losses by up to 50% compared to the SVPWM strategy.

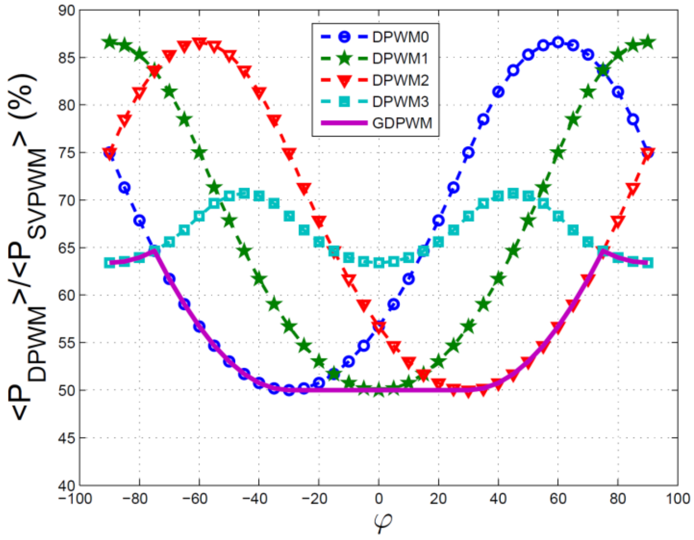

*Figure 3.23: Ratio of switching losses of DPWM strategies with respect to SVPWM strategies as a function of load power factor [59].*

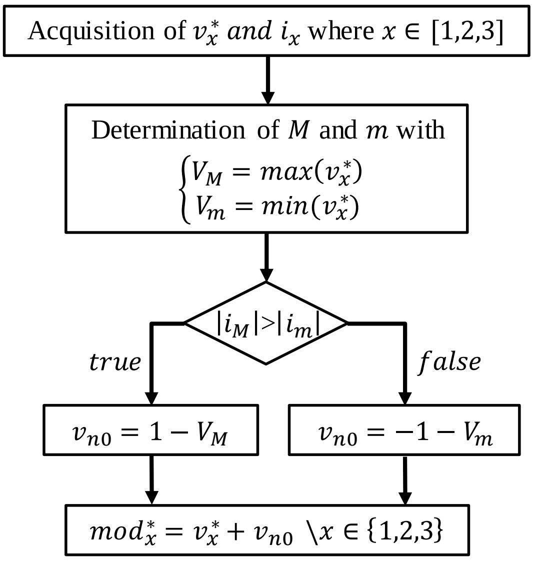

*Figure 3.24: GDPWM duty ratios calculation flowchart.*

The advantages of the GDPWM method [10], [59], [76], [96]:

- The method provides up to 50% reduction in switching losses per arm and up to 30% reduction in total losses compared to the currently used three-phase PWM. This is the maximum loss reduction achievable by two-phase modulation strategies;
- The losses remain symmetrically distributed on one arm, which is not valid for DPWMMIN. This does not unbalance the inverter bridge and does not require a different dimensioning of the top and bottom of the arm.
- The maximum linearity extension of the two-level inverter is always guaranteed;

Some studies present another modulation strategy which is called dual-carrier or double carrier PWM that reduces the RMS value of the current absorbed by the capacitors [5].

The flowchart that describes the steps of GDPWM algorithm is depicted in Figure 3.24.

### 3.3.8 DCPWM

Supposing that the absorbed current by the decoupling capacitors is the oscillating part of the inverter input current $i_{dc}$. Obviously, the average value of $i_{dc}$ can only come from the source but we will also admit that the impedance of the capacitors is negligible in front of the equivalent impedance ($Z_{th}$) of the cable and the source for all the spectral components of the fluctuating part of $i_{dc}$. Therefore, the current coming from the source $i_s$ will be assumed to be constant and thus the entire fluctuating term of $i_{dc}$ flows entirely through the decoupling capacitors as described in (3.49) (see Figure 3.25).

$$i_s = i_{dc} + i_C \tag{3.46}$$

Assuming that:

$$i_{dc} = I_{dc} + \tilde{i}_{dc} \tag{3.47}$$

$$i_C = \overbrace{I_C}^{<i_C>=0} + \tilde{i}_C = \tilde{i}_C \tag{3.48}$$

$I_{dc}$, $\tilde{i}_{dc}$ , $I_C$ and $\tilde{i}_C$ represent the average and oscillating terms for the currents of DC-link and decoupling capacitor respectively.

Or $i_s = constant = I_{dc}$, then by using (3.46), (3.47) and (3.48) we get:

$$i_C = \tilde{i}_C = -\tilde{i}_{dc} \tag{3.49}$$

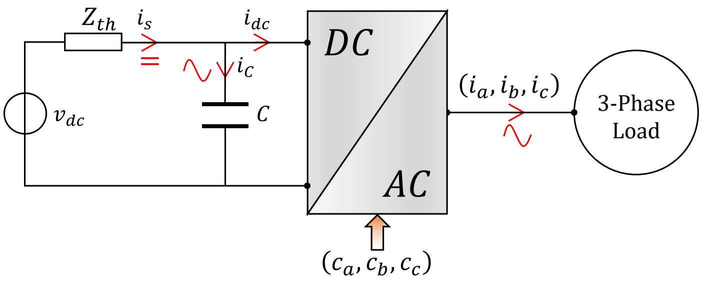

*Figure 3.25: Simplified circuit to calculate the effective current absorbed by the decoupling capacitors.*

Consequently, in order to reduce the current flowing in the capacitors, the fluctuating part of the DC-link should be reduced. This later is treated and achieved by DCPWM strategy that is proposed in [63].

DCPWM is another type of PWM strategies, which use two carriers in phase opposition to each other [7], [11], [59], [63]. The strategies studied in [64], [66] aim to reduce the common mode voltage ripple which is a result of semiconductor switching pulses, while [6], [59] focused on the reduction of the RMS current in decoupling capacitors. All these controls use a classical scalar approach with two opposite carriers instead of one.

From vector-based approach's point of view, instead of using two adjacent active vectors and zero vectors during each switching period to generate the reference vector, DCPWM strategies use three adjacent active vectors or two non-adjacent active vectors and one zero vector as depicted in Figure 3.26. Both cases are applied according to the positon of the reference vector $V^*$ in different zones (see Figure 3.27).

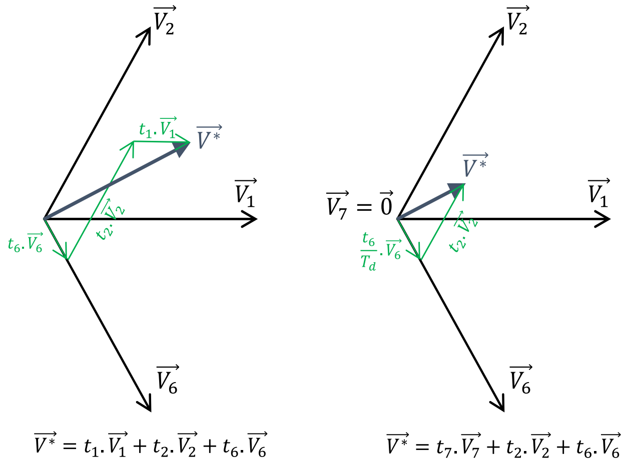

*Figure 3.26: Vector-based principle of the DCPWM strategy.*

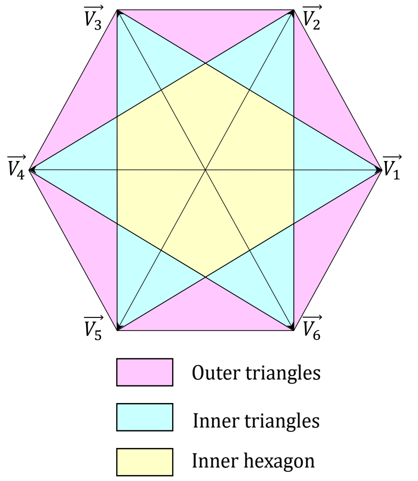

*Figure 3.27: Various zones of the DCPWM strategy.*

Referring to [59], the instantaneous value of the DC-link current $i_{dc}$ is expressed, in the plane $\alpha\beta$, by a scalar product between the "normalized voltage" vector $\overrightarrow{V_k}$ at the output of the inverter and the vector of the load current $\vec{I}$ as mentioned in (3.50). In other words the instantaneous value of $i_{dc}$ is (multiplied by a coefficient of 3/4) the orthogonal projection of the vector $\vec{I}$ onto the vector $\overrightarrow{V_k}$.

$$i_{dc} = \frac{3}{4}\overrightarrow{V_k}\cdot\vec{I} \qquad (3.50)$$

This representation thus all having the instantaneous value of $i_{dc}$ graphically as illustrated in Figure 3.28.

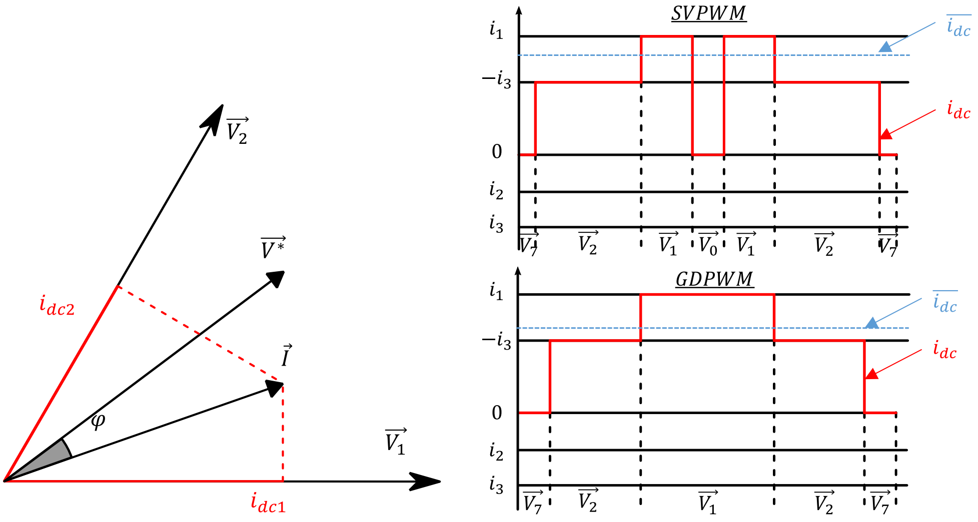

(a) In the $\alpha\beta$-plane (b) Instantaneous value

*Figure 3.28: DC-link current during a decoupling periode.*

**Uni-DCPWM:**

Applying of zero vectors ($V_0$ and $V_7$) leads to significant current ripples at the input of the inverter. In fact, this ripple is a great interest in the dimensioning of DC link capacitors.

In general, the principle concept of DCPWM technique is to strictly avoid the application of freewheel vectors ($V_0$ and $V_7$) where possible. But this technique isn't appropriate for lowest modulation factor range $m \leq \frac{2}{3}$. Therefore, the aim of the Uni-DCPWM technique is to benefit from DCPWM advantage even if the modulation factor is small (i.e. $m \leq \frac{2}{3}$). Its implementation requires following the flow chart described in Figure 3.29.

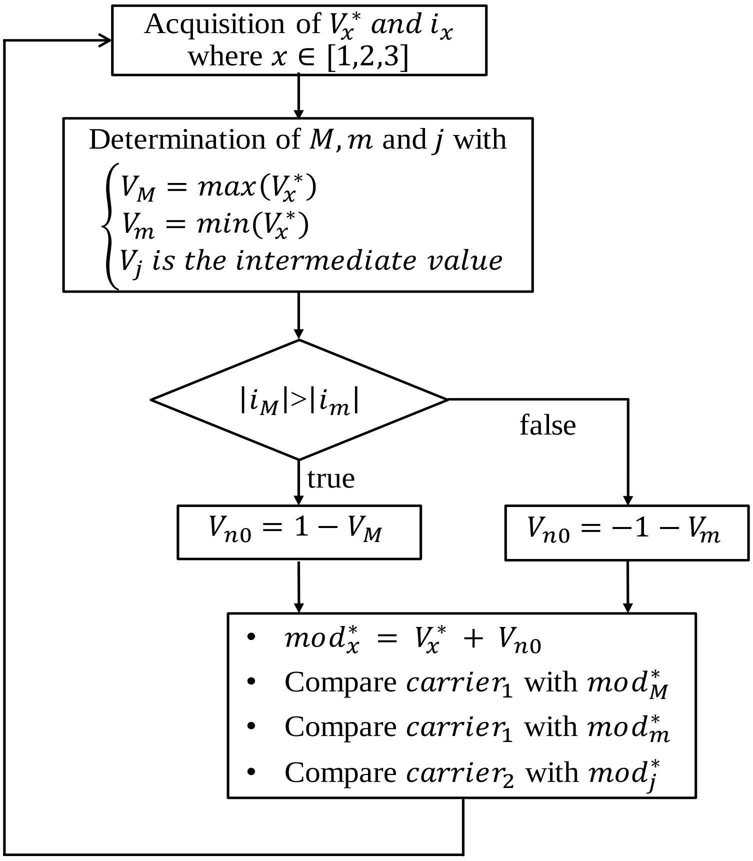

*Figure 3.29: Uni-DCPWM flowchart.*

Figure 3.30 illustrates the cartography of the ratio between RMS current for Uni-DCPWM and SVPWM strategies as a function of the phase shift $\varphi$ of the AC load and of the modulation factor $m$.

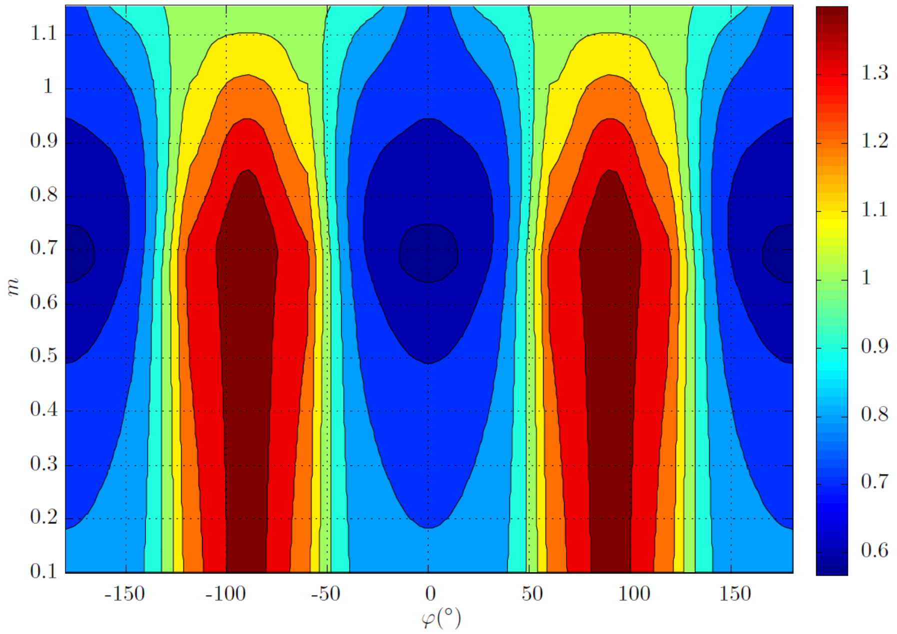

*Figure 3.30: Ratio between RMS current for Uni-DCPWM and SVPWM strategies as a function of the phase shift $\varphi$ of the AC load and of the modulation [59].*

It can be noted that in the high power factor area ($-50° \leq \varphi \leq 50°$ motor mode and $150° \leq |\varphi| \leq 180°$ generator mode), the ratio is less than 1, which means that the Uni-DCPWM strategy is more advantageous than the SVPWM strategy in this area in terms of decoupling capacitor stress. This ratio can go below 0.6, i.e. the reduction in current value is more than 40% compared to the SVPWM strategy.

## 3.4 Conclusion

The structure of the three-phase full bridge converter is well addressed in this chapter. It has touched on the converter component (switches) and its operating principle by presenting the possible status of each leg and which case should be avoided by adding a dead time delay between the switches transition in order to prevent happening a short-circuit. Also, the functions of the output voltages and the input currents have been expressed with regard to the input voltage and the switches states control signals ($c_a, c_b, c_c$). Then, the concept of controlling the converter has been treated by proposing different PWM methods. Each PWM strategy has a specific characteristics like the zero-sequence voltage $v_{n0}$ and algorithm, which leads to different advantages. For instance, SVPWM can increase the modulation index range with respect to SPWM and it can improve the phase current quality. While the DPWM strategies focus on the reduction of the switching losses (conduction and commutation). As for Uni-DCPWM, it aims reducing the stress on the decoupling capacitor and limit the switching losses too.

After we have touched on the DFIM, its control and the operating of the static converter, we are able to start in next chapter to study the global system including a back-to-back converters connected to the grid from one side and to the machine on the other side.

# Chapter 4: Back-to-back converter system

## 4.1 Introduction

In the literature, different Pulse Width Modulation (PWM) strategies based on a double carrier have been developed in order to reduce the current in the DC link capacitor within the context of a single three-phase full bridge in comparison with classical (single carrier space vector PWM strategies). These techniques are presented in [5], [63] and [12]. The last one can be easily implemented on a DSP and is efficient for all practical operating points (for all modulation indexes and all usual power factors both in motor and generator modes). Recent papers treating the DC link capacitors focus on multi-phase converters [101]. It has been shown in [102] that the reduction of the RMS current is important for the reduction of the size of DC link capacitors (or the reduction of their stress), especially in low voltage high current applications where they represent an important part of the overall volume of the converter. Indeed, in practice, the DC voltage ripple is never the tightest constraint for the design of the converter and, as a consequence, the capacitance is not the key parameter for the choice of aluminum electrolytic capacitors used within this context.

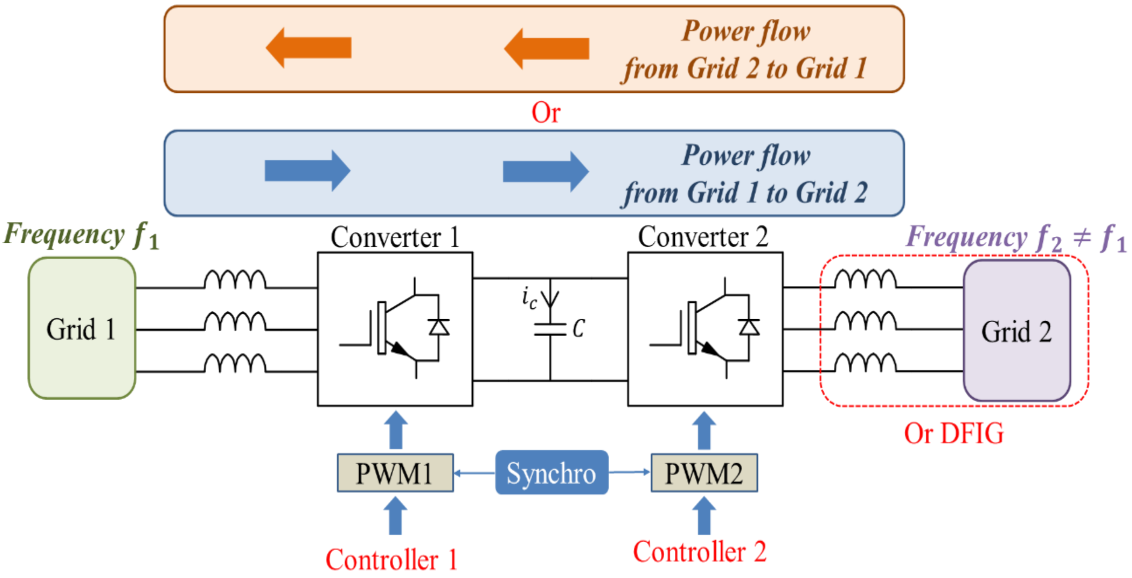

*Figure 4.1: Two back-to-back converters.*

All these studies have been performed in the case of a battery-fed inverter (in an electric or hybrid vehicle) for instance. However, other important cases that can be investigated are parallelized converters [102], [103] and another interesting configuration is the back-to-back topology [61] (as shown in Figure 4.1) which can be found in various applications such as Doubly-Fed Induction Generators (DFIG) used as Variable Speed Constant Frequency Generators (wind mills [51], small hydropower [104]). With two separate converters connected to a common point (DC link), an interleaved PWM technique is usually adopted (e.g. Voltage Regulation Modules dedicated to microprocessors) because it allows us to increase the effective frequency of the current in the capacitor in comparison with the switching frequency applied to the active components in the converters. This solution has been adopted in [102] and [103] clearly focused on the DC capacitor current.

The aim of this chapter is also the reduction of the RMS current. For this purpose, individual PWM strategies are applied for both converters, and more particular we will see the impact on the DC-link current for two different PWM strategies:

- Classical SVPWM with one carrier per converter
- Uni-DCPWM with two opposite carriers per converter

And as shown in Figure 4.2, interleaved carriers are used for these PWM controllers.

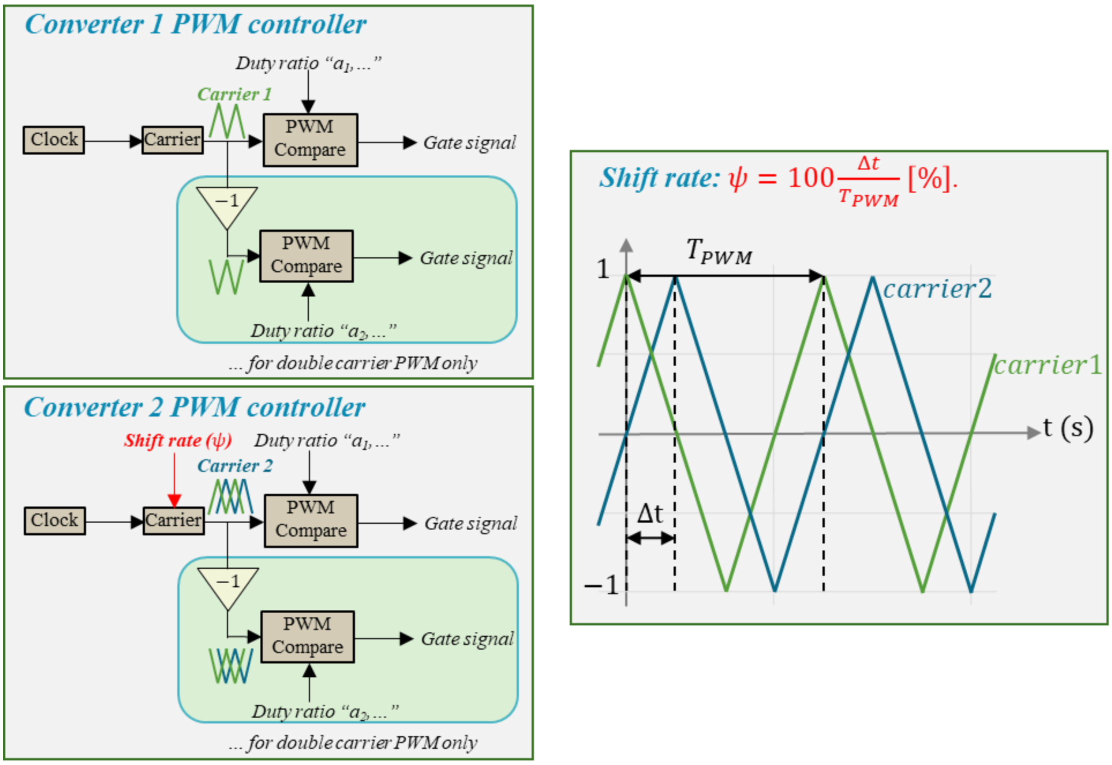

Figure 4.2: PWM carriers interleaving principle.

It must be noticed that, even if the Uni-DCPWM strategy has better performance than a SVPWM strategy for a single converter, this result has to be proved in the case of two back-to-back converters. So, the innovating aspect of this work is to compare the performance of both strategies in the context of interleaving of carriers. Then, it will be shown that the needed interleaving rate has to be dynamically tuned in order to reach the optimal performance and a simple tracking technique is tested in simulation.

In both cases, a shift rate $\psi$, which is described in (4.1), is applied between carriers of both converters, where $T_{PWM}$ is the common switching period or the decoupling period and $\Delta t$ is the delay introduced between carriers as shown in Figure 4.2.

$$\psi = 100 * \frac{\Delta t}{T_{PWM}} \tag{4.1}$$

The carriers used in this study are symmetric triangles (a complementary study with a saw-tooth waveform could be easily done).

Grid frequencies $f_1$ and $f_2$ are usually different and in practice (with a DFIG), $f_2$ is much lower than $f_1$. Therefore, results presented in this chapter are given with $f_1 = 50\,Hz$ and $f_2 \in [-15Hz, +15Hz]$. Moreover, phase shift between voltages and currents are neglected on grid 1 and grid 2. In this chapter, the study is limited to real power transfer.

In Section 4.2, the instantaneous model of a three-phase inverter is presented and then, assumptions about splitting of low and high frequencies of the DC current are recalled in order to justify the previously published results in the cases of SVPWM and Uni-DCPWM strategies about the capacitor RMS current. These results and recalled in Section 4.3.

In Section 4.4, the simulation of the interleaving impact is detailed and the complete system is briefly described. In Section 4.5, simulation results for SVPWM and Uni-DCPWM are analyzed and compared. A spectrum analysis is also performed in order to evaluate the possibility of choosing another technology for DC link capacitors.

In Section 4.6, a real-time control is developed. It is based on a tracking technique. It aims to dynamically tune the interleaving rate when the operating point is modified in order to achieve optimal results. Finally, the conclusion highlights the interest of Uni-DCPWM within this new context and proposes an optimal interleaving strategy in the case of a unity power factor operating mode of both converters.

## 4.2 Modeling

In this part, we are going to model each part of the back-to-back converter system illustrated in Figure 4.3. Firstly, we will talk about the source, the load then we will treat the converters part, and finally the DC-link will be dealt.

In order to establish a cartography of dc-link capacitor RMS current for many operating points, a large amount of transient simulations has to be performed. As a consequence, a simple global model is needed. Therefore, the DFIG (the load) is not modeled as presented in Chapter 1: but as a three-phase RLE series similar to the model of the source (utility grid).

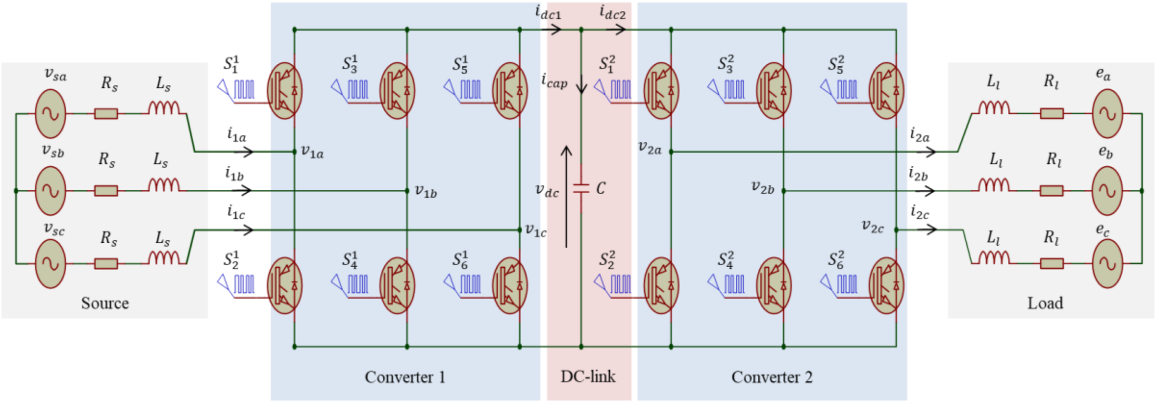

*Figure 4.3: Back-to-back converter system.*

### 4.2.1 Source modeling

Supposing that we have a balanced three-phase grid. According to Kirchhoff's voltage law (KVL), its mathematical model is presented in equation (4.2).

$$v_{1x} = v_{sx} - R_s i_{1x} - L_s \frac{di_{1x}}{dt} \qquad x = (a, b, c) \tag{4.2}$$

$v_{sx}$: $x$-phase voltage of the source.

$i_{1x}$: $x$-phase current of the source or incoming current into first converter.

$R_s$ and $L_s$: Resistor and inductor of the grid side filter.

$v_{1x}$: The applied voltage on the rectifier (first converter).

By reorganizing (4.2), we can compute the values for the rectifier input current $i_1 = (i_{1a}, i_{1b}, i_{1c})^T$.

$$i_1 = \begin{bmatrix} i_{1a} \\ i_{1b} \\ i_{1c} \end{bmatrix} = \frac{1}{(R_s + L_s.s)}(v_s - v_1) = \frac{1}{(R_s + L_s.s)} \begin{bmatrix} v_{sa} - v_{1a} \\ v_{sb} - v_{1b} \\ v_{sc} - v_{1c} \end{bmatrix} \tag{4.3}$$

Where $s$ represents the Laplace operator.

By using Park transformation, equation (4.2) can be reformulated in $dq$-frame as mentioned in (4.4) for control purpose.

$$\begin{cases} v_{1d} = v_{sd} - R_s i_{sd} - L_s \dfrac{di_{sd}}{dt} + \omega_1 L_s i_{sq} \\ v_{1q} = v_{sq} - R_s i_{sq} - L_s \dfrac{di_{sq}}{dt} - \omega_1 L_s i_{sd} \end{cases} \tag{4.4}$$

Where $v_{1d}$ and $v_{1q}$ are direct and quadrature applied voltages respectively on the rectifier in synchronous reference frame. $\omega_1$ is the grid side frequency ($rad/s$).

### 4.2.2 Load modeling

Take into consideration that the load is a RLE balanced three-phase system (which is a simplified model of the DFIG) similar to the source model with a resistor $R_l$, inductor $L_l$ and source voltage $e_x$, the only different between equations of the source and the load is the current direction. As consequence, voltages can be expressed as follows:

$$v_{2x} = R_l i_{2x} + L_l \frac{di_{2x}}{dt} + e_x \quad x = (a, b, c) \tag{4.5}$$

By reorganizing (4.5), we can compute the values for the inverter output current $i_2 = (i_{2a}, i_{2b}, i_{2c})^T$.

$$i_2 = \begin{bmatrix} i_{2a} \\ i_{2b} \\ i_{2c} \end{bmatrix} = \frac{1}{(R_l + L_l.s)}(v_2 - E) = \frac{1}{(R_l + L_l.s)} \begin{bmatrix} v_{2a} - e_a \\ v_{2b} - e_b \\ v_{2c} - e_c \end{bmatrix} \tag{4.6}$$

Where $s$ represents the Laplace operator.

Then, if needed for control purpose, a $dq$- model can be derived from equation (4.5):

$$\begin{cases} v_{2d} = R_l i_{ld} + L_l \frac{di_{2d}}{dt} - \omega_2 L_l i_{2q} + e_d \\ v_{2q} = R_l i_{2q} + L_l \frac{di_{2q}}{dt} + \omega_2 L_l i_{2d} + e_q \end{cases} \qquad (4.7)$$

### 4.2.3 Rectifier/Inverter modeling

Concerning the three-phase voltage vector $v_1 = (v_{1a}, v_{1b}, v_{1c})^T$for the first converter (rectifier) or $v_2 = (v_{2a}, v_{2b}, v_{2c})^T$ for the second converter (inverter), their function is shown in equation (4.8), it depends on the DC-link voltage value $v_{dc}$ and the switches state $C_k$ multiplied by matrix $G$ (see equation (3.7)), where $k$ allows us to distinguish both converters:

$$v_k = v_{dc}.G.C_k \quad \begin{cases} k = 1\, for\ first\ converter \\ k = 2\, for\ second\ converter \end{cases} \qquad (4.8)$$

### 4.2.4 DC bus modeling

Basing on the Figure 4.3 and the Kirchhoff's current law, the output rectifier current $i_{dc1}$ merges three currents $i_{1a}, i_{1b}$ and $i_{1c}$ depending on the state of switches $c_{1a}, c_{1b}$ and $c_{1c}$. In the same way, the input inverter current $i_{dc2}$ is divided into three current $i_{2a}, i_{2b}$ and $i_{2c}$ depending on the state of switches $c_{2a}, c_{2b}$ and $c_{2c}$. Basing on (3.9), $i_{dc1}$ and $i_{dc2}$ are mentioned in (4.9).

$$i_{dc,k} = C_k.i_k = c_{ka}i_{ka} + c_{kb}i_{kb} + c_{kc}i_{kc}. \begin{cases} k = 1\, for\ first\ converte \\ k = 2\, for\ second\ conver \end{cases} \qquad (4.9)$$

Finally, the DC bus voltage is characterized by equation (4.11), the current coming from the rectifier $i_{dc1}$ is split in two terms, the first is the current that come in the decoupling capacitor $i_{cap}$. While the second term correspond to the inverter input current $i_{dc2}$. Finally, the voltage $v_{dc}$ on the capacitor is taken to be applied on the inverter input.

$$i_{cap} = i_{dc1} - i_{dc2} \qquad (4.10)$$

$$v_{dc} = \frac{1}{C.s} i_{cap} = \frac{1}{C.s}(i_{dc1} - i_{dc2}) \qquad (4.11)$$

$C$: The capacitance value for the decoupling capacitor.

Suppose that $i_{dc1}$ and $i_{dc2}$ are calculated using (4.9), therefore (4.10) and (4.11) lead to find two unknowns variables $i_{cap}$ and $v_{dc}$ respectively. They can be done using a control diagram represented in Figure 4.4.

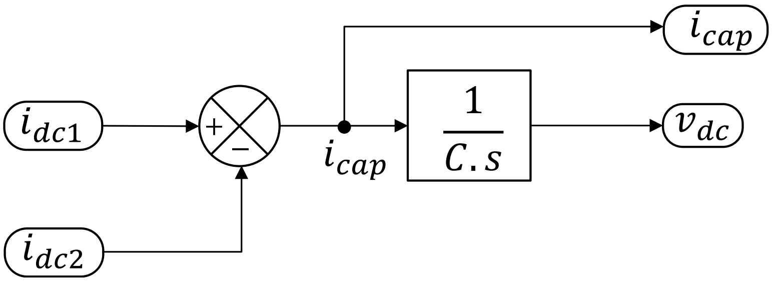

*Figure 4.4: DC bus circuit bloc diagram.*

By using Clarke's transformation (Appendix A), the equations (4.8) and (4.9) can be reformulated as in (4.12) and (4.13) respectively.

$$\begin{bmatrix} v_\alpha \\ v_\beta \end{bmatrix} = \frac{2}{3} v_{dc} \begin{bmatrix} 1 & -\frac{1}{2} & -\frac{1}{2} \\ 0 & \frac{\sqrt{3}}{2} & -\frac{\sqrt{3}}{2} \end{bmatrix} \begin{bmatrix} c_a \\ c_b \\ c_c \end{bmatrix} \tag{4.12}$$

$$i_{dc} = \frac{2}{3} \begin{bmatrix} c_a & c_b & c_c \end{bmatrix} \cdot \begin{bmatrix} 1 & 0 \\ -\frac{1}{2} & \frac{\sqrt{3}}{2} \\ -\frac{1}{2} & -\frac{\sqrt{3}}{2} \end{bmatrix} \cdot \begin{bmatrix} i_\alpha \\ i_\beta \end{bmatrix} \tag{4.13}$$

Based on (4.12), the dot product occurring in (4.13) can be rewritten as:

$$i_{dc} = \frac{1}{v_{dc}} \begin{bmatrix} v_\alpha & v_\beta \end{bmatrix} \cdot \begin{bmatrix} i_\alpha \\ i_\beta \end{bmatrix} \tag{4.14}$$

Figure 4.5 shows the overall functional block diagram for back-to-back converter that is performed in Simulink in order to simulate the system and present the results. As it seems, the system requires four inputs source and load voltages ($v_s$ and $e$ respectively), also, the switches states signals $C_1$ and $C_2$ that come from PWM strategies blocs to control the converters.

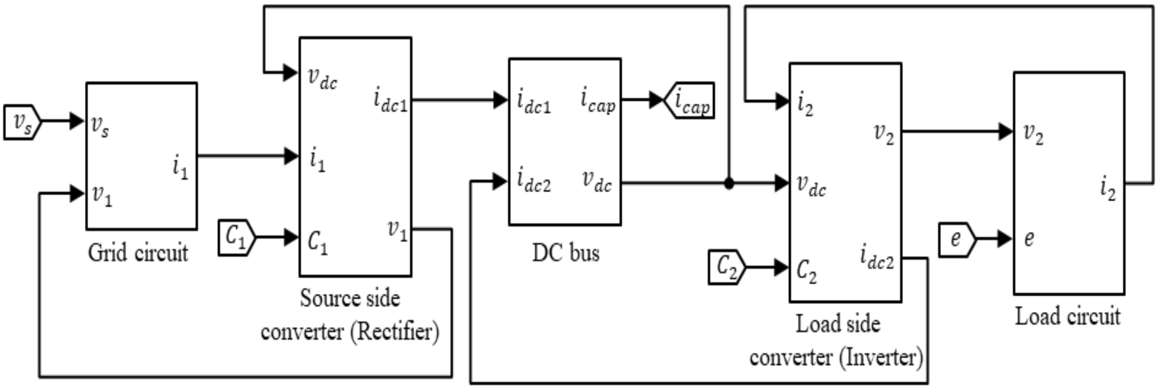

*Figure 4.5: Block diagram for back-to-back converter.*

Due to the interaction of the converters in the configuration that presented in Figure 4.6, the situation is much more complex than one converter case. Indeed, the result about RMS capacitor current is not trivial even if the PWM controllers associated to the converters are synchronized with the same carrier. That is because constructive and destructive interferences can occur. This latter is due to different spectrum distributions of $i_{ac1}$ and $i_{ac2}$ linked to different operating points of the rectifier and the inverter (even if the DC components remain the same for both converters).

As a consequence, it is not possible to conclude about the effectiveness of a PWM strategy in this back-to-back topology on the basis of the performances obtained in a single converter configuration.

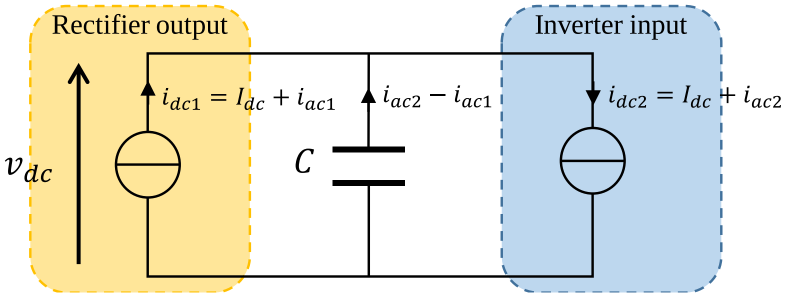

*Figure 4.6: the configuration of a DC-link with two converters.*

### 4.2.5 Control loops

Figure 4.7 illustrates two control loops in synchronous frame ($dq$ reference frame). At the top (the control loop for the first converter which is a rectifier), we have DC voltage loop. This loop is used to find the desired voltages $v_{1a}^*$, $v_{1b}^*$ and $v_{1c}^*$ that have to be injected into the first converter's PWM strategy, they are calculated based on the desired DC-link voltage

$v_{dc}^{*}$. This loop includes two controllers, the inner current controller and the outer voltage controller.

At the bottom of Figure 4.7, we have the current control loop for the second converter (inverter). This control loop is applied in order to determine $v_{2a}^{*}$, $v_{2b}^{*}$ and $v_{2c}^{*}$, which are the input reference voltages of the second converter's PWM strategy. They are computed using current controller that regulates the load current $i_{2a}^{*}, i_{2b}^{*}$ and $i_{2c}^{*}$ or their maximum $I_{2_{max}}^{*}$in $dq$ frame.

Also, as it seems, the interleaving time is inserted to make shifting or to add delay between career of both PWM strategies. The aim is to monitor, observe and visualize its effect on the decoupling capacitor current $i_{cap}$, which is the output of the DC bus bloc in Figure 4.5.

**Note:** The shift rate value is set to zero in the beginning in order to prove the control loops work well.

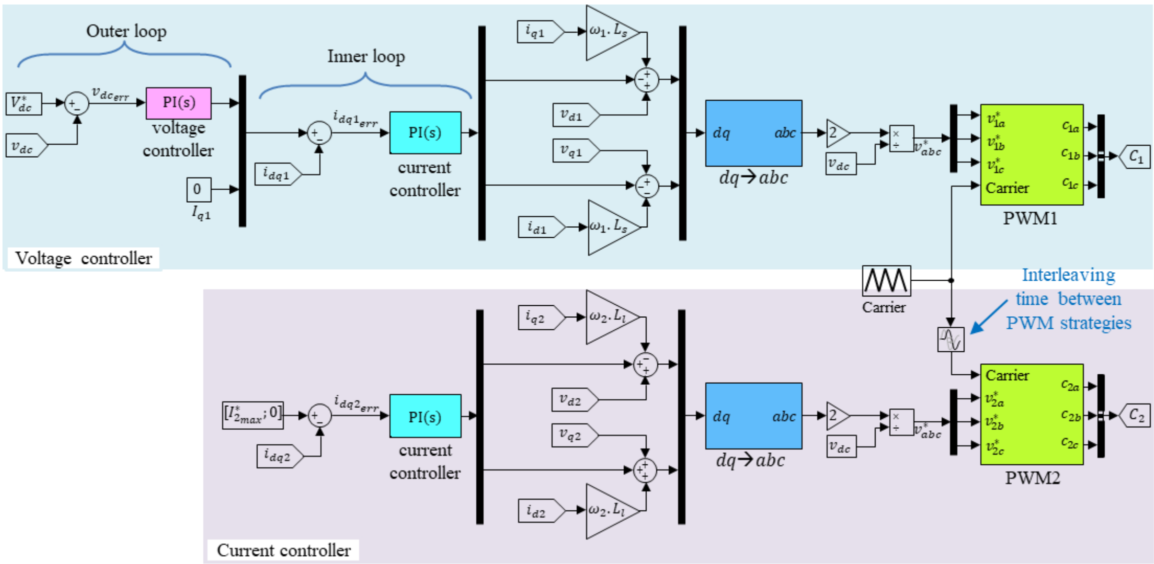

*Figure 4.7: Control loops and insertion of interleaving time.*

Figure 4.8 illustrates the load current $i_2$ and the DC-link voltage $v_{dc}$in the case of applying SVPWM strategy. The simulation is performed with consideration that desired DC voltage is $V_{dc}^{*} = 722V$ and load current peak is $I_{2_{max}}^{*} = 10A$ without any delay between the PWM strategies of converters.

The simulation results provided in Figure 4.8 verify the accuracy and success of the control loops and the modeling of the various parts in the back-to-back converter.

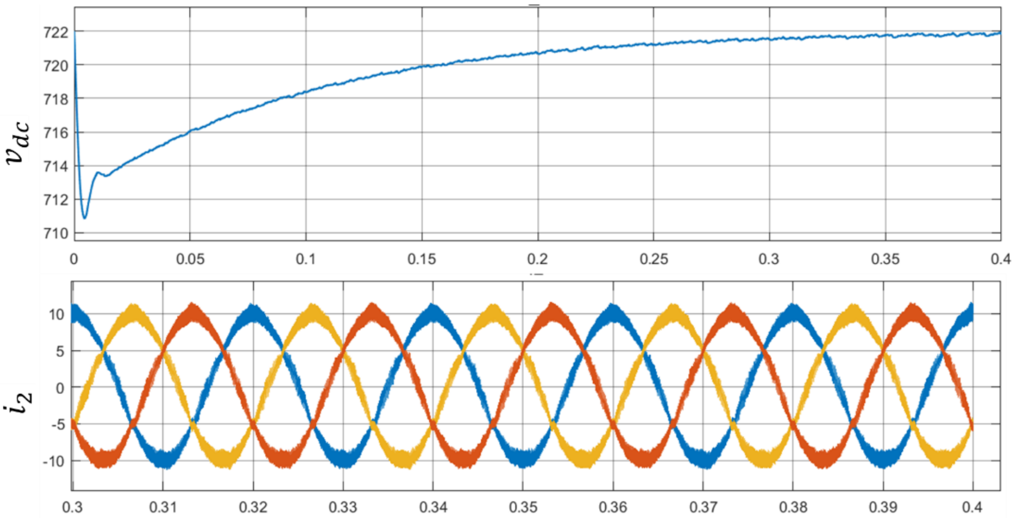

*Figure 4.8: Test for PWM rectifier control.*

## 4.3 Studied PWM strategies

### 4.3.1 Space vector PWM

Many PWM strategies can be used for the control of a three-phase full bridge due to the available degrees of freedom such as zero sequence component on the AC side. This study is limited to constant frequency PWM strategies.

Within this context, a logical choice is to analyse the widely used SVPWM technique, which can be seen as a single carrier intersective PWM using a specific zero sequence $v_{n0}$ component added to sinusoidal references as shown in section 3.3.6.

It leads to a low distortion of the AC voltages with a maximal available amplitude of fundamental voltages $\frac{v_{dc}}{\sqrt{3}}$ without over-modulation but:

- All legs switch two times per switching period.
- Zero voltages vector $\overrightarrow{V_0}$ and $\overrightarrow{V_7}$ are both used per switching period.

These drawbacks correspond to non-optimal switching losses and sub-optimal RMS value of the AC component $i_{ac}$ of the input current $i_{dc}$. It must be noticed that the RMS current in the DC link capacitor has been analytically expressed as in (4.15) [105].

$$i_{c-RMS} = I_{max} \times \sqrt{\frac{\sqrt{3}m}{4\pi} + \left(\frac{\sqrt{3}m}{4} - \frac{9m^2}{16}\right)\cos^2(\varphi)} \qquad (4.15)$$

Where $I_{max}$, $\varphi$ and $m$ are respectively, the amplitude of AC currents, the phase shift between AC voltages and currents and $m$ is the modulation index.

Moreover, this result is not only limited to the SVPWM but also applied to the basic sinusoidal PWM and more generally to all strategies using only two adjacent vectors (including active and zero vectors) during a switching period.

These issues (sub-optimal switching losses and RMS current in the DC link capacitor) are both addressed by the Uni-DCPWM strategy. However, no analytical result (similar to (4.15)) has been established in the literature for double carrier PWM strategies [5], [12], [63]. For this purpose, numerical analysis has been used and the same methodology can be applied here with two converters as exposed in the following paragraph.

### 4.3.2 Uni-DCPWM

The Uni-DCPWM is derived to a single carrier discontinuous PWM technique called GDPWM [95] which consists in adding a zero sequence component clamping a leg to one rail of the DC bus during a complete switching period. The interest of such behavior is the limitation of switching losses, which are proportional to the switched current. The decision of the algorithm is based on the actual currents (absolute value) measured in the potentially clamped legs (either the one with the maximal requested duty ratio - without zero sequence component - or the one with the minimal duty ratio).

Then, the Uni-DCPWM only uses two opposite carriers for modulation of non-clamped legs. The interest of a double carrier strategy (as shown in [5], [12], [63]) is that it avoids, or at least, it limits the use of zero voltage vectors $\overrightarrow{V_0}$ and $\overrightarrow{V_7}$ which dramatically increase ripples of the input current. According the assumption presented in Figure 3.25 (total AC component flowing through the capacitor), the Uni-DCPWM significantly reduces the RMS current in the capacitor of a single converter as shown in Figure 3.30.

Unfortunately, in the literature, no explicit function has been derived from double carrier techniques such as the original DCPWM presented in [63], Uni-DCPWM [12] or even the intermediate solution so-called Ext-DCPWM presented in [12]. This is mainly due to the non-linear behavior of such kinds of PWM strategies which calculate duty ratios (and select one carrier or its opposite) not only on the basis of voltage references but also on measured AC currents.

However, the calculation of the RMS capacitor current can be based on idealized current waveforms since high frequency ripples can be neglected in practice. Thus, based on (4.14) and since the DC components of $i_{dc1}$ and $i_{dc2}$ must be the same in steady state operation (in order to achieve the stability of the DC bus voltage), a script-based analysis of the behavior of PWM strategies in steady-state operating mode can quickly (less than $0.1s$ per operating point and approximately $30s$ for a cartography like those presented in Figure 4.12, Figure 4.13 and Figure 4.14) confirm the results obtained with transient simulations.

Such an analysis allows us to check the impact of all key parameters:

- Independent AC frequencies for both converters ($f_1$ and $f_2$).
- Independent power factors for both converters (in this study, for converter 1, a unity power factor is assumed to be reached but this parameter could be easily modified).
- Delayed carriers between these two converters.

The only parameter that has to be initialized at the beginning of the analysis is the $v_{dc}$ reference. Thus, if voltage drop across grid side inductors is neglected, it gives:

$$m_1 = \frac{2V_{smax}}{v_{dc}} \tag{4.16}$$

Where $\mathrm{V_{smax}}$ represents the amplitude of grid voltages (325 V in this study).

Finally, indexes $m_1$ and $m_2$ applied to PWM controllers (of both converters) are linked by the following equation:

$$m_1 I_{1max} \cos \varphi_1 = m_1 I_{1max} = m_2 I_{2max} \cos \varphi_2 \tag{4.17}$$

Thus, for a given $\varphi_2$ phase shift, the amplitude of grid currents in rotor windings of the DFIG are linked. As a consequence, the characterization of DC link capacitor RMS current for cascaded converters is similar to the one applied to a single converter (except a new degree of freedom which is the delay introduced between carriers for both converters) (see Figure 4.9).

**Remark**. On the grid side, $\varphi_1$ is equal to zero in this study but if a static reactive power compensation is needed, it could be modified as needed. In such a case, the current in the DC-link capacitor is significantly increased but the dependence on interleaving remains.

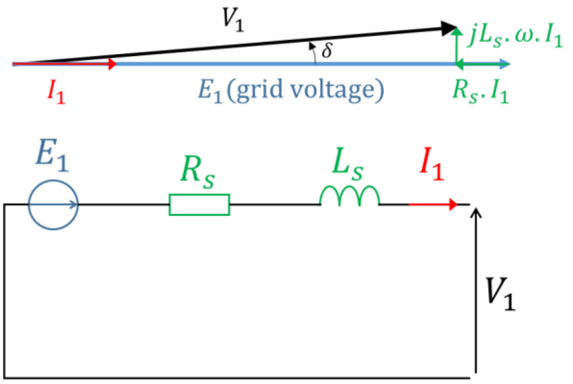

If voltage across the impedance $R_s + j\omega.L_s$ can be neglected:
$E_1 \approx V_1$ or $(\delta \approx 0)$.
Thus

$$m_1 = \frac{2V_1}{V_{dc}} \approx \frac{2E_1}{V_{dc}}$$

Where $E_1$ is the amplitude of phase to neutral voltages.

*Figure 4.9: Grid voltages vector diagram.*

## 4.4 Global structure

### 4.4.1 Description

The analysis of the DC capacitor stress with both PWM strategies is performed with two back-to-back converters as shown in Figure 4.1. A classical application of such a topology is the control of a Doubly-Fed Induction Generator. However, in order to simplify the simulation model (implemented in Matlab/Simulink), one converter (converter 2) is connected to a simple (balanced) three-phase RL load. All parameters of this system are summarized in Table 4.1.

| *Parameter* | *Value* |
|---|---|
| *Switching frequency* | 10 $kHz$ |
| *Grid 1 frequency* | 50 $Hz$ |
| *Grid 1 voltage (L-N)* | 230 $V$ |
| *Grid 1 inductances* | 1 $mH$ |
| *Grid 1 resistances* | 1 $m\Omega$ |
| *DC bus voltage reference* | *722 V* |
| *Load inductance* | *10 mH* |

| | |
|---|---|
| *Load resistance* | $35\ m\Omega$ |
| *Load frequency* | $0\text{–}15\ Hz$ |

*Table 4.1: System parameters.*

The control of converter 1 is based on an inner $dq$-current loop included in a DC voltage regulation loop allowing us to maintain the DC bus voltage to a constant reference (722 V). During all simulations, this voltage is initially regulated before the activation of converter 2.

Then, the output current of converter 2 is regulated in a $dq$-reference frame with different references from 1 to 10 Amperes, requiring a variation of the modulation index in a wide linear range (from 0 to 1).

### 4.4.2 Validation waveforms

The satisfactory operation of the system can be checked with two key indicators (see Figure 4.10):

- Regulation of DC bus voltage.
- AC output currents (converter 2).

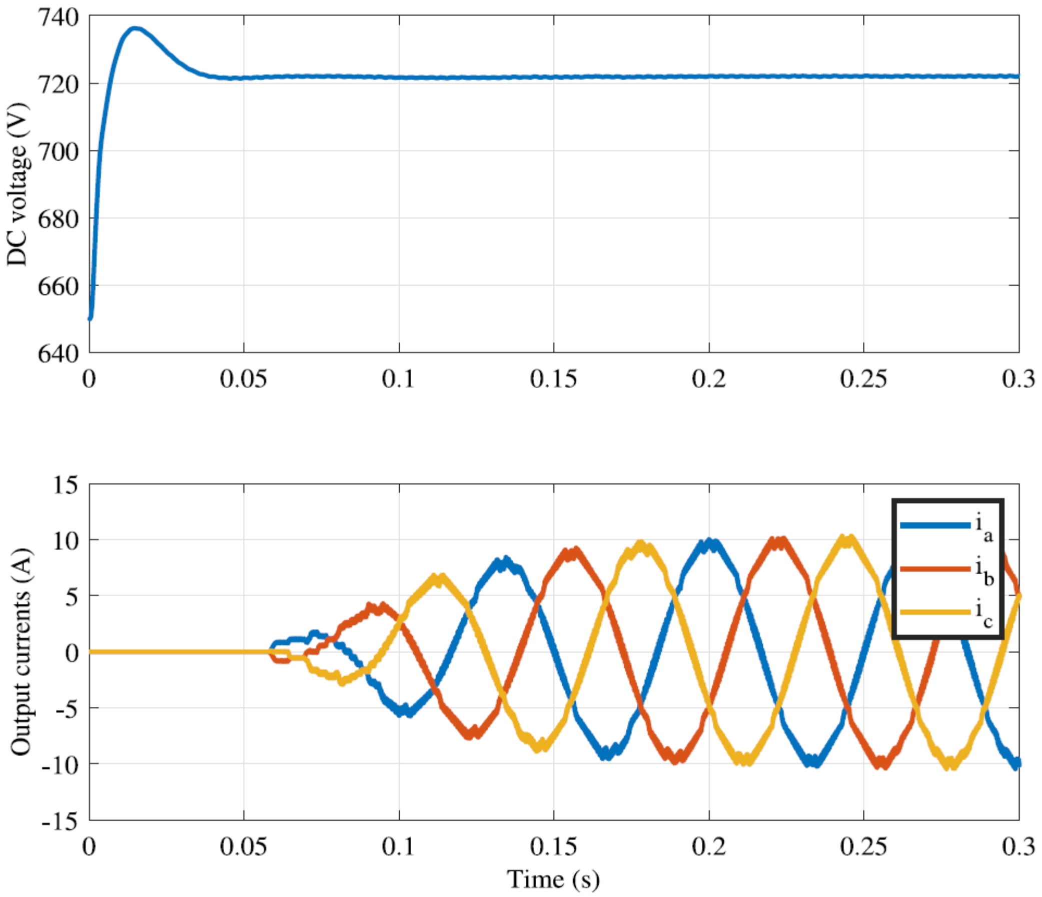

*Figure 4.10: Single simulation: DC link voltage and AC output currents waveforms.*

This figure also shows that steady state operation is reached in less than 0.3 s (which is the duration of all transient simulations). Since this study is performed with two different strategies on an extensive amount of operating points (see Table 4.2 : shift rates between carriers applied to PWM controllers of converters 1 and 2, output current references with different amplitudes and frequencies), all scripted simulations must be verified by checking these two indicators which guarantee the stability of regulations in all cases.

| *Parameter* | *Range* |
|---|---|
| *Shift rate (%)* | *[0; 90] - step: 10%* |
| *d-axis current reference (conv. 2 output) - Amperes* | *[1; 10] - step: 1 A* |
| *Output frequency* $f_2$ | *0; 5; 10; 15 Hz* |

*Table 4.2: Tuning ranges of key parameters.*

## 4.5 Interleaving effect and comparison of PWM strategies

### 4.5.1 Interleaving time factor

This section is going to study the impact of interleaving time on the behavior of the DC-link current. The PWM strategies are interleaved when an interleaving time (delay time) is injected between the PWMs' inputs carriers (see Figure 4.11). This delay $\Delta t$ (in $[s]$) is varying from 0 up to $T_{PWM}$ (i.e. the shift rate percentage varies from 0 to 90% in our case as depicted in Table 4.2). $T_{PWM}$ represents the carrier period of PWM strategy.

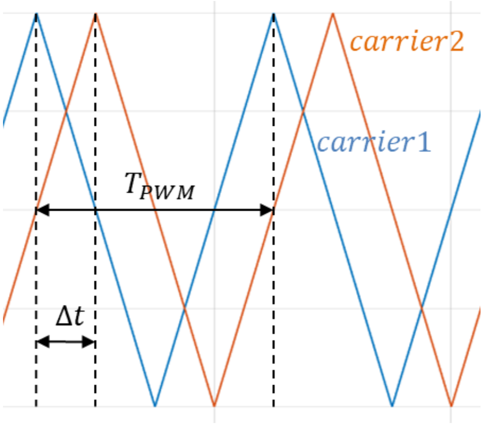

*Figure 4.11: Definition of interleaving time.*

### 4.5.2 Simulation results

In Figure 4.12, it can be seen that the interleaving (for SVPWM) has an effect essentially at high modulation indexes applied to converter 2 (linked to the output current reference) when the output frequency $f_2 = 0Hz$. Moreover, the "intuitive" optimal shift rate of 50% can be verified for all modulation indexes.

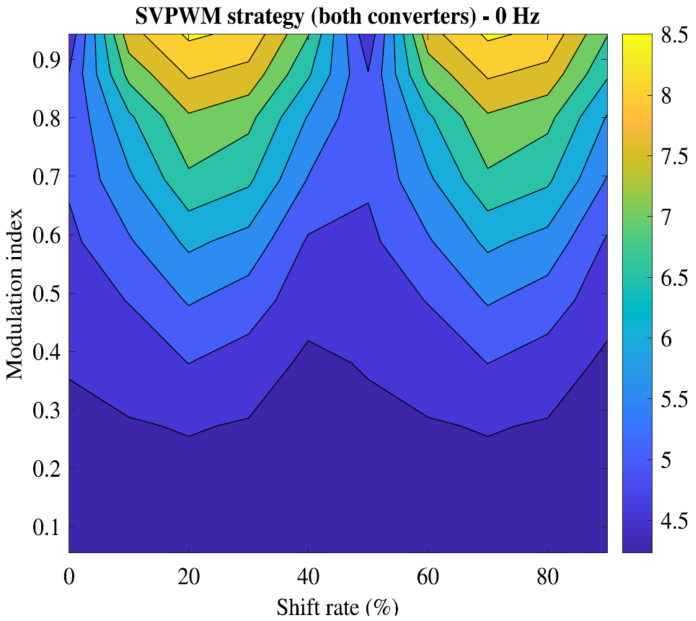

*Figure 4.12: Interleaving effect on the RMS capacitor current for a SVPWM strategy when $f_2 = 0Hz$.*

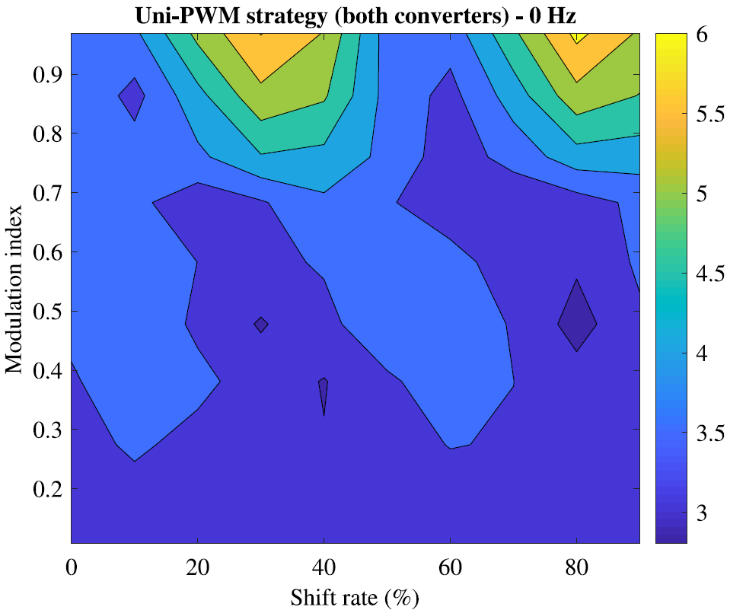

*Figure 4.13: Interleaving effect on the RMS capacitor current for a Uni-DCPWM strategy when $f_2 = 0\ Hz$.*

In Figure 4.13, this result is presented for the same operating conditions with the Uni-DCPWM strategy. And, in this case, we can notice that the RMS current in the DC link capacitor is lower than the case of SVPWM strategy. However, it seems that the optimal shift rate is slightly higher than 50%, and it should probably be adapted to the modulation index. This result is coherent with the one obtained in the case of a single inverter.

This comparison is illustrated in Figure 4.14 by presenting the ratio of RMS currents (Uni-DCPWM/SVPWM) in both cases for all operating points. If this ratio is greater than 1, then the Uni-DCPWM is less efficient than the SVPWM. Thus, it can be noted that it is never the case for any observed operating points.

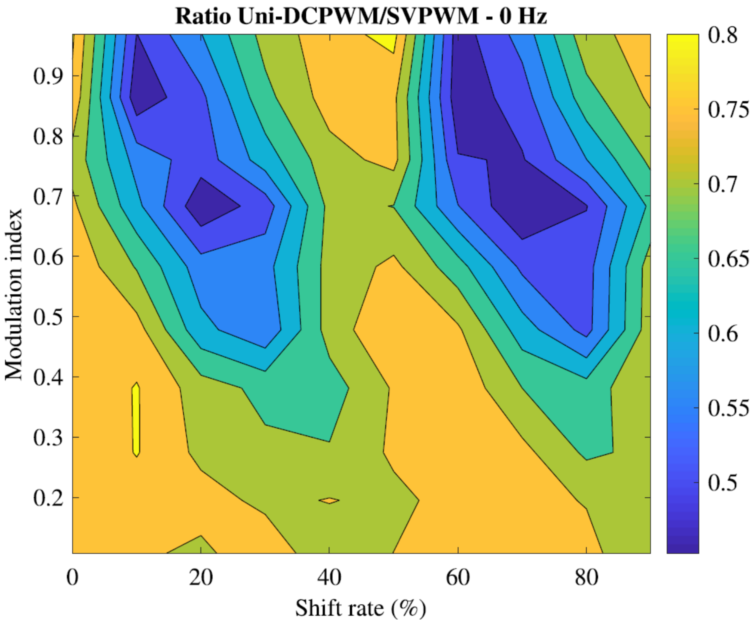

*Figure 4.14: Comparison between Uni-DCPWM and SVPWM strategies when* $f_2 = 0\ Hz$.

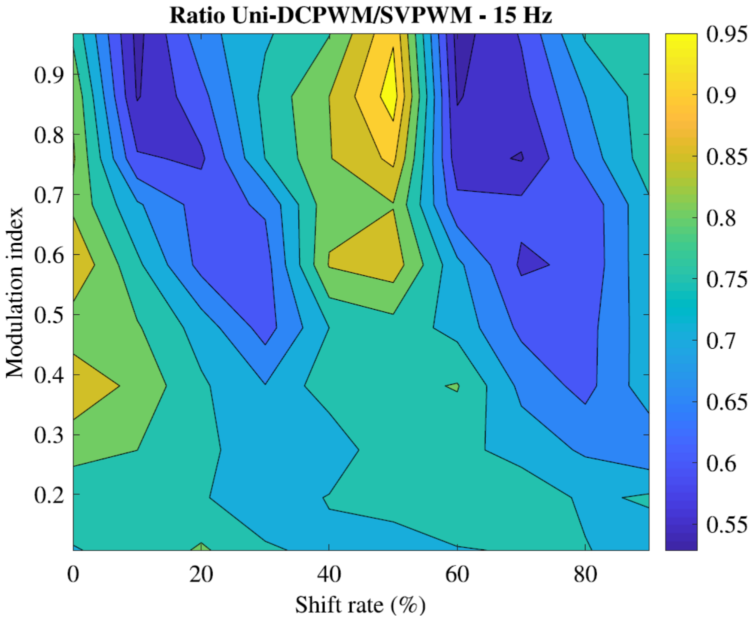

*Figure 4.15: Comparison between Uni-DCPWM and SVPWM strategies @* $f_2 = 15\ Hz$.

The same result can be observed in Figure 4.15 when the output frequency $f_2 = 15Hz$. Other simulations at other frequencies (5 and 10 Hz, not presented) have also led to the same result.

It should be noted that the gain at 15 Hz is lower than the gain at 0 Hz. Moreover, it can be seen in Figure 4.14 that the optimal shift rate (applied to the Uni-DCPWM) is not 50% and must vary according the operating point (i.e.modulation index).

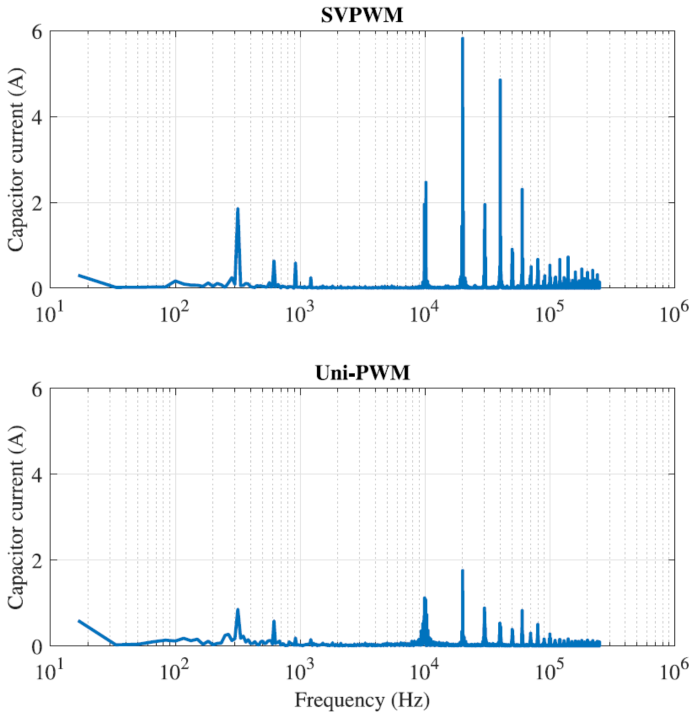

*Figure 4.16: Comparison of capacitor currents spectra in both cases.*

Finally, in Figure 4.16, the capacitor current spectra for SVPWM and Uni-DCPWM show that the interleaving does not clearly increase the apparent frequency of the current on DC side. Indeed, significant harmonic components appear around the switching frequency (10 kHz) even if the most significant terms of the spectrum are located at 20 kHz. This result is quite similar to the one obtained with a single converter, and in such a situation, the most valuable capacitor technology remains the aluminum electrolytic one.

## 4.6 Real-time interleaving control and Tracking algorithm

### 4.6.1 Preliminary analysis

Since the impact of the interleaving of carriers is proved for both strategies and as it is shown the best performance for RMS DC link capacitor current is achieved with the Uni-DCPWM technique, it is clear that an adapted real-time control is required. Indeed, with this PWM strategy, as it is shown in Figure 4.13, the interleaving rate needs to be dynamically tuned when the operating point is modified for achieving optimal results.

However, this closed-loop control cannot be based on a classical reference-based controller because the objective is a minimization of the RMS current in the DC link capacitor and not a regulation at a given value. Thus, a good choice for this purpose is to use a tracking technique similar to the one used in Maximum Power Point Tracking (MPPT) strategies applied to photovoltaic converters as in [106].

### 4.6.2 Structure and start-up sequence

The global structure of the controller used for both converters is presented in Figure 4.17.

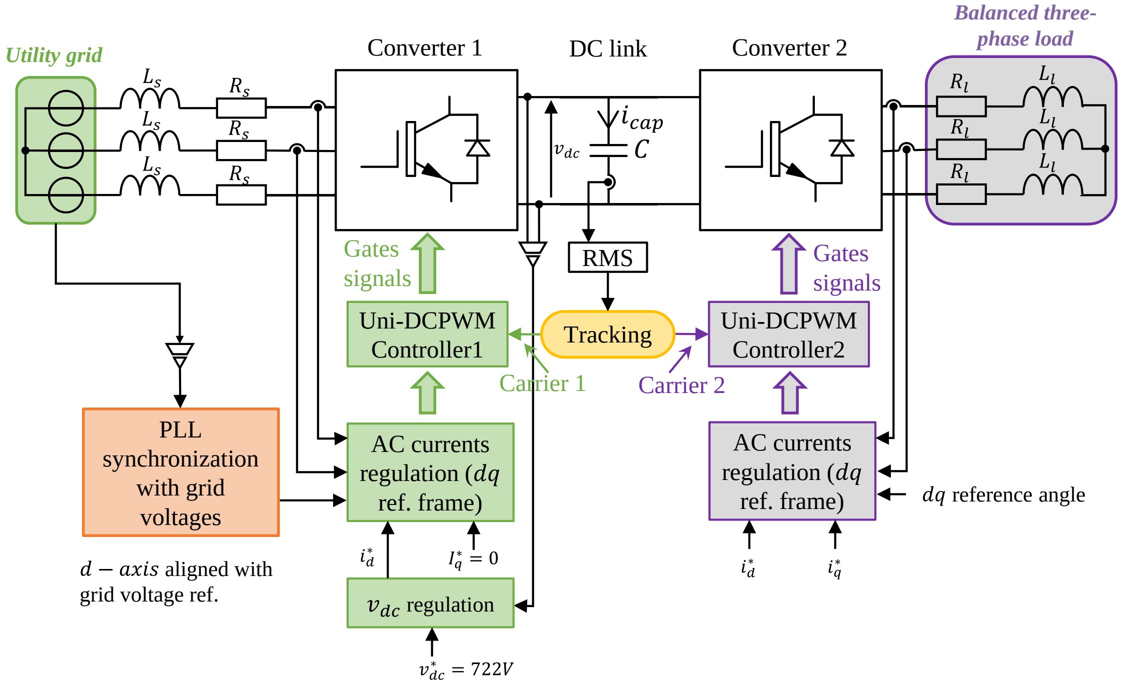

*Figure 4.17: Global control scheme.*

The key element studied here is the "tracking block". However, in order to obtain a proper behavior of the whole system, the following start-up sequence is necessary (a flowchart is presented in Figure 4.18):

1. Activation of the converter 1 (converter 2 is inhibited) with its dedicated control loops in order to reach the DC link voltage reference (720 V here).
2. When the DC bus voltage reference is reached, converter 2 is activated with an initial interleaving rate equal to 50%. Simultaneously, the associated AC currents control loop is activated with given $dq$ references.

3. Then, the tracking algorithm is used in order to reach the minimal RMS current in the DC link capacitor.

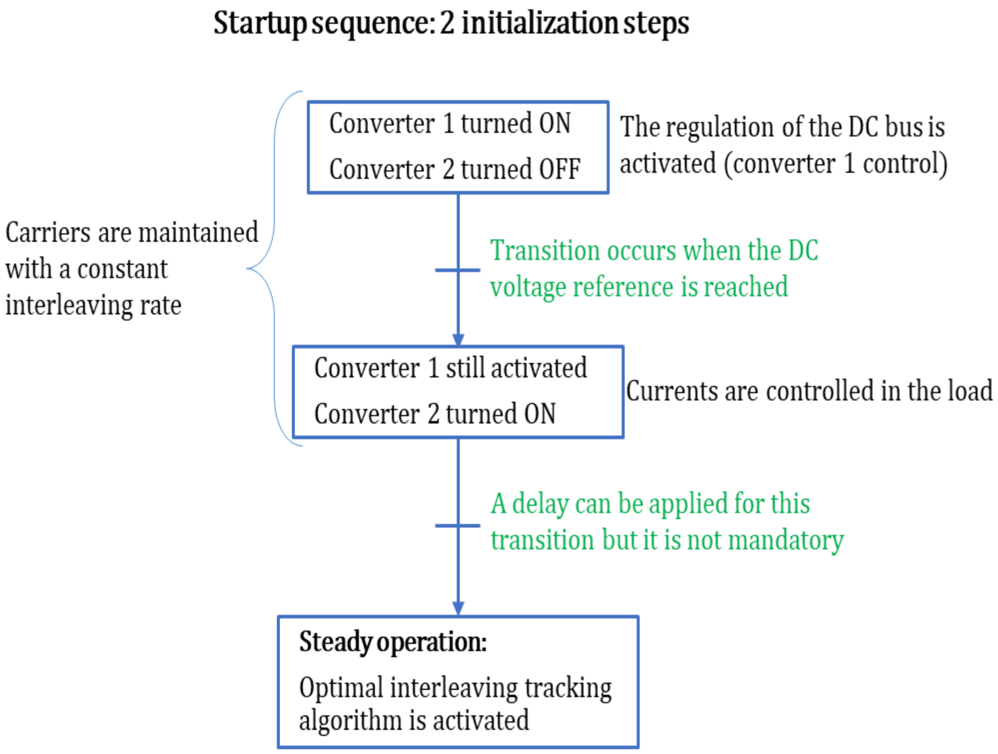

*Figure 4.18: Startup flowchart.*

Since the RMS current is measured with a first order low pass filter having a cut-off frequency equal to 200 $Hz$, its time constant is lower than 1 $ms$. As a consequence, a sampling period of 1 $ms$ can be used for the reconfiguration of the interleaving rate resulting in a significant evolution of the estimated RMS current (ICRMS).

Then, the sensitivity of this current according to the interleaving rate (ILR) which is observed in the cartography of Figure 4.12, the variation step used in the controller is equal to 2%. The algorithm applied in this study can be illustrated by the flowchart shown in Figure 4.19.

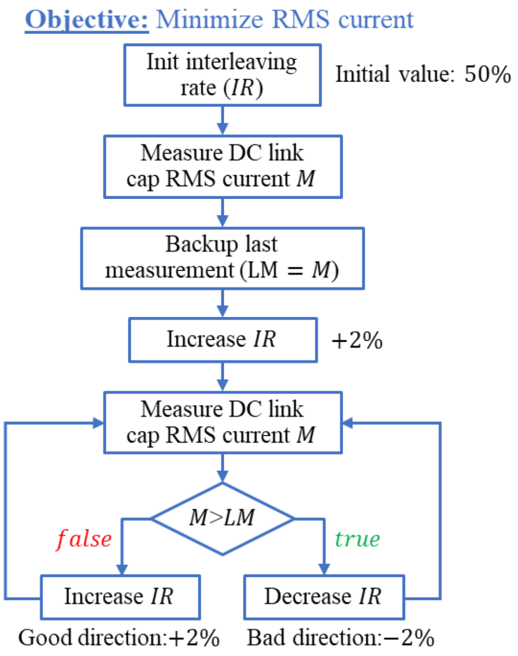

*Figure 4.19: Optimal interleaving tracking algorithm.*

### 4.6.3 Simulation results

Simulations have been performed using the methodology detailed in the previous paragraph. The obtained results are presented in Figure 4.20.

In this simulation, we can see that the DC bus voltage is pre-loaded at 650 V. This result can be obtained in practice when the gate signals are inhibited since converter 1 operates as a three-phase full-bridge diode rectifier. The associated controller (activated at $t = 0s$) allows us to reach the voltage reference and, as a consequence, converter 2 is activated at $10\ ms$ with a ramp signal applied to the $i_d$ current reference (reaching a steady-state value equal to $10\ A$ at $t = 30\ ms$). The actual currents (their amplitude) reach this value $10\ ms$ later.

Finally, the algorithm dedicated to the tracking of the optimal interleaving rate is started @ $50\ ms$ as we can see in Figure 4.20: before this instant, the interleaving rate is constant (50%) and then, variations can be observed with a "steady-state" after $t = 100ms$. It can be seen that the optimal interleaving rate found by the algorithm is greater than 50% (more precisely between 66 and 68%). Finally, from $t = 0.05$s to $0.12s$, the RMS current in the DC-link capacitor can be seen in Figure 4.21.

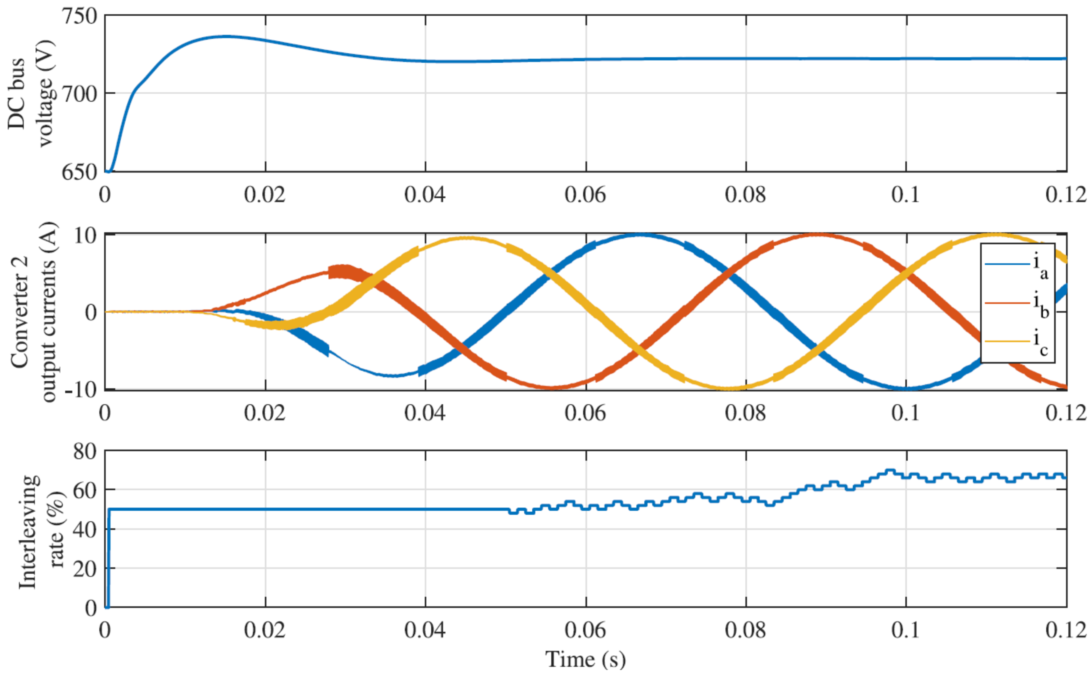

*Figure 4.20: Dynamic interleaving tuning.*

Even if this kind of control scheme does not give a quick response, it should be noted that the aim of this tracking is to limit losses in the DC link capacitors. More precisely, it is well known that the aluminum electrolytic capacitors are very sensitive to their internal temperature, which plays a direct role in their lifetime. Thus, the minimization of the instantaneous RMS current is not as crucial as its minimization on a large time span and within this context, a convergence in few tenths of milliseconds is perfectly satisfying in comparison with the thermal time constant of several hundreds of seconds even for small capacitors [107], [108].

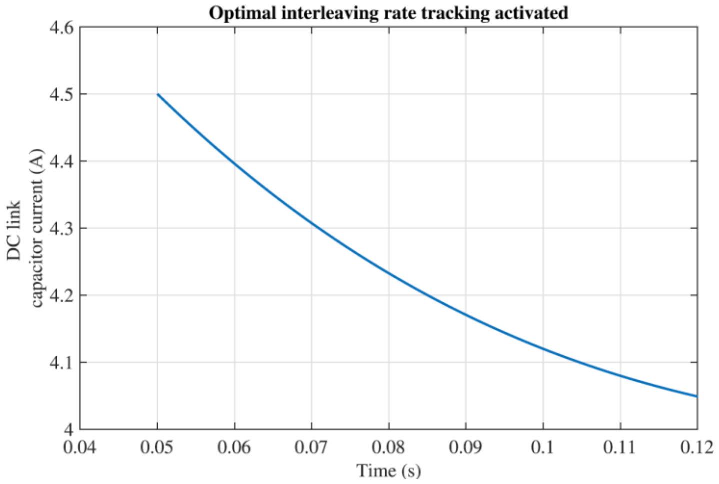

*Figure 4.21: Reduction of the capacitor RMS current due to the optimal interleaving rate tracking.*

As it can be seen in Figure 4.22, the capacitor current waveform is significantly modified by the operating point (including the interleaving rate) with three different configurations. More particularly, it can be noticed that, even the interleaving allows to reduce the RMS value of currents, peak value can be very high due to narrow spikes as it can be seen for the third operating point presented in this figure (for a modulation index $m_2 = 1$, an output frequency $f_2 = 10Hz$ and with an output phase shift angle $\varphi_2 = 0\ rad$).

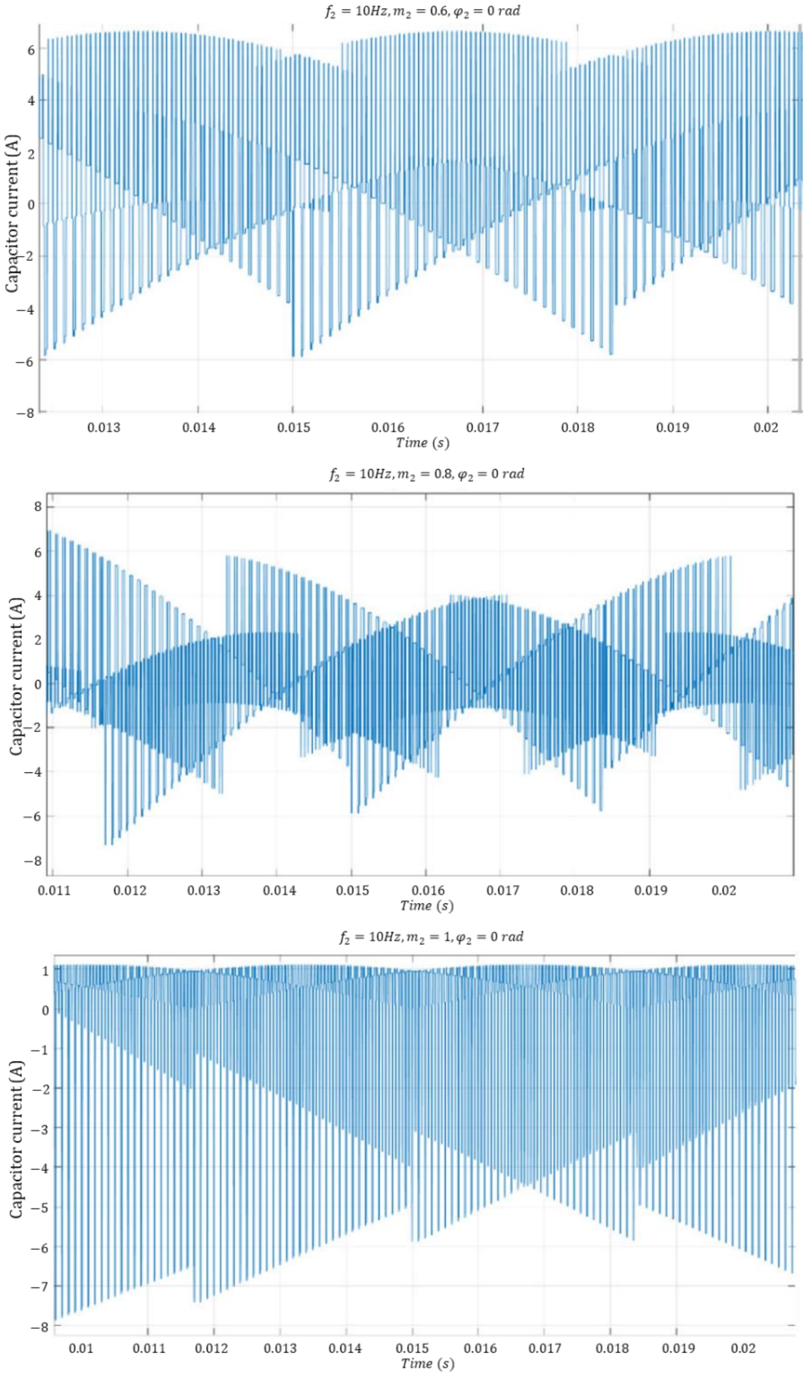

*Figure 4.22: Instantaneous capacitor current waveforms (for three different operating points).*

## 4.7 Conclusion

This chapter showed that the use of two interleaved PWM controllers is of great interest in the context of two back-to-back converters, because it can significantly reduce the RMS current in the DC link capacitor, especially at high (output - i.e. converter 2) modulation index. Moreover, it seems that the Uni-DCPWM strategy is the most adapted strategy within the context of a converter connected to the rotor of a DFIG with a limited range ($\pm 30\%$) around the synchronous speed (corresponding to $\pm 15Hz$ if the grid frequency is equal to $50\ Hz$). For a larger output frequency range, the SVPWM could be more efficient under the condition of a dynamic adaptation of the shift rate between carriers. Therefore, a real-time interleaving control is elaborated based on a tracking technique. Its application yields to minimize the losses in the decoupling capacitor(s) and as a consequence, their internal temperature.

# General conclusion and perspectives

In conclusion, it is important to remind that the wind power is one of the fastest-growing renewable energy technologies [109]–[111]. Since countries are increasingly interested in producing electricity from wind power in order to produce clean and sustainable energy. In earlier period, the technology used in Wind Energy Conversion Systems (WECS) was based on SCIG, operating at fixed speed, and directly connected to the utility grid [112]. Currently, the technology is evolving to variable speed WECS that have been used with DFIG connected to two back-to-back converters.

Growing interest in DFIG connected to two back-to-back converters prompted us to study this system and in particular the stress on the decoupling capacitor which represents a weak point of the system.

In this thesis work, the assigned goal is to make a study on a power generation system based on a DFIG. This study allowed us to realize a complete and global modeling of a back-to-back converters system connected to a machine operating at variable speed. We have established a mathematical model of DFIM in the first chapter. In this model, the stator of the machine is directly connected to the grid and the rotor is connected to the grid through static converters. Their operation principle and power transfer between the machine and the grid are presented in the first chapter too.

In order to manipulate the power transfer between the generator and the utility grid, we should be able to control the generator. This was the goal of the second chapter, where the control of RSC is addressed based on the SFO concept that helps to simplify the DFIG model and obtaining a decoupled control of real and reactive stator powers. Also the control of GSC is treated. It includes outer loop that aims to control and stabilize the DC-bus voltage, and inner loop that regulates the $dq$-axis decoupling current components. In the end of this chapter, the control of the machine has been validated by presenting simulation results for super and sub synchronism modes.

Chapter 3 has been dedicated to deal with the issue of static converter. This chapter presents the preliminary basics on the structure and control of a three-phase full bridges converter. Two approaches for the representation of PWM strategies have been introduced (scalar-based and vector based). The concept of zero-sequence component has been presented too.

This is the basis of different PWM strategies proposed in the literature because this component modifies the time distribution of the null vectors and thus modifies the quality of the voltage supplied to the load, the linear zone of the PWM strategy or the switching losses of the converter. Among these PWM strategies, a review of the literature on the SVPWM, GDPWM and Uni-PWM is presented with their principle and algorithm.

Finally, chapter 4 treated the entire system including two back-to-back three-phase full bridges converter, load, closed-loops control scheme and the PWM controller. Both strategies SVPWM and Uni-DCPWM are applied to converters besides introducing the interleaving time value between the PWM strategies controlling both converters. It has been demonstrated that this interleaving time has a great impact on the value of the decoupling capacitor current. The best or the most advantageous value of the interleaving time is $0.5 * T_{PWM}$ (50 %) when SVPWM is used. While the optimal shift rate applied to the Uni-DCPWM is not 50 % and must vary according the operating point. And it should probably be adapted to the modulation index. Also, it is clear that there is an improvement on the RMS current reduction when Uni-DCPWM is used compared to the use of SVPWM with a limited range ($\pm 30\%$) around the synchronous speed. In addition, a dynamic adaptation of the shift rate and a real-time control has been elaborated based on a tracking technique with the aim of minimizing the RMS current in the decoupling capacitor and as a consequence, their internal temperature which leads increasing the lifetime.

With regard to future perspectives, the door is open for discussion and any suggestion but we mention some perspectives that might be important to be treated. Among these perspectives, it may be interesting to implement other robust commands for the DFIG and make a comparison between them. Also, as we have seen in this thesis, both converters (RSC and GSC) are controlled by same strategy in same time (SVPWM or Uni-DCPWM). Therefore, applying different strategies for both converters in same time can be a good idea, for example the first converter is controlled by SVPWM while the second one is controlled by Uni-DCPWM and vice versa. Moreover, it may be good applying other PWM methods evoked in literature (such as GDPWM) to see if we can obtain a better optimization of stress reduction on the bus by mitigating thermal cycling under variable operating point of the DFIG. Finally, since circumstances did not permit to validate the simulation results, it is important to realize a test bench in order to verify the simulation results experimentally.

# Appendix A

## Mathematical transformation

The mathematical transformations (Concordia, Clarke and Park) are used with the aim to facilitate and simplify the model, also they allow us to control the system easily by decoupling the real and reactive stator power as we will see later.

### 1. Three-phase – two-phase transformation

The objective of using this transition is to pass from a three-phase system $abc$ to a diphase system $\alpha\beta$ in order to simplify the model (see Figure A.1), where we reduce the system from three equations to two equations. There are primarily two transformations: Clarke and Concordia.

Clarke's transformation preserves the degree of amplitude, but not the power nor the torque (a 3/2 coefficient must be multiplied). While that of Concordia, which is normalized, it keeps the power without changing but not the amplitudes.

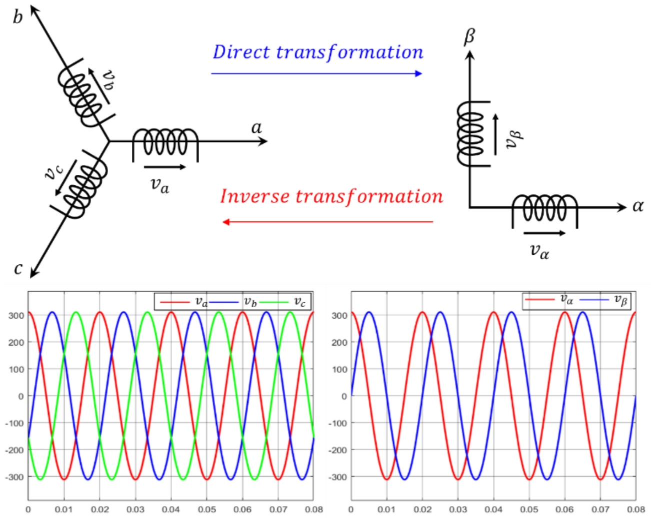

*Figure A.1: Clarke transformation.*

### a. Concordia transformation

The Transition from a three-phase $abc$ system to a dual-phase $\alpha\beta$ system (i.e. direct transformation) is obtained via:

$$\begin{bmatrix} x_a \\ x_b \\ x_c \end{bmatrix} \xrightarrow{T_{23}} \begin{bmatrix} x_\alpha \\ x_\beta \end{bmatrix} \Leftrightarrow [x_{\alpha\beta}] = T_{23}[x_{abc}] \qquad \text{(A.1)}$$

Where $T_{23} = \sqrt{\frac{3}{2}}\begin{bmatrix} 1 & -\frac{1}{2} & -\frac{1}{2} \\ 0 & \frac{\sqrt{3}}{2} & -\frac{\sqrt{3}}{2} \end{bmatrix}$.

While the inverse transformation which means the transition from a dual-phase $\alpha\beta$ system to a three-phase $abc$ system is obtained via:

$$\begin{bmatrix} x_\alpha \\ x_\beta \end{bmatrix} \xrightarrow{T_{32}} \begin{bmatrix} x_a \\ x_b \\ x_c \end{bmatrix} \Leftrightarrow [x_{abc}] = T_{32}[x_{\alpha\beta}] \qquad \text{(A.2)}$$

Where $T_{32} = \sqrt{\frac{2}{3}}\begin{bmatrix} 1 & 0 \\ -\frac{1}{2} & \frac{\sqrt{3}}{2} \\ -\frac{1}{2} & -\frac{\sqrt{3}}{2} \end{bmatrix}$.

### b. Clarke transformation

For direct Clarke transformation we use (A.3)

$$\begin{bmatrix} x_a \\ x_b \\ x_c \end{bmatrix} \xrightarrow{C_{23}} \begin{bmatrix} x_\alpha \\ x_\beta \end{bmatrix} \Leftrightarrow [x_{\alpha\beta}] = C_{23}[x_{abc}] \qquad \text{(A.3)}$$

Where $C_{23} = \frac{2}{3}\begin{bmatrix} 1 & -\frac{1}{2} & -\frac{1}{2} \\ 0 & \frac{\sqrt{3}}{2} & -\frac{\sqrt{3}}{2} \end{bmatrix}$.

Equation (A.4) is used to obtain the inverse Clarke Transformation:

$$\begin{bmatrix} x_\alpha \\ x_\beta \end{bmatrix} \xrightarrow{C_{32}} \begin{bmatrix} x_a \\ x_b \\ x_c \end{bmatrix} \Leftrightarrow [x_{abc}] = C_{32}[x_{\alpha\beta}] \qquad \text{(A.4)}$$

Where $C_{32} = \begin{bmatrix} 1 & 0 \\ -\frac{1}{2} & \frac{\sqrt{3}}{2} \\ -\frac{1}{2} & -\frac{\sqrt{3}}{2} \end{bmatrix}$.

## 2. Park transformation

The Park transformation consists of a three-phase - dual-phase transformation followed by a rotation. It allows you to move from the $abc$ frame to the $\alpha\beta$ frame and then to the $dq$ frame. The $\alpha\beta$ reference is always fixed in relation to the $abc$ reference (Figure A.2), but the $dq$ reference is rotating. It forms an angle with the fixed frame $\alpha\beta$ which is called the Park transformation angle or Park angle $\theta$.

### a. Direct transformation

$$\begin{bmatrix} x_\alpha \\ x_\beta \end{bmatrix} \xrightarrow{P(\theta)} [x_{dq}] \Leftrightarrow [x_{dq}] = P(\theta)[x_{\alpha\beta}] \qquad \textit{(0A.5)}$$

Where $P(\theta) = \begin{bmatrix} \cos\theta & -\sin\theta \\ \sin\theta & \cos\theta \end{bmatrix}$.

### a. Inverse Transformation:

$$[x_{dq}] \xrightarrow{P(-\theta)} \begin{bmatrix} x_\alpha \\ x_\beta \end{bmatrix} \Leftrightarrow [x_{\alpha\beta}] = P(-\theta)[x_{dq}] \qquad \textit{(A.6)}$$

Where $P(-\theta) = \begin{bmatrix} \cos\theta & \sin\theta \\ -\sin\theta & \cos\theta \end{bmatrix}$.

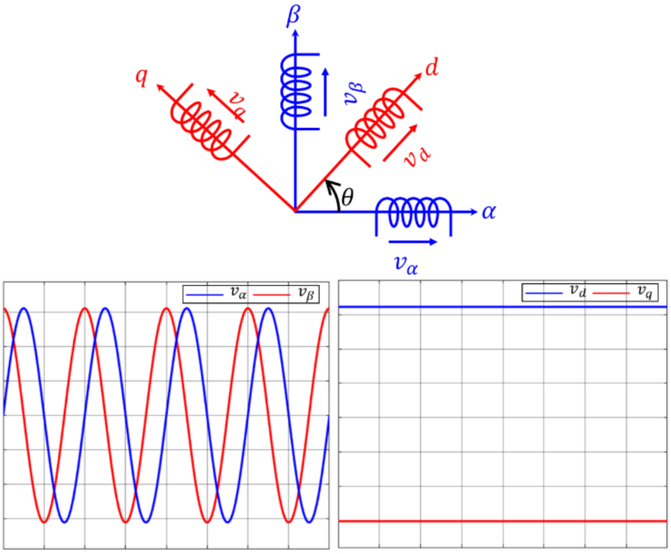

*Figure A.2: Park transformation.*

# Appendix B

The DFIM parameters are shown in the following table [113]:

| **Parameter** | **Value** |
|---|---|
| Stator resistance $R_s$ | 1.77 Ω |
| Rotor resistance $R_r$ | 0.44 Ω |
| Stator cyclic self-inductance $L_s$ | 0.309 H |
| Rotor cyclic self-inductance $L_r$ | 0.035 H |
| Cyclic mutual inductance $M$ | 0.103 $H$ |
| Moment of inertia $J$ | 0.021 $Kg.m^2$ |
| Friction coefficient $f$ | 0.004 $N.m/s$ |
| Stator nominal voltage $V_{sn}$(V) | 220 |
| Rotor nominal voltage $V_{rn}$(V) | 80 |
| Number of pair per pole $p$ | 2 |

*Table B.1: Parameters of the DFIM.*

# Appendix C

## Computing the duration for applying each vector during the decoupling period:

In order to find the values of $t_i$ and $t_{i+1}$ which represent the times when the vectors $\overrightarrow{V_i}$ and $\overrightarrow{V_{i+1}}$ are applied in vector based implementation, we have to solve the following system of two equations which is done in (3.37).

$$\begin{cases} T_d \cdot m \cdot \cos\theta = \frac{2}{3} \cdot t_i \cdot \cos\gamma_i + \frac{2}{3} \cdot t_{i+1} \cdot \cos\gamma_{i+1} \\ T_d \cdot m \cdot \sin\theta = \frac{2}{3} \cdot t_i \cdot \sin\gamma_i + \frac{2}{3} \cdot t_{i+1} \cdot \sin\gamma_{i+1} \end{cases} \tag{C.1}$$

By multiplying the first and the second equation of (C.1) by $(\sin\gamma_{i+1})$ and $(-\cos\gamma_{i+1})$ respectively, we get:

$$\begin{cases} T_d \cdot m \cdot \cos\theta \cdot \sin\gamma_{i+1} = \frac{2}{3} \cdot t_i \cdot \cos\gamma_i \cdot \sin\gamma_{i+1} + \frac{2}{3} \cdot t_{i+1} \cdot \cos\gamma_{i+1} \cdot \sin\gamma_{i+1} \\ -T_d \cdot m \cdot \sin\theta \cdot \cos\gamma_{i+1} = -\frac{2}{3} \cdot t_i \cdot \sin\gamma_i \cdot \cos\gamma_{i+1} - \frac{2}{3} \cdot t_{i+1} \cdot \sin\gamma_{i+1} \cdot \cos\gamma_{i+1} \end{cases} \tag{C.2}$$

If we add the equations which are obtained in (C.2), we get an equation with one unknown as follows:

$$\begin{aligned} &T_d \cdot m \cdot (\sin\gamma_{i+1} \cdot \cos\theta - \sin\theta \cdot \cos\gamma_{i+1}) \\ &\qquad = \frac{2}{3} \cdot t_i \cdot (\sin\gamma_{i+1} \cdot \cos\gamma_i - \cos\gamma_{i+1} \cdot \sin\gamma_i) \end{aligned} \tag{C.3}$$

And then,

$$T_d \cdot m \cdot \sin(\gamma_{i+1} - \theta) = \frac{2}{3} \cdot t_i \cdot \sin(\gamma_{i+1} - \gamma_i) \tag{C.4}$$

$$T_d \cdot m \cdot \sin(\gamma_{i+1} - \theta) = \frac{2}{3} \cdot t_i \cdot \sin\left(\frac{\pi}{3}\right) \tag{C.5}$$

Finally we find the value of $t_i$ as described in (C.6).

$$t_i = \sqrt{3} \cdot T_d \cdot m \cdot \sin(\gamma_{i+1} - \theta) \tag{C.6}$$

To find $t_{i+1}$, we repeat the same steps. But this time, by multiplying the first and the second equation of (C.1) by $(-\sin\gamma_i)$ and $(\cos\gamma_i)$ respectively, so we have:

$$\begin{cases} -T_d \cdot m \cdot \cos\theta \cdot \sin\gamma_i = -\frac{2}{3} \cdot t_i \cdot \cos\gamma_i \cdot \sin\gamma_i - \frac{2}{3} \cdot t_{i+1} \cdot \cos\gamma_{i+1} \cdot \sin\gamma_i \\ T_d \cdot m \cdot \sin\theta \cdot \cos\gamma_i = \frac{2}{3} \cdot t_i \cdot \sin\gamma_i \cdot \cos\gamma_i + \frac{2}{3} \cdot t_{i+1} \cdot \sin\gamma_{i+1} \cdot \cos\gamma_i \end{cases} \tag{C.7}$$

The adding of these two equations give us:

$$\begin{aligned} &T_d \cdot m \cdot (\sin\theta \cdot \cos\gamma_i - \cos\theta \cdot \sin\gamma_i) \\ &\qquad = \frac{2}{3} \cdot t_{i+1} \cdot (\sin\gamma_{i+1} \cdot \cos\gamma_i - \cos\gamma_{i+1} \cdot \sin\gamma_i) \end{aligned} \tag{C.8}$$

And then,

$$T_d \cdot m \cdot \sin(\theta - \gamma_i) = \frac{2}{3} \cdot t_{i+1} \cdot \sin(\gamma_{i+1} - \gamma_i) \tag{C.9}$$

$$T_d \cdot m \cdot \sin(\theta - \gamma_i) = \frac{2}{3} \cdot t_{i+1} \cdot \sin\left(\frac{\pi}{3}\right) \tag{C.10}$$

Finally we find the value of $t_{i+1}$ as described in (C.6).

$$t_{i+1} = \sqrt{3} \cdot T_d \cdot m \cdot \sin(\theta - \gamma_i) \tag{C.11}$$

# Appendix D

## Different PWM strategies

### 1- THIPWM

In order to improve and to extend the linearity rang of PWM strategies, several investigations have been carried out [114]. By adding a zero-voltage component with a frequency three times greater than the fundamental as following:

$$v_{n0} = A \cdot \cos(3\omega t + \theta_0) \tag{D.1}$$

It is possible to extend the linear zone of the SPWM strategy by choosing the right value of $A$. It has been demonstrated that the optimum in terms of linearity is obtained with $A = \frac{1}{6}$ [114], this strategy is called THIPWM6. With the value of $A = \frac{1}{4}$, this strategy, called THIPWM4, it minimizes the voltage harmonics supplied to the load.

The limit value of the linearity zone for these two strategies are:

- $m = \frac{2}{\sqrt{3}} = 1.1547$ for THIPWM.
- $m = \frac{36}{7\sqrt{21}} = 1.1223$ for THIPWM.

### 2- DPWM

Some studies focussed on the switching or conduction losses reduction like [85], [100], among these studies various DPWM strategies have been investigated such as DPWM0, DPWM1, DPWM2, DPWMMAX, DPWMMIN and GDPWM. These methods use modulating signals $mod_x$ that are the results of adding the zero-sequence voltage $v_{n0}$ to the reference voltage $v_x^*$, and each method has a specific function for $v_{n0}$ as follows:

- DPWM0, DPWM1, DPWM2: $v_{n0} = sign(V_{max}) \cdot \frac{v_{dc}}{2} - V_{max}$. Where $V_{max}$ is the voltage resulting from the maximum amplitude test $|V_{max}| = \max(|v_1^*|, |v_2^*|, |v_3^*|)$, (absolute maximum of the three reference voltages, after translation by an angle $\psi$ )
    - $\psi = 0°$ for DPWM0
    - $\psi = 30°$ for DPWM1

  - $\psi = 60°$ for DPWM2
- DPWM3: $v_{n0} = sign(V_{medium}) \cdot \frac{v_{dc}}{2} - V_{medium}$, where $V_{medium}$ is the intermediate value between the reference voltages $(v_1^*, v_2^*, v_3^*)$.
- DPWMMAX: $v_{n0} = \frac{v_{dc}}{2} - V_{max}$, or $V_{max} = \max(v_1^*, v_2^*, v_3^*)$.
- DPWMMIN : $v_{n0} = -\frac{v_{dc}}{2} - V_{min}$, or $V_{min} = \min(v_1^*, v_2^*, v_3^*)$.

# References

[1] "Turbines asynchrones ou synchrones." [Online]. Available: http://www.journal-eolien.org/tout-sur-l-eolien/les-principales-technologies-eoliennes/.

[2] IRENA, "Global energy transformation: A roadmap to 2050," Abu Dhabi, 2019.

[3] T. Ghennam, "Supervision d'une ferme éolienne pour son intégration dans la gestion d'un réseau électrique, Apports des convertisseurs multi niveaux au réglage des éoliennes à base de machine asynchrone à double alimentation," 2011.

[4] H. Bennani, "Machine asynchrone à double alimentation: Les lois de commande en régime permanent," 2011.

[5] T. D. Nguyen, N. Patin, and G. Friedrich, "Extended double carrier PWM strategy dedicated to RMS current reduction in DC link capacitors of three-phase inverters," *IEEE Trans. Power Electron.*, vol. 29, no. 1, pp. 396–406, 2014.

[6] J. HOBRAICHE, "Comparaison des stratégies de modulation à largeur d'impulsions triphasées–Application à l'alterno-démarreur," *Univ. Technol. Compiègne*, 2005.

[7] G. Oriti, A. L. Julian, and T. A. Lipo, "A new space vector modulation strategy for common mode voltage reduction [in PWM invertors]," in *PESC97. Record 28th Annual IEEE Power Electronics Specialists Conference. Formerly Power Conditioning Specialists Conference 1970-71. Power Processing and Electronic Specialists Conference 1972*, 1997, vol. 2, pp. 1541–1546.

[8] W. JOHANN, "Minimizing the Current Harmonics RMS Value of Three-Phase PWM Converter Systems by Optimal and Suboptimal Transition Between Continuous and Disconinuous Modulation," 1991.

[9] O. Ojo, "The generalized discontinuous PWM scheme for three-phase voltage source inverters," *IEEE Trans. Ind. Electron.*, vol. 51, no. 6, pp. 1280–1289, 2004.

[10] K. S. Gowri, T. B. Reddy, and C. S. Babu, "A novel high performance Generalized Discontinuous PWM algorithm for reduced current ripple and switching losses using

imaginary switching times," in *TENCON 2008-2008 IEEE Region 10 Conference*, 2008, pp. 1–6.

[11] T. D. Nguyen, J. Hobraiche, N. Patin, G. Friedrich, and J.-P. Vilain, "A direct digital technique implementation of general discontinuous pulse width modulation strategy," *IEEE Trans. Ind. Electron.*, vol. 58, no. 9, pp. 4445–4454, 2011.

[12] T. D. Nguyen, N. Patin, and G. Friedrich, "PWM strategy dedicated to the reduction of DC bus capacitor stress in embedded three phase inverter," in *2011 IEEE Vehicle Power and Propulsion Conference*, 2011, pp. 1–6.

[13] N. Rouhana, G. Friedrich, and N. Patin, "Contribution à la réduction des composants passifs dans les convertisseurs électroniques de puissance embarqués Thèse," no. Ea 4297. Compiègne, 2017.

[14] H. Camblong, "Minimisation de l'impact des perturbations d'origine éolienne dans la génération d'électricité par des aérogénérateurs à vitesse variable." Paris, ENSAM, 2003.

[15] O. Zamzoum, Y. El Mourabit, M. Errouha, A. Derouich, and A. El Ghzizal, "Power control of variable speed wind turbine based on doubly fed induction generator using indirect field-oriented control with fuzzy logic controllers for performance optimization," *Energy Sci. Eng.*, vol. 6, no. 5, pp. 408–423, 2018.

[16] T. Wildi and G. Sybille, *électrotechnique*. De Boeck Supérieur, 2000.

[17] F. Poitiers, "Etude et commande de génératrices asynchrones pour l'utilisation de l'énergie éolienne-machine asynchrone a cage autonome-machine asynchrone a double alimentation reliée au réseau." Université de Nantes, 2003.

[18] I. Cadirci and M. Ermiş, "Double-output induction generator operating at subsynchronous and supersynchronous speeds: steady-state performance optimisation and wind-energy recovery," in *IEE Proceedings B (Electric Power Applications)*, 1992, vol. 139, no. 5, pp. 429–442.

[19] E. Monmasson, *Power electronic converters: PWM strategies and current control techniques*. John Wiley & Sons, 2013.

[20] L. Fan and Z. Miao, *Modeling and analysis of doubly fed induction generator wind energy systems*. Academic Press, 2015.

[21] N. Patin, “Analyse d’architectures, modélisation et commmande de générateurs pour réseaux autonomes.” École normale supérieure de Cachan-ENS Cachan, 2007.

[22] J.-P. Caron and J.-P. Hautier, *Modélisation et commande de la machine asynchrone*, vol. 10. Technip Paris, 1995.

[23] G. Tapia and A. Tapia, “Wind generation optimisation algorithm for a doubly fed induction generator,” *IEE Proceedings-Generation, Transm. Distrib.*, vol. 152, no. 2, pp. 253–263, 2005.

[24] L. Jiao, H. Banakar, B. Shen, C. Luo, G. Joos, and B.-T. Ooi, “Fundamental and applied research on doubly-fed induction generator,” in *2005 International Conference on Electrical Machines and Systems*, 2005, vol. 1, pp. 32–37.

[25] J. Soens, J. Driesen, and R. Belmans, “A comprehensive model of a doubly fed induction generator for dynamic simulations and power system studies,” in *Proc. International Conference on Renewable Energies and Power Quality, Vigo, Spain*, 2003.

[26] A. Boyette, S. Saadate, and P. Poure, “Direct and indirect control of a doubly fed induction generator wind turbine including a storage unit,” in *IECON 2006-32nd Annual Conference on IEEE Industrial Electronics*, 2006, pp. 2517–2522.

[27] A. Petersson, *Analysis, modeling and control of doubly-fed induction generators for wind turbines*. Chalmers University of Technology, 2005.

[28] B. Ozpineci and L. M. Tolbert, “Simulink implementation of induction machine model-a modular approach,” in *IEEE International Electric Machines and Drives Conference, 2003. IEMDC’03.*, 2003, vol. 2, pp. 728–734.

[29] G. Salloum, “Contribution à la commande robuste de la machine asynchrone à double alimentation.” Institut National Polytechnique de Toulouse, 2007.

[30] A. Gaillard, “Système éolien basé sur une MADA: contribution à l’étude de la qualité

de l’énergie électrique et de la continuité de service.” Université Henri Poincaré-Nancy 1, 2010.

[31] P. Krafczyk, “Modélisation et mise en oeuvre d’une chaîne de production éolienne à base de la MADA,” *Mémoire présentée pour l’obtention du diplôme d’ingénieur en Electrotech. Cent. d’enseignement Nancy*, vol. 10, 2013.

[32] D. Kairous, R. Wamkeue, and B. Belmadani, “Sliding mode control of DFIG based variable speed WECS with flywheel energy storage,” in *The XIX International Conference on Electrical Machines-ICEM 2010*, 2010, pp. 1–6.

[33] M. Koteich, “Modélisation et observabilité des machines électriques en vue de la commande sans capteur mécanique.” 2016.

[34] M. A. Hannan, J. A. Ali, A. Mohamed, and A. Hussain, “Optimization techniques to enhance the performance of induction motor drives: A review,” *Renew. Sustain. Energy Rev.*, vol. 81, pp. 1611–1626, 2018.

[35] B. Hopfensperger, D. J. Atkinson, and R. A. Lakin, “Stator-flux-oriented control of a doubly-fed induction machine: with and without position encoder,” *IEE Proceedings-Electric power Appl.*, vol. 147, no. 4, pp. 241–250, 2000.

[36] W. Leonhard, *Control of electrical drives*. Springer Science & Business Media, 2001.

[37] S. Wang and Y. Ding, “Stability analysis of field oriented doubly-fed induction machine drive based on computer simulation,” *Electr. Mach. power Syst.*, vol. 21, no. 1, pp. 11–24, 1993.

[38] L. Xu and W. Cheng, “Torque and reactive power control of a doubly fed induction machine by position sensorless scheme,” *IEEE Trans. Ind. Appl.*, vol. 31, no. 3, pp. 636–642, 1995.

[39] L. Morel, H. Godfroid, A. Mirzaian, and J. M. Kauffmann, “Double-fed induction machine: converter optimisation and field oriented control without position sensor,” *IEE Proceedings-Electric Power Appl.*, vol. 145, no. 4, pp. 360–368, 1998.

[40] R. Datta and V. T. Ranganathan, “Decoupled control of active and reactive power for

a grid-connected doubly-fed wound rotor induction machine without position sensors," in *Conference Record of the 1999 IEEE Industry Applications Conference. Thirty-Forth IAS Annual Meeting (Cat. No. 99CH36370)*, 1999, vol. 4, pp. 2623–2630.

[41] S. Golestan, J. M. Guerrero, and J. C. Vasquez, "Three-phase PLLs: A review of recent advances," *IEEE Trans. Power Electron.*, vol. 32, no. 3, pp. 1894–1907, 2016.

[42] J. Ögren, "PLL design for inverter grid connection: Simulations for ideal and non-ideal grid conditions." 2010.

[43] A. Kulkarni and V. John, "Analysis of bandwidth–unit-vector-distortion tradeoff in PLL during abnormal grid conditions," *IEEE Trans. Ind. Electron.*, vol. 60, no. 12, pp. 5820–5829, 2012.

[44] V. Kaura and V. Blasko, "Operation of a phase locked loop system under distorted utility conditions," *IEEE Trans. Ind. Appl.*, vol. 33, no. 1, pp. 58–63, 1997.

[45] L. Harnefors and H.-P. Nee, "A general algorithm for speed and position estimation of AC motors," *IEEE Trans. Ind. Electron.*, vol. 47, no. 1, pp. 77–83, 2000.

[46] M. Rasheduzzaman, S. Khorbotly, and J. W. Kimball, "A modified SRF-PLL for phase and frequency measurement of single-phase systems," in *2016 IEEE Energy Conversion Congress and Exposition (ECCE)*, 2016, pp. 1–7.

[47] S.-K. Chung, "A phase tracking system for three phase utility interface inverters," *IEEE Trans. Power Electron.*, vol. 15, no. 3, pp. 431–438, 2000.

[48] M. Karimi-Ghartemani, "A unifying approach to single-phase synchronous reference frame PLLs," *IEEE Trans. power Electron.*, vol. 28, no. 10, pp. 4550–4556, 2012.

[49] A. Ghoshal and V. John, "Performance evaluation of three phase SRF-PLL and MAF-SRF-PLL," *Turkish J. Electr. Eng. Comput. Sci.*, vol. 23, no. 6, pp. 1781–1804, 2015.

[50] T. M. C. Le, "Couplage Onduleurs Photovoltaïques et Réseau, aspects contrôle/commande et rejet de perturbations." 2012.

[51] S. Muller, M. Deicke, and R. W. De Doncker, “Doubly fed induction generator systems for wind turbines,” *IEEE Ind. Appl. Mag.*, vol. 8, no. 3, pp. 26–33, 2002.

[52] Š. Bucz and A. Kozáková, “PID controller design for specified performance,” *Introd. to PID Control. Theory, Tuning Appl. to Front. areas*, 2012.

[53] J. Crowe *et al.*, *PID control: new identification and design methods*. Springer, 2005.

[54] B. M. Vinagre, C. A. Monje, A. J. Calderón, and J. I. Suárez, “Fractional PID controllers for industry application. A brief introduction,” *J. Vib. Control*, vol. 13, no. 9–10, pp. 1419–1429, 2007.

[55] K. J. Åström and T. Hägglund, “PID control,” *IEEE Control Syst. Mag.*, vol. 1066, no. 033X/06, 2006.

[56] H. M. Boulouiha, A. Allali, and M. Denai, “Grid integration of wind energy systems: control design, stability, and power quality issues,” in *Clean energy for sustainable development*, Elsevier, 2017, pp. 239–335.

[57] L. Buchta and L. Otava, “Adaptive compensation of inverter non-linearities based on the Kalman filter,” in *Industrial Electronics Society, IECON 2016-42nd Annual Conference of the IEEE*, 2016, pp. 4301–4306.

[58] M. Salcone and J. Bond, “Selecting film bus link capacitors for high performance inverter applications,” in *2009 IEEE International Electric Machines and Drives Conference*, 2009, pp. 1692–1699.

[59] T. D. Nguyen, N. Patin, and G. Friedrich, “Etude de stratégies de modulation pour onduleur triphasé dédiées à la réduction des perturbations du bus continu en environnement embarqué,” UTC, Compiègne, 2011.

[60] J. Millman, “A useful network theorem,” *Proc. IRE*, vol. 28, no. 9, pp. 413–417, 1940.

[61] N. Patin, Z. Chmeit, G. Salloum, and R. Mbayed, “Study of interleaved PWM strategies applied to two back-to-back three-phase full bridges,” *Math. Comput. Simul.*, 2020.

[62] R. Pena, J. C. Clare, and G. M. Asher, “Doubly fed induction generator using back-to-back PWM converters and its application to variable-speed wind-energy generation,” *IEE Proceedings-Electric Power Appl.*, vol. 143, no. 3, pp. 231–241, 1996.

[63] J. Hobraiche, J.-P. Vilain, P. Macret, and N. Patin, “A new PWM strategy to reduce the inverter input current ripples,” *IEEE Trans. Power Electron.*, vol. 24, no. 1, pp. 172–180, 2009.

[64] A. M. Hava and N. O. Cetin, “A generalized scalar PWM approach with easy implementation features for three-phase, three-wire voltage-source inverters,” *IEEE Trans. Power Electron.*, vol. 26, no. 5, p. 1385, 2011.

[65] A. M. Hava, R. J. Kerkman, and T. A. Lipo, “Simple analytical and graphical methods for carrier-based PWM-VSI drives,” *IEEE Trans. power Electron.*, vol. 14, no. 1, pp. 49–61, 1999.

[66] E. Un and A. M. Hava, “A near-state PWM method with reduced switching losses and reduced common-mode voltage for three-phase voltage source inverters,” *IEEE Trans. Ind. Appl.*, vol. 45, no. 2, pp. 782–793, 2009.

[67] J. Zitzelsberger and W. Hofmann, “Reduction of Bearing Currents in inverter fed drive applications by using Sequentially Positioned Pulse Modulation,” *EPE J.*, vol. 14, no. 4, pp. 19–25, 2004.

[68] Y.-S. Lai and F.-S. Shyu, “Optimal common-mode voltage reduction PWM technique for inverter control with consideration of the dead-time effects-part I: basic development,” *IEEE Trans. Ind. Appl.*, vol. 40, no. 6, pp. 1605–1612, 2004.

[69] M. Cacciato, A. Consoli, G. Scarcella, and A. Testa, “Reduction of common-mode currents in PWM inverter motor drives,” *IEEE Trans. Ind. Appl.*, vol. 35, no. 2, pp. 469–476, 1999.

[70] A. Iqbal, S. Moinoddin, S. Ahmad, M. Ali, A. Sarwar, and K. N. Mude, “Multiphase converters,” in *Power Electronics Handbook*, Elsevier, 2018, pp. 457–528.

[71] B. R. Naidu, G. Panda, and B. C. Babu, “Dynamic energy management and control

of a grid-interactive DC microgrid system," in *Smart Power Distribution Systems*, Elsevier, 2019, pp. 41–67.

[72] S. Pawar and A. S. Kulkaarni, "Effect of Carrier Frequency on the Performance of Three Phase SPWM Inverter," *Int. J. Sci. Eng. Technol. Res*, vol. 4, no. 9, pp. 3019–3023, 2015.

[73] A. K. Sharma, V. Mishra, N. Kaushik, M. Singhal, and A. Sharma, "Advanced Techniques for Controlling Output Voltage of Inverter," *Int. J. Electron. Commun. Eng.*, vol. 3, no. 2, 2013.

[74] P.-E. Vidal, B. Trajin, and F. Rotella, "Stratégie et technique pour le pilotage en modulation des convertisseurs statiques," *Tech. l'Ingénieur*, 2019.

[75] K. Berkoune, "Approche mathématique pour la Modulation de Largeur d'Impulsion (MLI) pour la conversion statique de l'énergie électrique: application aux onduleurs multiniveaux." 2016.

[76] S. L. Capitaneanu, "Optimisation de la fonction MLI d'un onduleur de tension deux-niveaux." 2002.

[77] R. Jadeja, A. Ved, and S. Chauhan, "An Investigation on the performance of random PWM controlled converters," *Eng. Technol. Appl. Sci. Res.*, vol. 5, no. 6, pp. 876–884, 2015.

[78] S.-Y. Oh, Y.-G. Jung, and Y.-C. Lim, "A two-phase dual-zero vector RCD-PWM (DZRCD) technique," in *30th Annual Conference of IEEE Industrial Electronics Society, 2004. IECON 2004*, 2004, vol. 1, pp. 30–34.

[79] M. Nayeemuddin, T. B. Reddy, and M. V. Kumar, "Space vector based random pwm algorithms for acoustic noise and harmonics reduction for voltage source inverter fed ac drive," *Energy Procedia*, vol. 117, pp. 353–360, 2017.

[80] H. Wang and F. Blaabjerg, "Reliability of capacitors for DC-link applications in power electronic converters—An overview," *IEEE Trans. Ind. Appl.*, vol. 50, no. 5, pp. 3569–3578, 2014.

[81] N. Sharma and V. K. Garg, “Comparison of SPWM VSI and SVPWM VSI FED Induction Machine Using Volt per Hertz Control Scheme,” *UIET, Kurukshetra, Haryana*.

[82] N. O. Çetin and A. M. Hava, “Scalar PWM implementation methods for three-phase three-wire inverters,” in *2009 International Conference on Electrical and Electronics Engineering-ELECO 2009*, 2009, pp. I–447.

[83] B. Tolunay, “Space Vector Pulse Width Modulationfor Three-Level Converters: a LabVIEW Implementation.” 2012.

[84] H. W. Van Der Broeck, H.-C. Skudelny, and G. V. Stanke, “Analysis and realization of a pulsewidth modulator based on voltage space vectors,” *IEEE Trans. Ind. Appl.*, vol. 24, no. 1, pp. 142–150, 1988.

[85] S. Ogasawara, H. Akagi, and A. Nabae, “A novel PWM scheme of voltage source inverters based on space vector theory,” *Arch. für Elektrotechnik*, vol. 74, no. 1, pp. 33–41, 1990.

[86] D. G. Holmes, “The significance of zero space vector placement for carrier-based PWM schemes,” *IEEE Trans. Ind. Appl.*, vol. 32, no. 5, pp. 1122–1129, 1996.

[87] V. Blasko, “A hybrid PWM strategy combining modified space vector and triangle comparison methods,” in *PESC Record. 27th Annual IEEE Power Electronics Specialists Conference*, 1996, vol. 2, pp. 1872–1878.

[88] S. M. Dabour, A. S. Abdel-Khalik, A. M. Massoud, and S. Ahmed, “Analysis of scalar PWM approach with optimal common-mode voltage reduction technique for five-phase inverters,” *IEEE J. Emerg. Sel. Top. Power Electron.*, vol. 7, no. 3, pp. 1854–1871, 2018.

[89] B. K. Bose, “Power electronics and motor drives recent progress and perspective,” *IEEE Trans. Ind. Electron.*, vol. 56, no. 2, pp. 581–588, 2008.

[90] P.-E. Vidal, S. Cailhol, F. Rotella, K. Berkoune, A. Llor, and M. Fadel, “Generalized inverses applied to Pulse Width Modulation for static conversion: a first study,” in *2013 15th European Conference on Power Electronics and Applications (EPE),*

2013, pp. 1–10.

[91] M. P. Kazmierkowski, R. Krishnan, and F. Blaabjerg, *Control in power electronics*. Elsevier, 2002.

[92] S. L. Capitaneanu, B. De Fornel, M. Fadel, J. Faucher, and A. Almeida, “Graphical and algebraic synthesis for PWM methods,” *EPE J.*, vol. 11, no. 3, pp. 16–28, 2001.

[93] K. L. Shi and H. Li, “Optimized PWM strategy based on genetic algorithms,” *IEEE Trans. Ind. Electron.*, vol. 52, no. 5, pp. 1458–1461, 2005.

[94] H. Kakigano, M. Nomura, and T. Ise, “Loss evaluation of DC distribution for residential houses compared with AC system,” in *The 2010 International Power Electronics Conference-ECCE ASIA-*, 2010, pp. 480–486.

[95] A. M. Hava, R. J. Kerkman, and T. A. Lipo, “A high-performance generalized discontinuous PWM algorithm,” *IEEE Trans. Ind. Appl.*, vol. 34, no. 5, pp. 1059–1071, 1998.

[96] T. B. Reddy, J. Amarnath, D. Subbarayudu, and M. H. Khan, “Generalized discontinuous PWM based direct torque controlled induction motor drive with a sliding mode speed controller,” in *2006 International Conference on Power Electronic, Drives and Energy Systems*, 2006, pp. 1–6.

[97] A. M. Trzynadlowski and S. Legowski, “Minimum-loss vector PWM strategy for three-phase inverters,” *IEEE Trans. Power Electron.*, vol. 9, no. 1, pp. 26–34, 1994.

[98] H. Der Van Broeck, “Analysis of the voltage harmonics of PWM voltage fed inverters using high switching frequencies and different modulation functions,” *Eur. Trans. Electr. Power*, vol. 2, no. 6, pp. 341–350, 1992.

[99] D. R. Alexander and S. M. Williams, “An optimal PWM algorithm implementation in a high performance 125 kVA inverter,” in *Proceedings Eighth Annual Applied Power Electronics Conference and Exposition*, 1993, pp. 771–777.

[100] J. W. Kolar, H. Ertl, and F. C. Zach, “Influence of the modulation method on the conduction and switching losses of a PWM converter system,” *IEEE Trans. Ind.*

*Appl.*, vol. 27, no. 6, pp. 1063–1075, 1991.

[101] Z. Nie and N. Schofield, “Multi-phase VSI DC-link capacitor considerations,” *IET Electr. Power Appl.*, vol. 13, no. 11, pp. 1804–1811, 2019.

[102] H. Ye and A. Emadi, “An interleaving scheme to reduce DC-link current harmonics of dual traction inverters in hybrid electric vehicles,” in *2014 IEEE Applied Power Electronics Conference and Exposition-APEC 2014*, 2014, pp. 3205–3211.

[103] A. Voldoire, J.-L. Schanen, J.-P. Ferrieux, C. Gautier, and C. Saber, “Analytical Calculation of DC-Link Current for N-Interleaved 3-Phase PWM Inverters Considering AC Current Ripple,” in *2019 21st European Conference on Power Electronics and Applications (EPE’19 ECCE Europe)*, 2019, p. P-1.

[104] S. Kato, N. Hoshi, and K. Oguchi, “Small-scale hydropower,” *IEEE Ind. Appl. Mag.*, vol. 9, no. 4, pp. 32–38, 2003.

[105] P. A. Dahono, Y. Sato, and T. Kataoka, “Analysis and minimization of ripple components of input current and voltage of PWM inverters,” *IEEE Trans. Ind. Appl.*, vol. 32, no. 4, pp. 945–950, 1996.

[106] T. Esram and P. L. Chapman, “Comparison of photovoltaic array maximum power point tracking techniques,” *IEEE Trans. energy Convers.*, vol. 22, no. 2, pp. 439–449, 2007.

[107] T. Furukawa, D. Senzai, and T. Yoshida, “Electrolytic capacitor thermal model and life study for forklift motor drive application,” in *2013 World Electric Vehicle Symposium and Exhibition (EVS27)*, 2013, pp. 1–6.

[108] T. D. Nguyen, “Analyse des sollicitations sur les c continu d’onduleur pour.”

[109] J. P. Hansen, P. A. Narbel, and D. L. Aksnes, “Limits to growth in the renewable energy sector,” *Renew. Sustain. Energy Rev.*, vol. 70, pp. 769–774, 2017.

[110] IRENA, “Wind power,” 2021. [Online]. Available: https://www.irena.org/wind.

[111] P. S. Georgilakis, “Technical challenges associated with the integration of wind power into power systems,” *Renew. Sustain. Energy Rev.*, vol. 12, no. 3, pp. 852–

863, 2008.

[112] R. D. Shukla and R. K. Tripathi, “A novel voltage and frequency controller for standalone DFIG based Wind Energy Conversion System,” *Renew. Sustain. energy Rev.*, vol. 37, pp. 69–89, 2014.

[113] F. Becker, “Emulation d’une chaîne éolienne de conversion d’énergie.” UHP-Université Henri Poincaré, 2011.

[114] E. Monmasson and J. Faucher, “Projet pédagogique autour de la MLI vectorielle,” *Rev. 3EI*, vol. 8, 1997.